Speckle Analysis of the Excitonic Emission from Quantum Wells

DISSERTATION

zur Erlangung des akademischen Grades
doctor rerum naturalium
(Dr. rer. nat.)
im Fach Physik

eingereicht an der
Mathematisch-Naturwissenschaftlichen Fakultät I
Humboldt-Universität zu Berlin

von
Herrn Dottore in Fisica Gianandrea Mannarini
geboren am 19.1.1977 in Lecce, Italien

Präsident der Humboldt-Universität zu Berlin:
Prof. Dr. J. Mlynek

Dekan der Mathematisch-Naturwissenschaftlichen Fakultät I:
Prof. T. Buckhout, PhD

Gutachter:

1. Prof. Dr. R. Zimmermann (HU Berlin)
2. Prof. G. C. La Rocca (SNS Pisa, Italien)
3. Priv.-Doz. Dr. B. Esser (HU Berlin)

eingereicht am:	28. Januar 2005
Tag der mündlichen Prüfung:	28. April 2005

Abstract

In this work, optical properties of semiconductor quantum wells (QW) are investigated, which are relevant for the light pattern (*speckle* pattern) emitted in non-specular directions by QW after resonant excitation of the exciton states. This secondary emission (SE) contains information on disorder and scattering processes in the sample. In particular, three main topics are investigated along this Thesis:

- *Spectral Speckle Analysis*
  Speckles in the direction- and frequency-resolved SE can be used for extraction of its coherent part, the Resonant Rayleigh Scattering (RRS). Furthermore, the frequency resolved lifetime of excitons within an inhomogeneously broadened ensemble can be established. A microscopic density matrix theory for excitons in interaction with acoustic phonons is developed and numerically solved. Good agreement with the experimental results for different QW sizes and temperatures is found.

- *Sloped Speckles*
  QW with mechanical strain are considered. For a proper geometry, the strain leads to a spatially dependent modification of the emission energy. Furthermore, a tilting of the direction- and time-resolved speckle pattern is experimentally observed. The theoretical description of the RRS allows to relate this tilting to the local value of the spatial gradient of the exciton energy. Numerical simulations make clear that this effect is not due to exciton motion along the strain gradient, but just relies on interference in an energetic landscape with systematic slope.

- *Non-Markovian exciton-phonon dynamics*
  Non-Markovian effects in QW are investigated, where both pure dephasing and dephasing due to relaxation between different excitonic states are possible. The density matrix theory is here numerically solved beyond the Markov approximation for the interaction between excitons and acoustical phonons. The absorption spectrum consists of Lorentzian peaks on top of broader sidebands originating from the non-Markovian coupling. These features are mostly important for the strongly localized states in the low energy side of the spectrum, suggesting a better interpretation of near-field experiments.

Keywords:
Disorder, Exciton, Phonon, Coherence, Quantum Wells, Density-matrix theory, non-Markovian Dynamics, Comparison with experiment

Zusammenfassung

In der vorliegenden Promotionsarbeit werden optische Eigenschaften von Halbleiterquantengräben untersucht, die mit der Ausbildung von *Speckle*-Mustern in der exzitonischen Emission zusammenhängen. Die in nichtspekulärer Richtung nach resonanter Anregung von Exzitonen ausgestrahlte Emission enthält Informationen über Unordnung und Streuprozesse in der Probe. Insbesondere werden drei Hauptthemen untersucht:

- *Spektrale Speckle-Analyse*
  Speckle in der winkel- und frequenzaufgelösten Emission können zur Bestimmung des koährenten Anteils (resonante Rayleighstreung) verwendet werden. Außerdem kann die innerhalb des inhomogen verbreiterten Ensembles frequenzaufgelöste Lebensdauer der Exzitonen bestimmt werden. Eine mikroskopische Dichtematrixtheorie für Excitonen in Wechselwirkung mit akustischen Phononen wird entwickelt und numerisch gelöst. Es wird eine gute Übereinstimmung mit den gemessenen Daten für unterschiedliche Quantengraben-Dicken und Temperaturen gefunden.

- *Schrägliegende Speckles*
  Es werden Quantengräben mit mechanischer Verzerrung betrachtet. Für geeignete Geometrien führt die Verzerrung zu einer ort-abhängigen Änderung der Emissionsenergie in der Ebene des Quantengrabens. Im weiteren wird experimentell beobachtet, dass das richtungs- und zeitaufgelöste Specklemuster eine Drehung erfährt. Die theoretische Beschreibung des Rayleigh-Spektrums erlaubt es, diese Drehung mit dem lokalen Wert des Gradienten der Exzitonenergie in Beziehung zu setzen. Numerische Simulationen zeigen, dass dieser Effekt nicht durch eine Bewegung der Exzitonen entlang des Verzerrungs-Gradienten verursacht wird, sondern auf Interferenzen in einer Energie-Landschaft mit systematischem Anstieg beruht.

- *Nicht-Markovsche Exziton-Phonon Dynamik*
  Nicht-Markovsche Effekte von Exzitonen in Quantengräben werden untersucht, wobei sowohl 'reines' Dephasieren als auch Dephasierung durch Relaxation der Exzitonen zwischen unterschiedlichen Zuständen möglich ist. Die Dichtematrixtheorie wird hier jenseits der Markovschen Näherung für die Streuung von Exzitonen an akustischen Phononen numerisch gelöst. Das Absorptionsspektrum besteht aus Lorentz-formige Peaks und breiteren Seitenbändern, die aus der nicht-Markovschen Kopplung stammen. Diese Eigenschaften sind vor allem für die stark lokalisierten Zustände auf der Niederenergie-Seite des Spektrums wichtig, und erlauben eine bessere Deutung von Nahfeld-Experimenten.

Schlagwörter:
Unordnung, Exziton, Phonon, Kohärenz, Quantengraben, Dichtematrixtheorie, nicht-Markovsche Dynamik, Vergleich mit Experimenten

Nel mezzo del cammin di nostra vita
mi ritrovai per una selva oscura
ché la diritta via era smarrita.
Ahi quanto a dir qual era è cosa dura
esta selva selvaggia e aspra e forte
che nel pensier rinova la paura!
Tant' è amara che poco è più morte;
ma per trattar del ben ch'i' vi trovai,
dirò de l'altre cose ch'i' v'ho scorte.

Halfway through the journey we are living
I found myself deep in a darkened forest,
For I had lost all trace of the straight path.
Ah how hard it is to tell what it was like,
How wild the forest was, how dense and rugged!
To think of it still fills my mind with panic.
So bitter it is that death is hardly worse!
But to describe the good discovered there
I here will tell the other things I saw.

Dante Alighieri, "Inferno" Canto I vv.1-9
(translation by James Finn Cotter)

Contents

Part I

Introductory matter

Chapter 1

Introduction

The impact of semiconductor nanostructures in solid state physics and in technology is inestimable. At the beginning of this lucky story is the invention in the late 1960s of the double heterostructure, or Quantum Well (QW), which was suggested by the 2000 Nobel laureate Z. I. Alferov.

We can summarize the main consequences of this invention in fundamental physics by mentioning: excitons at room temperature, tailoring of the energy spectrum, 2D electron gas, Quantum Hall Effect, Fractional Quantum Hall Effect. The technological applications have been impressive as well if we think at: 2D electron gas transistor, precise resistance standards, infrared quantum cascade laser. Perhaps the most impressive figure resuming the practical impact of nanostructures is the lowering of the threshold current for laser action, which has been lowered of a factor of 500 since introduction of QW up to year 2000. This fascinating story is told in [3].

Thus, the transport and optical properties of QW have assumed a strategic relevance and were intensively investigated in the last half century. We would like to position the Speckle Analysis among the techniques that have conquered an established role for understanding light-matter interaction in semiconductor nanostructures and that we briefly mention here (cp. [55, 49]):

Luminescence, in which photons from radiative recombination of electrons an holes are detected. Since usually nonresonant excitation is used, the emitted photons carry information on the scattering processes (carrier-carrier and carrier-phonon) the particles have gone through. The emitted radiation can be detected either spectrally- or time-resolved;

Pump-Probe experiments, in which the investigated sample is excited by one pulse train (pump) and the changes it induces in the sample are probed by a second weaker pulse train (probe), which is eventually delayed with respect to the pump. Properties of the probe such as transmission, absorption, Raman scattering are monitored and the changes in the sample produced by the pump are studied;

Four-Wave-Mixing (FWM), which relies on interference between two laser pulses that originate an interference pattern in the sample, which translates into a density grating for the light of a third beam. This one is diffracted into a new beam (the fourth one, explaining the name of the technique). The fourth beam carries information on the interband polarization as long as the delay between the first two pulse is within the dephasing time of the system;

Spectral interferometry, which relies on the interference between the excitation beam and the emitted beam, [39]. Both amplitude and phase of the emitted field can be retrieved, both time- and spectrally-resolved [35]. A recent experiment measuring the interference between two beams emitted in different directions [25] can be considered as a new variant of spectral interferometry;

Speckle Analysis, which consists in simultaneous detection of the emission in a window of nonspecular directions after resonant excitation. This secondary emission (SE) exhibits intensity fluctuations (*speckles*) along detection direction which can be exploited for quantifying the coherent part of the emission, both in time- and spectrally-resolved experiments [37, 30].

These five techniques are compared on the same footing in Fig. 1.1.

Speckle Analysis is a linear technique, allowing one to study the sample for low excitation densities; does not need complicated setups such those used in FWM or spectral interferometry; gives access to intensity and coherence relaxation rates independently (whereas FWM just gives the sum of both rates); can accept any kind of excitation spectrum, from delta-pulse to continuous wave (cw) excitation; works both in time and spectral domain. This versatility relies on the simple idea on which Speckle Analysis is based: only coherent intensity contributes to the speckled (i.e., fluctuating) emission, see Chapter 2.

Speckle techniques have been developed in other physical contests too. In Sect. (2.2) a few examples from astronomy, and material science are presented.

The research done along this PhD-Thesis moved on a double track. On the one side, attention to the experimental world was paid, attempting to compare results of computer simulations with really measured quantities. This was successfully implemented for the Spectral Speckle Analysis (Chapter 3) and for the samples presenting Sloped Speckles (Chapter 4). On the other side, the theoretical model was improved. In Chapter 3 a density matrix theory with state-dependent relaxation rates was derived; in Chapter 4 the question of exciton acceleration in strained samples was discussed; in Chapter 5 the state-of-the-art Markov approximation for the exciton-phonon interaction was overcome, furnishing previsions for future experimental investigations. Appendixes A-D are thought to provide the mathematical tools and to describe the numerical techniques used for the actual calculations. Appendix E is a list of the used abbreviations.

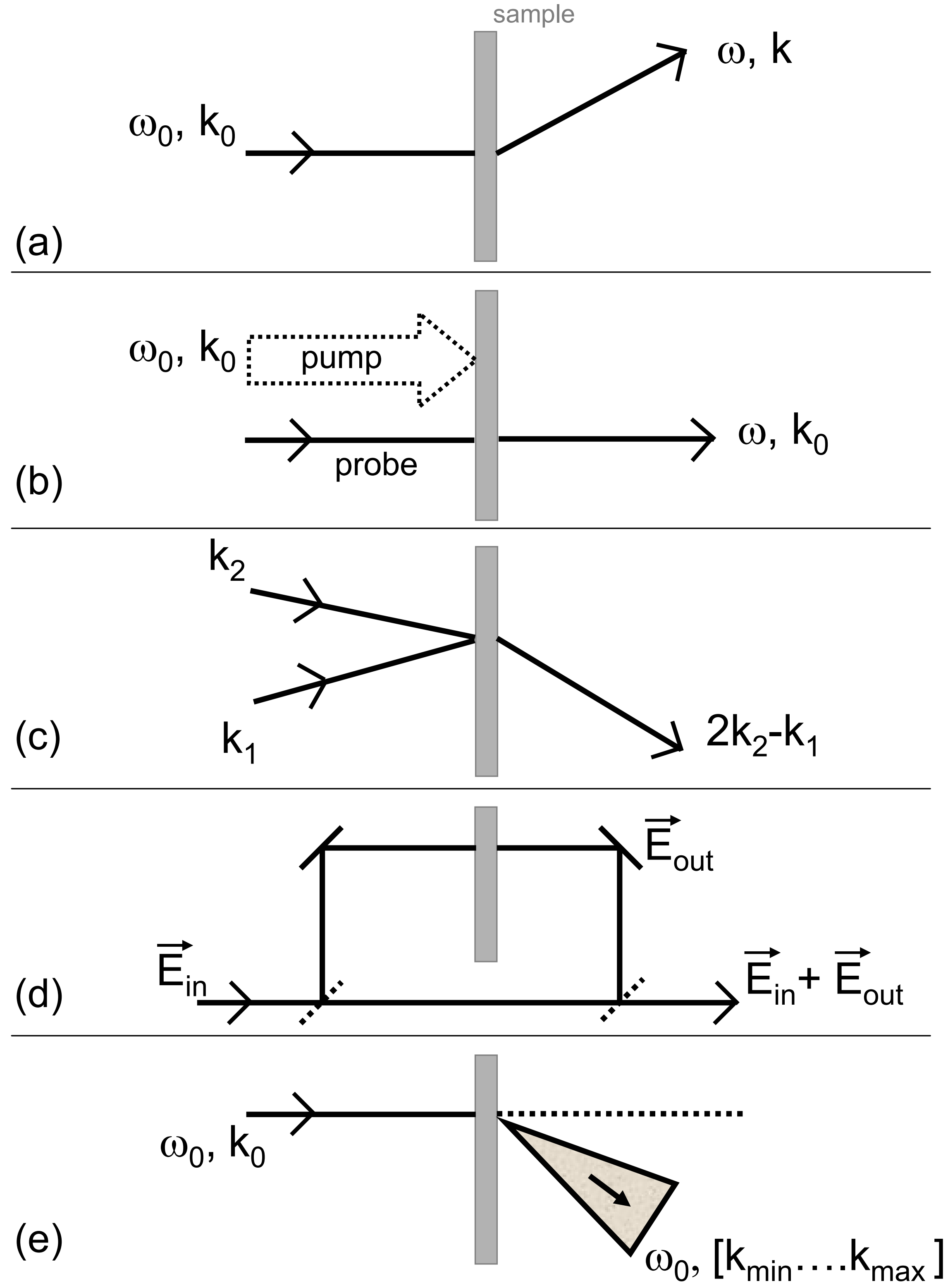

Figure 1.1: *The five main experimental techniques for investigating optical properties of semiconductor nanostructures: a) Luminescence; b) Pump-Probe (setup for differential transmission); c) FWM (the self-diffraction geometry is depicted: pulse 2 simultaneously creates the grating and is diffracted by the grating); d) Spectral Interferometry; e) Speckle Analysis.*

Chapter 2

Speckle basics

Speckles are random fluctuations of light intensity. They result from interference of electromagnetic waves from a disordered medium. An example is given in Fig. 2.1. In this Chapter introductory material to the physics of speckles and of their applications is presented. Though the focus of this work will be on speckles in semiconductor optics, the reader should be aware that speckle formation is a rather general phenomenon and that speckles are observed and their features exploited in many different fields. Therefore we start here with a general approach for describing speckle

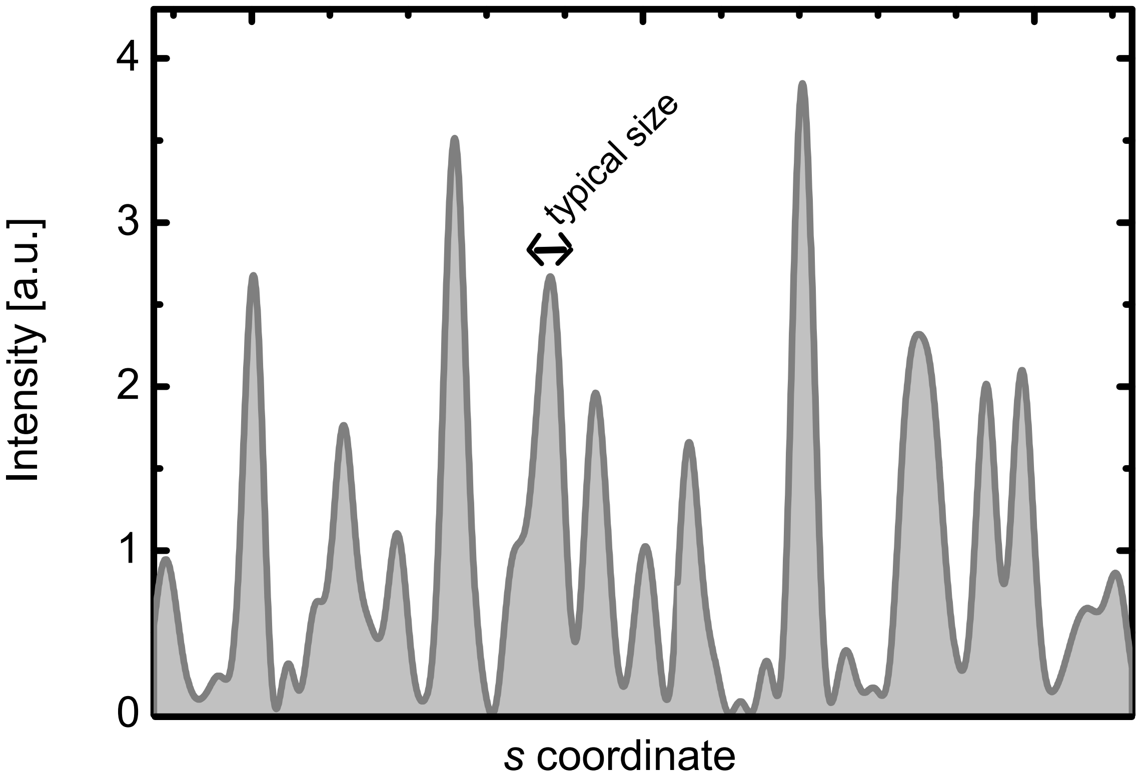

Figure 2.1: *Computer generated speckle pattern. The coordinate s can be any spatial ($\mathbf{R}$), directional ($\mathbf{k}$), temporal (t), or spectral (ω) coordinate where speckles appear. Speckles have got a typical size and even their intensity distribution is not random, see Fig. 2.2.*

formation (Sect. (2.1)), we give examples of speckles in astronomy and engineering (Sect. (2.2)), and finally turn to a close description of the relevant experiment for this Thesis (Sect. (2.3) and Sect. (2.4)).

2.1 Speckle formation

Speckle formation is a pure interference effect. As long as the photons emitted by optical oscillators are in phase-coherence among themselves, interference takes place. Speckle patterns are indeed nothing more than complicated interference patterns. In a sense, the object itself containing the oscillators ("sample") plays the role of the interferometer. The more coherently the oscillators are excited (spatial coherence of the source), and the less important decoherence processes are, the higher is the contrast[1] of the resulting interference pattern. The point that speckle patterns have a random character is due to disorder in the sample. Coherence and disorder are therefore the essential ingredients for observing speckles. They are also all what we need for deriving the statistical properties of speckle patterns. A suitable starting point for this task is the electrical field A of the emitted light which, due to interference, is given by the coherent sum

$$A = \sum_{j=1}^{N} a_j \, e^{i\Phi_j} \, . \tag{2.1}$$

In writing Eq. (2.1) we have already kept into account the effect of disorder: it is described by formation of N localized oscillators with random oscillator strengths, positions, and eigenfrequencies. These affect the amplitudes a_j and the phase factors Φ_j. At this level, we keep the functional dependence of the phase factors unspecified, since we want to determine the general properties of speckles. The disorder has to be such that the following properties of a_j and Φ_j are fulfilled:

i) a_j and Φ_j are uncorrelated;

ii) Φ_j are uniformly distributed in $[0, 2\pi]$;

iii) Φ_j, Φ_k and a_j, a_k are uncorrelated for $j \neq k$.

If this is the case, an exponential intensity probability density with average intensity I_0 is obtained, as derived in App. (A.1) [2] [3]:

$$p(I) = \left\langle \delta(I - A_R^2 - A_I^2) \right\rangle = \frac{\theta(I)}{I_0} \exp\left(-\frac{I}{I_0} \right) \, . \tag{2.2}$$

This basic property of speckle patterns was first derived in [13]. As a direct consequence of Eq. (2.2), $\langle I^2 \rangle = 2 \langle I \rangle^2$ and the ratio κ between intensity variance and

---

[1] See Eq. (2.3) for a definition of intensity contrast.

[2] $A_R = \mathrm{Re}A$; $A_I = \mathrm{Im}A$.

[3] The average $\langle \cdots \rangle$ is either an integration over the coordinate $\mathbf{R}$, $\mathbf{k}$, t, or ω where speckles appear or an ensemble average over different realizations of the disordered system. However, both definitions are equivalent when the ergodic theorem applies.

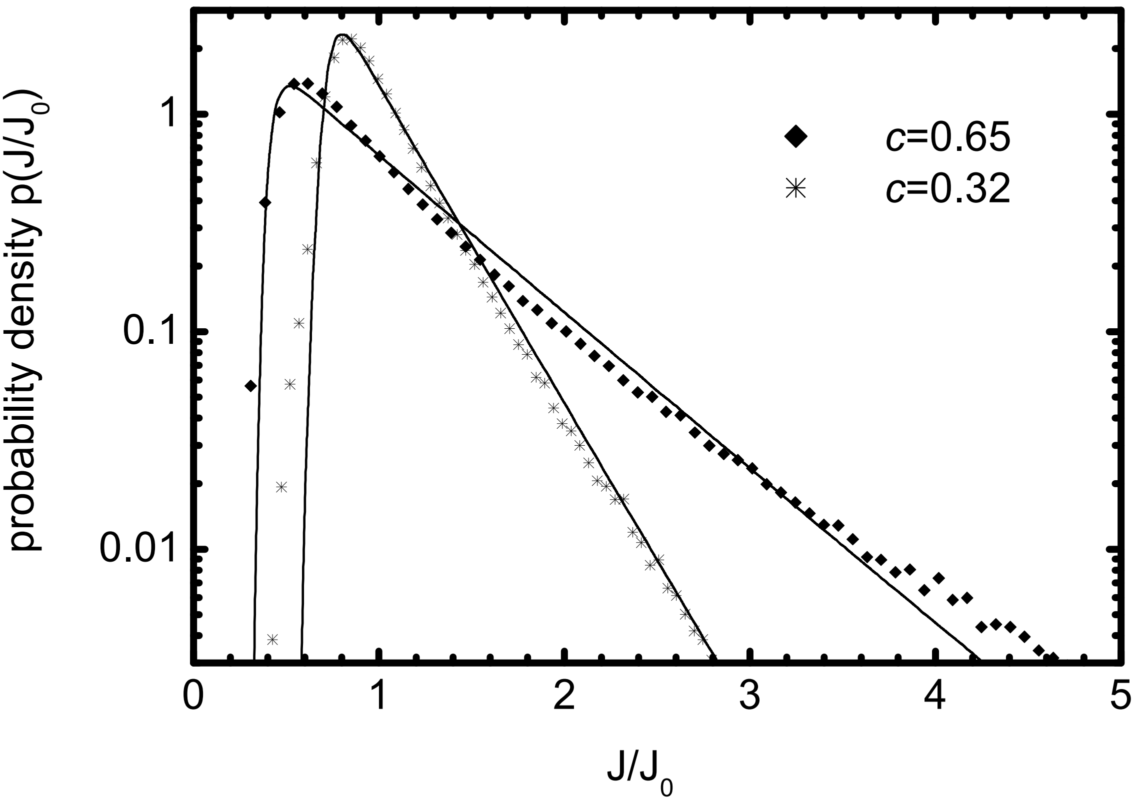

Figure 2.2: *Example of speckle intensity distribution $p(J)$ for different values of the contrast κ. The displaced exponential distribution is smoothed by an averaging process, but the average value $J_0 = I_0$ is unchanged with respect to the case of ideal resolution. Symbols: experimental data from the secondary emission of a semiconductor QW; lines: theoretical distribution for finite resolution parameter $N_{\text{eff}} = 1.2$. Figure edited after [30].*

average intensity is equal to unity:

$$\kappa = \frac{\sqrt{\langle I^2 \rangle - \langle I \rangle^2}}{\langle I \rangle} = 1 \,. \tag{2.3}$$

κ is called contrast of the speckle pattern. There are at least two cases in which κ can differ from unity:

a) presence of incoherent intensity;

b) finite experimental resolution.

(a) For instance if the oscillator is an exciton that undergoes an exciton-phonon scattering event (see Chapter 3), its phase factor Φ_j is irreversibly altered. This phase-destroying scattering can happen at any intermediate time after the excitation pulse and will differ from one single pulse to the next. This leads to a modification to the speckle pattern which is different for each pulse and which averages to a constant background after billions of repetitions of the driving pulse. The total intensity is hence the sum of a coherent intensity (the speckle pattern) and a constant, the incoherent intensity I^{inc}. The intensity probability density is now a displaced exponential,

$$p(I) = \frac{\theta(I - I^{\mathrm{inc}})}{I_0} \exp\left(-\frac{I - I^{\mathrm{inc}}}{I_0}\right) . \tag{2.4}$$

The speckle contrast κ is correspondingly reduced. However, the intensity variance is still due only to the coherent part I^{coh} of the emission. Indeed in App. (A.2) it is shown that the speckle contrast κ is identical to the *coherence degree* c of the emission, defined as

$$c = \frac{\left\langle I^{\mathrm{coh}}\right\rangle}{I^{\mathrm{inc}} + \left\langle I^{\mathrm{coh}}\right\rangle} . \tag{2.5}$$

This was the key observation that lead Langbein *et al.* to applications of the speckle analysis to the study of the optical coherence in time [37] and frequency resolved [30] experiments on semiconductor QW.

(b) The effect of finite experimental resolution is to average over speckles. This happens at costs of the detected intensity variance, which is lower than the emitted one. Therefore the detected contrast c_{det} is reduced to the value

$$c_{\mathrm{det}} = c \frac{1}{\sqrt{N_{\mathrm{eff}}}} , \tag{2.6}$$

where N_{eff} is an effective number of speckles over which it is averaged due to finite resolution. If the FWHM of the detector response function is δ and the the average speckle size Δ, then $N_{\mathrm{eff}} = 1 + 2(\delta/\Delta)^2$ [50]. The measured intensities J represent a directional average over I, and the measured distribution $p(J)$ deviates from the displaced exponential, approaching a Gaussian shape with increasing averaging. The detailed shape of $p(J)$ depends on the relative importance of the averaging along the two directional and the spectral detection parameters. Experimental intensity distributions from a QW are displayed in Fig. 2.2. They show a smoothed displaced exponential shape.

Since speckles have got typical sizes, (see Fig. 2.1), a useful concept for their characterization is the speckle correlation function,

$$C(s, \Delta s) = \frac{\langle I(s - \Delta s/2) I(s + \Delta s/2)\rangle}{\langle I(s - \Delta s/2)\rangle \langle I(s + \Delta s/2)\rangle} - 1 , \tag{2.7}$$

where s can be any of the variables $\mathbf{R}$, $\mathbf{k}$, t, or ω. The quantity $C(s, \Delta s)$ contains information about the average speckle size along the coordinate s. In App. (A.2) it is shown that, if the coherent part of the intensity is exponentially distributed, then the correlation function at $\Delta s = 0$ is proportional to the s-resolved coherence degree, $C(s, 0) = c^2(s)$.

2.2 Speckles outside semiconductor physics

Since the essential ingredients for speckle formation are

- spatially coherent excitation;

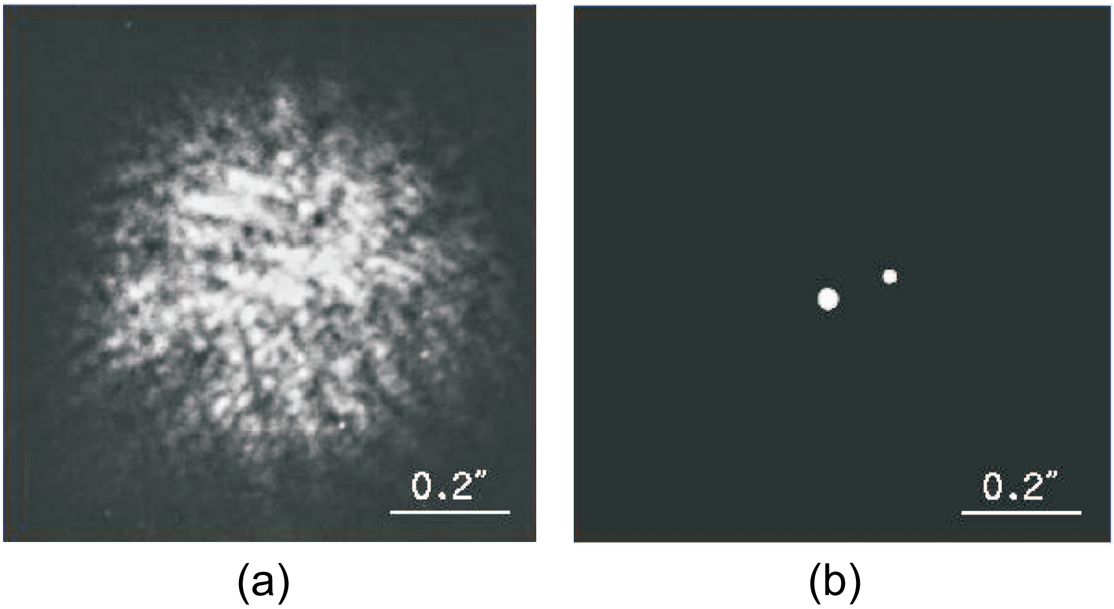

Figure 2.3: *(a): speckle interferogram of the binary star Ψ-Sagittarii. (b): the same star after application of the speckle masking method. The scale segment is equal to* 0.2 as. *Figure after [15].*

- random distribution of oscillator strength,

it is clear that the existence of speckles is not restricted to solid state physics. In this section, we review some specific examples of speckles in other physical contexts. Mostly important for applications have been up to now speckle techniques in astronomy and engineering.

Astronomy. The general inconvenience of optical terrestrial astronomy is the presence of the atmosphere. Due to air turbulence, the best achievable resolution is far poorer than the diffraction limit set by the telescope aperture, and it is about 1 arcsecond (as) in conditions of optimal seeing. For instance, a double star with separation smaller than 1 as is imaged as a diffraction pattern, Fig. 2.3(a). This is a speckle pattern: the star is the light source with some extent of spatial coherence and the atmosphere is the scattering medium (“disordered sample”).

In 1970, Labeyrie [34] developed the stellar speckle interferometry, which allows to extract the (instrument) diffraction limited autocorrelation of an astronomical object. His idea was to take advantage of the possibility to record many realizations of the speckle pattern (just take photographs at different times) for computing the ensemble averaged spread function of medium (atmosphere) and detector (telescope). A clever combination of Fourier transformations yields then the autocorrelation.

A significant improvement to this technique was carried out by Weigelt in 1977 [68] with the speckle masking method. The input for this technique is the autocorrelation obtained by the speckle interferometry. A nonlinear processing yields then the (single atmosphere-realization) spread function, that allows to recover the real image. Advantages over the autocorrelation are that angular positions of double stars can be retrieved and that images are more intuitive and easier to remember than autocorrelations. An example of application of this technique is given in Fig. 2.3(b) where a binary star with separation below 0.2 as is resolved. The speckle masking method allows to reach a resolution of 0.075 as, which is equal to the diffraction limit of a 1.3 m diameter telescope at a mean wavelength of 400 nm, [69]. A comprehensive review of more modern achievements in optical astronomy based on the Speckle techniques can be found in [52].

Engineering. Broad sectors of applied science have profited of the information that is possible to extract from speckles. Here, we just mention applications for measuring surface roughness [13], probing the magnetic return-point memory [48] and the local magnetic configuration in nanostructures [12], study of fluidodynamics [11, 65], and coherent control of conjugated polymers [27].

Finally not to forget, detection of moving speckle patterns is at the heart of widespread computer devices, like optical mouse and optical pen. The sector is still expanding and the recent launch of a specialized magazine (Journal Of Holography And Speckles, JOHAS) is a signal for that.

2.3 Experimental setup for speckle spectroscopy from Quantum Wells

All experimental results concerning QW that will be shown in this thesis have been obtained by Wolfgang Langbein and Gerrit Kocherscheidt at the University of Dortmund. Here we briefly review the main features of their experiment. The setup comprises the light source, a controllable environment for the sample, the imaging optics, and the detection system. It is sketched in Fig. 2.4.

The light source is a Fourier-limited pulsed laser, whose spectrum, duration, and repetition rate are adjustable through a pulse shaper. The environment is a Helium bath cryostat which allows temperatures down to 1.5 K. The imaging system consists of a part that guarantees that the emission in nonspecular directions (secondary emission, SE) is transmitted to the entrance of the detector, and a part that assures directional imaging at the detector position. The achieved angular resolution is $\delta = 0.4$ mrad, which is usually much smaller than the typical speckle size Δ (as mentioned in Sect. (2.1), the final results have to be corrected for this finite resolution).

The key feature for doing speckle analysis is simultaneous detection of many speckles. That is, a three-dimensional signal has to be recorded (two angular dimensions and time or frequency resolution). A two-dimensional signal can be measured in parallel by nowadays' detectors. The third dimension is recorded doing sequential measurements. The detector is either a streak camera (time resolution limited to 2 ps) or a CCD camera in series to a spectrometer (resolution FWHM about 20 μeV, see Sect. (3.5) for details). For further experimental details, see [31].

The experimental situation is mapped to the general description of speckle properties of Sect. (2.1) in the following way. The amplitude a_j is identified with the oscillator strength of an exciton state localized around $\mathbf{R}_j$. When this exciton recombines, it emits a spherical wave (approximated in our description by a plane wave because the sample-detector distance is much larger than sample size) of momentum $\mathbf{k}$ whose phase Φ_j is

$$\Phi_j = \mathbf{k} \cdot \mathbf{R}_j - \omega_j t \,, \tag{2.8}$$

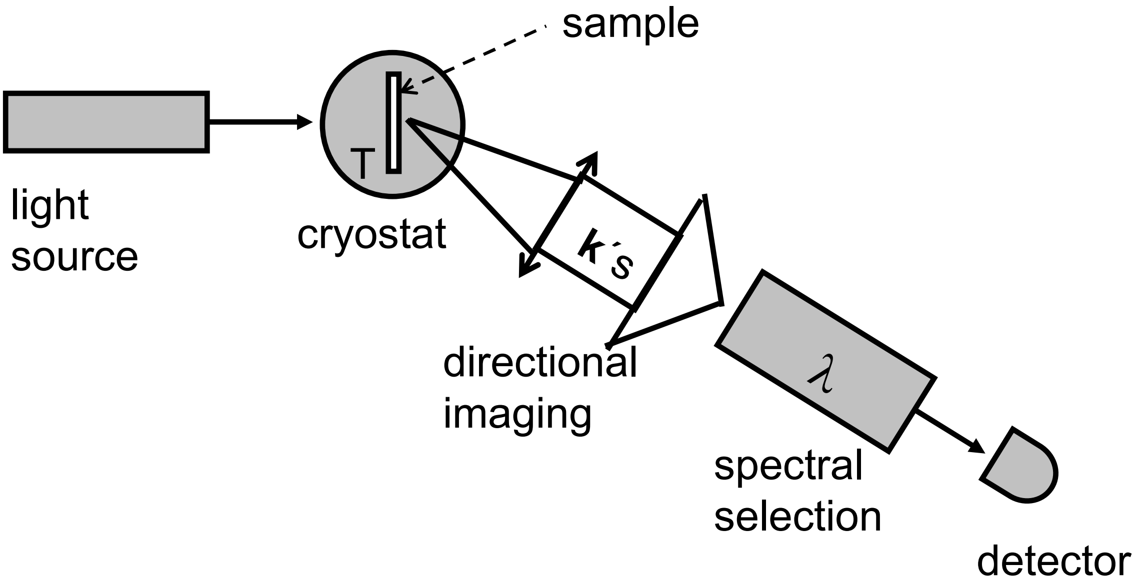

Figure 2.4: *Schematic representation of the experimental setup used at the University of Dortmund for the speckle experiments.*

where ω_j is the eigenfrequency of the $j-$th exciton. Eq. (2.8) implies that speckles appear both along the detection directions $\mathbf{k}$ and in the time t resolved emission. The emission in the Fourier conjugated spaces $\mathbf{R}$ (near-field detection) and ω (spectral domain) are speckled as well. Due to Eq. (2.8), the condition (ii) of Sect. (2.1) implies that, for observing speckles with the exponential distribution as in Eq. (2.2), the size Φ_F of the illuminated region has to be much larger than the wavelength $\lambda = 2\pi c/|\mathbf{k}|$ and that the detection time t has to be much larger than the inverse of the inhomogeneous broadening σ of the ensemble of transition frequencies ω_j. In Fig. 2.5 is sketched how speckle formation takes place in the angular resolved SE. The intensity-intensity correlation function $C(s, \Delta s)$ has the meaning of average speckle shape along s. In particular the range of $C(\Delta\mathbf{k})$ is Φ_F^{-1} and the range of $C(\Delta t)$ is $\hbar\sigma^{-1}$ [37]. The width of the function $C(\Delta\omega)$ is related to $\Gamma_0(\omega)$, the average dephasing rate for packets of excitons of energy $\hbar\omega$, see Sect. (3.5).

2.4 Existing results on speckles in semiconductor physics

The seminal idea and the first application of the Speckle Analysis to semiconductors physics were published by Langbein *et al.* [37]. The central observation was that SE fluctuates over the emission directions. These fluctuations (speckles) are due to the inhomogeneous distribution of oscillator strength in the plane of the QW: because of disorder, exciton states are localized at random, Fig. 2.5. The point is that the mere existence of speckles is a fingerprint of coherence: only coherent photons can interfere. On the other hand, exciton-phonon scattering destroys coherence and contributes to SE as a directionless background. The speckle contrast can thus be used as a measure of the Resonant Rayleigh Scattering (RRS), the co-

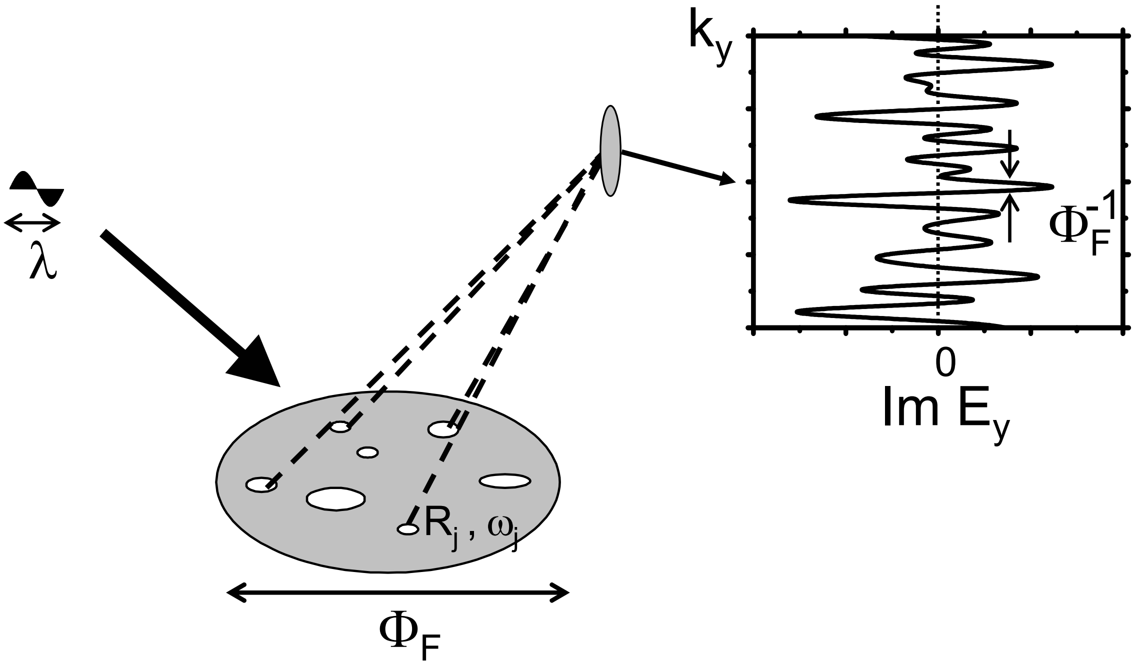

Figure 2.5: *Speckle formation in the angular resolved SE (imaginary part of a component of the electric field is shown) after coherent excitation of an ensemble of localized oscillators.*

herent part of SE. Time-resolved Speckle Analysis makes unnecessary complicated interferometric setups, is a linear technique, and allows a simultaneous determination of the inhomogenous broadening, the state lifetime, and the coherence decay by phonon scattering. The coherence degree c is determined through the speckle contrast, Eq. (2.3), with the averaging done over the emission directions $\mathbf{k}$ [4]. The lifetime is the decay constant of the speckle averaged SE. The average speckle shape, computed through the speckle correlation function, contains information on both inhomogenous broadening and phonon scattering.

The theoretical description in [37] did not account for the fact that each exciton scattering rate has got an individual radiative and phonon scattering rate [51]. This limitation was overcome in the Spectral Speckle Analysis [30, 45].

A quantitative comparison between Four-Wave-Mixing (FWM) and Time-resolved Speckle Analysis was carried out in [36]. Measurements on QW of different thickness (8 and 35 nm) at different lattice temperatures were performed. The sum of radiative and phonon rates from Time-resolved Speckle Analysis agreed within error bars with the decay constant of time integrated FWM experiments.

Unpolarized SE was assumed to be fully incoherent by Stolz *et al.* [61]. However, application of the Speckle Analysis could show that it is not the case [38, 75]. The coherence decay time for cross polarized emission was even found to be 5 times longer than the intensity lifetime. Furthermore, subtracting the incoherent part found by the Speckle Analysis, the dynamics of the linear polarized emission gives insight into

---

[4] Without **k**-averaging, any value $0 \leq c \leq 1$ could be obtained, depending on which speckle (i.e., which direction) is observed. This incorrect procedure was applied in [9].

the in-plane anisotropy of the exciton wavefunctions.

Recently, speckled emission was proposed as a tool for investigating the formation of a Bose-Einstein condensate [73]. SE after off-resonant excitation is, because of relaxation, incoherent and therefore speckle-free. But at low temperature and high excitation density, a single macro-wavefunction appears. If the extension of this state exceeds the light wavelength, a speckled emission is obtained, despite of off-resonant excitation. The transition into the condensate phase can thus be followed by monitoring the increase of the speckle contrast κ.

Part II

Research results

Chapter 3

Spectral Speckle Analysis

The investigation of optical coherence in solid state systems has received continued interest in the last 20 years. This interest is driven by both fundamental and application reasons.

Specially deep insight has been possible by optical experiments on semiconductor QW. In particular, study of light emission in directions differing from the specular and the transmitted one has played an important role in these research.

Indeed this *secondary emission* (SE) contains information about scattering processes which the optical resonance has gone through. Excitons, that are the fundamental excitation in QW, can undergo scattering with any kind of static disorder (interfacial and compositional disorder), with the lattice vibration modes (optical and acoustical phonons), and with other excitons (high-order Coulomb effects for cases of high excitation density). In presence of an ideal crystal structure, in the limit of low excitation density, and if we could avoid phonon emission at zero temperature, light emission from a QW would be observed just in specular or transmitted direction: the in-plane component of the momentum has to be conserved (translational symmetry). Thus, SE would not be present in this case. This is why the mere existence of SE is a consequence of scattering processes. Studying to which extent coherence is preserved by scattering is of course an appealing business for the physicists.

We review here some important steps of the scientific work about coherence in the SE. The results of the Speckle Analysis obviously belong to this story, but have been discussed separately in Sect. (2.4) for the special relevance they have for this Thesis.

We stress that the word *coherence* always means for us that A is coherent with B, i.e. $A+B$ exhibits interference fringes. The coherent part of SE (with respect to the excitation field) is called Resonant Rayleigh Scattering (RRS). RRS is due to elastic scattering of light by particles; it is therefore spectrally unshifted and coherent (no relaxation has taken place) with respect to the excitation. Furthermore, RRS is linear in the excitation field [41]. The emission difference between SE and RRS is usually called photoluminescence (PL).

Exploiting the fact that RRS is strongly enhanced for resonant excitation, Hegarty *et al.* [24] were able to record the first RRS spectrum from a multiple quantum well. They scanned an inhomogeneously broadened exciton resonance by continuous wave (cw) laser light and recorded the corresponding SE spectra. The peaks of these spectra were then identified as belonging to the RRS envelope.

The relation between SE and exciton-exciton scattering was studied by Wang *et al.* in a time-resolved experiment [66]. Sub-ps time resolution was achieved thanks to upconversion in a nonlinear crystal. It allowed to follow the fast build-up of SE and to monitor its dependence on the excitation density. The rise time of SE was found to be inversely proportional to the density. Furthermore, a beating between heavy and light hole (HH and LH) exciton showed to persist on a time longer than the time between exciton collisions. This was interpreted as a failure of the impact approximation, suggesting to take into account non-Markovian effects.

The possibility to make interference using partially coherent light was at the heart of the experiment by Gurioli *et al.* [22]. They excited the sample with two successive laser pulses and observed the interference signal as a function of mutual delay. In particular, the distortion of this interferogram by a spectral filter was exploited for quantifying the degree of coherence.

Switching between a mainly RRS- or PL-dominated SE was achieved by Haacke *et al.* [23] by varying the excitation density over 3 order of magnitudes, down to about 10^8 cm^{-2}. The time evolution of SE was observed. At low density, the build-up is density-independent and quadratic in time and was therefore interpreted as RRS. At higher density, SE rises linearly with density and was thought to be mainly due to incoherent PL.

An interferometric setup was used by Birkedal *et al.* [9], who claimed to have established a method for the determination of the frequency-resolved coherence degree. They let interfere the spectra of the laser and of the SE *at a fixed emission direction* and determined the coherence degree as a function of the interferogram amplitude. The weak point of their approach was that the directional fluctuations (speckles) in the SE were neglected. Therefore, as explained in Sect. (2.4), the value of the so obtained results is highly questionable.

The theoretical descriptions have been based so far on density matrix formalism, starting either from an electron-hole or a from an exciton picture.

The time evolution of the SE signal recorded by Wang *et al.* [66] at a certain excitation density could be explained by Zimmermann [72] who considered disorder as a source of scattering for excitons. The disorder was treated perturbatively at the level of the 2nd Born approximation. Non-Markovian effects (in the interaction with disorder) were partially accounted for by a weak-memory approximation.

Kira *et al.* [28] adopted the electron-hole basis and published numerical results showing that, even in the absence of disorder and phonon scattering, emission into nonspecular directions (SE) is possible. This SE signal is approximately quadratic in the excitation density and should rely on higher-order Coulomb processes.

The electron-hole picture in presence of both disorder and electron-phonon interaction was investigated by Thränhardt *et al.* [64, 63]. The electron-disorder interaction is treated at the 2nd Born level and thus is able to account only for weak disorder or wide QW. The electron-phonon interaction is on the level of the Fermi's golden rule. Numerical results could be compared to measurements for a 20 nm InGaAs/GaAs QW. Only the absorption spectrum was studied; furthermore the theoretical results had to be broadened phenomenologically for comparing to the experimental data, which were slightly renormalized.

3.1 Excitons in disordered Quantum Wells

In this section we present the main lines of a microscopic theory of excitons in QW, that accounts also for structural disorder.
Considering electron and hole motion and the band structure modifications due to spatial confinement in the QW growth direction and treating the crystal band structure within the effective mass approximation, a two-dimensional two-body Schrödinger problem evolves [78],

$$\begin{aligned}&\left(\mathcal{H}_{eh} - \epsilon_\alpha^{(0)}\right)\Psi_\alpha(\mathbf{r}_e, \mathbf{r}_h) = 0\\ &\mathcal{H}_{eh} = -\frac{\hbar^2}{2m_e}\Delta_{\mathbf{r}_e} - \frac{\hbar^2}{2m_h}\Delta_{\mathbf{r}_h} - \frac{e^2/(4\pi\varepsilon_0\varepsilon_S)}{|\mathbf{r}_e - \mathbf{r}_h|} + U_e(\mathbf{r}_e) + U_h(\mathbf{r}_h)\,.\end{aligned} \tag{3.1}$$

Here one conduction and one valence band are considered, whose edges $U_a(\mathbf{r}_a)$ $(a = e, h)$ are spatially varying functions, due to the presence of the QW heterostructure and to the various disorder sources. The main features of this complex problem can be captured by doing some approximations that we briefly discuss here. Following [74], we will always assume that disorder effects can be described in terms of an in-plane potential, whose strength [1] is

i) much smaller than the energetic distance of the confinement levels;

ii) much smaller than the exciton binding energy.

Assumption (i) allows us to be left with a single-sublevel equation, while assumption (ii) leads to factorization of in-plane wave function into centre-of-mass (COM) and (ground state, $1s$) relative motion. Very recent calculations for a very thin and disordered GaAs QW [18, 19] could quantify to which extent the relative part of the wave function is not identical for different COM states. However, we will always consider wide enough QW with moderate disorder, for which both assumptions (i) and (ii) should be satisfied. Consequently, the total wave function can be factorized into

$$\Psi_\alpha(\mathbf{r}_e, \mathbf{r}_h) = u_e(z_e)\, u_h(z_h)\, \phi_{1s}(\boldsymbol{\rho}_e - \boldsymbol{\rho}_h)\, \psi_\alpha(\mathbf{R})\,, \tag{3.2}$$

introducing the in-plane COM coordinate

$$\mathbf{R} = \frac{m_e\boldsymbol{\rho}_e + m_h\boldsymbol{\rho}_h}{M} \tag{3.3}$$

with the exciton kinetic mass $M = m_e + m_h$ and the in-plane electron(hole) coordinate $\boldsymbol{\rho}_e(\boldsymbol{\rho}_h)$. The confinement functions $u_a(z)$ in the growth direction result from the solution of the confinement equation

$$\left[-\frac{\hbar^2}{2m_a}\frac{d^2}{dz^2} + \overline{U}_a(z)\right] u_a(z) = E_a u_a(z)\,. \tag{3.4}$$

with the potential $\overline{U}_a(z) = V_a\left(\theta(x - L_z/2) + \theta(-x - l_z/2)\right)$ corresponding to the in-plane averaged situation with well width L_z and barrier heights V_a. In the numeric,

---

[1] For quantifying the disorder strength independently of the step size Δ_x of a computer simulation, we can consider the linewidth of the resulting linear absorption profile.

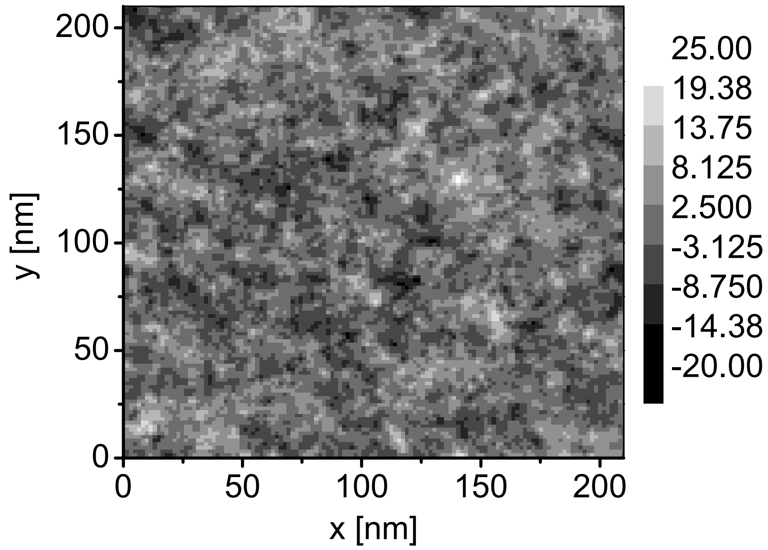

Figure 3.1: *An example of the spatially correlated random potential $V(\mathbf{R})$. Here $\hbar\sigma = 4.75$ meV, $a_B = 9.9$ nm and the grid resolution is 1.65 nm. The values in the grey-code are in meV.*

Gauss fits to the solutions $u_a(z)$ are used.

In [78] it is shown that the factorization Eq. (3.2) leads to the COM equation

$$\left(-\frac{\hbar^2}{2M}\Delta_{\mathbf{R}} + V(\mathbf{R})\right)\psi_\alpha(\mathbf{R}) = \epsilon_\alpha^{(0)}\,\psi_\alpha(\mathbf{R})\,, \tag{3.5}$$

where the potential $V(\mathbf{R})$ describes the well-width fluctuations and is given by

$$V(\mathbf{R}) = \int d\mathbf{R}' \sum_{a=e,h} \eta_a^2\,\phi_{1s}^2(\eta_a(\mathbf{R}-\mathbf{R}'))\,\frac{dE_a}{dL_z}\,\Delta L_z(\mathbf{R}')\,, \tag{3.6}$$

with mass ratios $\eta_e = M/m_h$ and $\eta_h = M/m_e$. The zero of the energies in Eq. (3.5) is the $1s$ exciton energy $\hbar\omega_X$ of the QW of average width L_z. The relative motion $\phi_{1s}(\mathbf{r})$ of the internal degrees of freedom of the exciton smoothes the fluctuations $\Delta L_z(\mathbf{R})$ of the well width. In the case growth-interruption techniques are not used [32], these fluctuations are correlated on a length scale much shorter than the QW exciton Bohr radius [20], which sets the lower "resolution limit" for the spatial correlations of the potential $V(\mathbf{R})$. Therefore $V(\mathbf{R})$ can be regarded as the convolution of a white noise potential $W(\mathbf{R})$ with the relative motion wavefunction $\phi_{1s}(\mathbf{r})$. Furthermore, since the relative weight of the hole part is $(\eta_h/\eta_e)^2 \approx 5.5$ times larger than the electron part, we take in the numerical simulations a monoexponential relative wave function. That is, we have used

$$V(\mathbf{R}) = \hbar\sigma\, g(\mathbf{R})^{-1/2} \int d\mathbf{R}'\,\phi_{1s}^2(\mathbf{R}-\mathbf{R}')\,W(\mathbf{R}')\,, \tag{3.7}$$

with

$$\phi_{1s}(\mathbf{r}) = \theta(\mathbf{r})\frac{2}{a_B}\exp\left(-\frac{\mathbf{r}}{a_B}\right)\,, \tag{3.8}$$

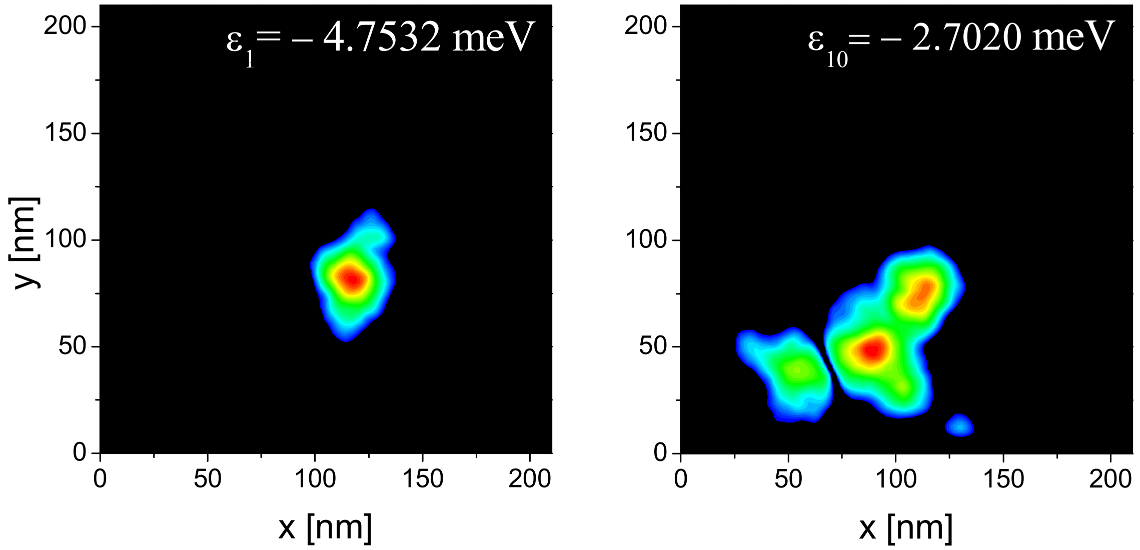

Figure 3.2: *The ground state and the* 10*th exciton COM states in the potential of Fig. 3.1. Corresponding eigenenergies are reported. Logarithmic scale over 3 orders of magnitude.*

where a_B is the exciton Bohr radius in a QW of average width L_z.
$W(\mathbf{R})$ is a white noise Gauss distributed potential,

$$\langle W(\mathbf{R})W(\mathbf{R}')\rangle = \delta(\mathbf{R}-\mathbf{R}')\,, \tag{3.9}$$

and the prefactor

$$g(\mathbf{R}) = \int d\mathbf{R}_1\, \phi_{1s}^4(\mathbf{R}-\mathbf{R}_1)\,. \tag{3.10}$$

ensures correct normalization.

3.2 Density-matrix approach

Our description of the system of QW excitons that interacts with phonons is based on a density-matrix approach. In this thesis the focus is set on disorder, suggesting us to start in the basis of disorder eigenstates $\psi_\alpha(\mathbf{R})$, calculated by diagonalization of Eq. (3.5). Since we are going to model experiments at low excitation power, the exciton density is always assumed to be low enough for neglecting exciton-exciton interaction. Thus, a bosonic commutation rule can be assigned to the operators $B^\dagger_\alpha, B_\alpha$ that create and destroy an exciton COM state $\psi_\alpha(\mathbf{R})$ [78]. In the Heisenberg picture, $B_\alpha(t)$ describes a local oscillating dipole within the QW. Therefore, it is the source of an emitted electromagnetic wave. Following Stolz [60], the field operator (positive rotating part) at a position $\mathbf{r}_1$ outside the sample is

$$\mathbf{E}_\alpha(\mathbf{r}_1,t) = \int d\mathbf{r}\, \frac{\omega_X^2\, \mu_{cv}}{c^2|\mathbf{r}_1-\mathbf{r}|}\, \Psi_\alpha(\mathbf{r}_e=\mathbf{r},\mathbf{r}_h=\mathbf{r})\, F(\mathbf{r}) B_\alpha(t'[t])\,. \tag{3.11}$$

This holds for dipole-allowed optical transitions (interband dipole matrix element μ_{cv}). The exciton-light coupling is proportional to the probability to find electron and hole at the same position, cp. Eq. (B.5). We have also inserted the long range modulation of this probability due to a focus function $F(\mathbf{r})$, modelling the excitation spot of the laser beam. The retarded time $t' = t - |\mathbf{r}_1 - \mathbf{r}|/c$ accounts for the free propagation from the source at $\mathbf{r}$ to the observation point at $\mathbf{r}_1$. In the far-field limit, the expansion $|\mathbf{r}_1 - \mathbf{r}| \approx r_1 - \mathbf{r}_1 \cdot \mathbf{r}/r_1$ holds and reduces the retarded time to $t' = t - r_1/c + \mathbf{q} \cdot \mathbf{r}/\omega_X$, where the emission wave vector is introduced as $\mathbf{q} = (\mathbf{r}_1/r_1)(\omega_X/c)$. Consequently the leading time dependence of the operator $B_\alpha(t') \sim \exp(i\omega_X t')$ is given by

$$B_\alpha(t') \approx B_\alpha(t - r_1/c)\, \mathrm{e}^{i\mathbf{q}\cdot\mathbf{r}}\,, \tag{3.12}$$

which converts the retardation into a spatial interference pattern. Altogether, we have

$$\mathbf{E}_\alpha(\mathbf{r}_1, t) = \frac{q^2\mu_{cv}}{r_1} \int d\mathbf{r}\, \Psi_\alpha(\mathbf{r},\mathbf{r})\, \mathrm{e}^{i\mathbf{q}\cdot\mathbf{r}}\, F(\mathbf{r}) B_\alpha(t - r_1/c)\,, \tag{3.13}$$

(the retardation along the sample was neglected by virtue of the light velocity of about 300 nm/fs). Summing over all states, we obtain

$$\mathbf{E}_\mathbf{q}(t) = \frac{q^2}{r_1} \sum_\alpha m_{\alpha\mathbf{q}}\, B_\alpha(t - r_1/c) \tag{3.14}$$

with the definition of the optical matrix element as

$$m_{\alpha\mathbf{q}} = \mu_{cv} \int d\mathbf{r}\, \mathrm{e}^{i\mathbf{q}\cdot\mathbf{r}}\, \Psi_\alpha(\mathbf{r},\mathbf{r}) F(\mathbf{r})\,. \tag{3.15}$$

If propagation from sample to detector is neglected, we can omit the q^2/r_1 prefactor and the overall retardation $-r_1/c$, ending with

$$\mathbf{E}_\mathbf{q}(t) = \sum_\alpha m_{\alpha\mathbf{q}} B_\alpha(t)\,. \tag{3.16}$$

Due to the factorization Eq. (3.2), the matrix element can be simplified as

$$m_{\alpha\mathbf{q}} = \mu_{cv}\, \phi_{1s}(0)\, O_{eh}\, \psi_{\alpha\mathbf{q}}\,, \quad \psi_{\alpha\mathbf{q}} = \int d\mathbf{R}\, \mathrm{e}^{i\mathbf{q}\cdot\mathbf{R}} \psi_\alpha(\mathbf{R}) F(\mathbf{R})\,, \tag{3.17}$$

where $\mathbf{R}$ is as before the 2-dimensional COM coordinate in the QW defined by Eq. (3.3). Therefore, in the Fourier-transformed wave function, only the in-plane component $\mathbf{q}_\parallel$ of the light wave vector $\mathbf{q}$ enters. Due to $L_z \ll \lambda = 2\pi c/\omega_X$, the confinement overlap $O_{eh} = \int dz\, u_e(z)\, \mathrm{e}^{iq_z z} u_h(z)$ is nearly independent of q_z.

Using Eq. (3.16) we write our model Hamiltonian for interacting phonons ($a_\mathbf{q}$), excitons (B_α), and photons ($C_\mathbf{q}$) as

$$\begin{aligned} \mathcal{H} &= \sum_\alpha \epsilon_\alpha^{(0)}\, B_\alpha^\dagger B_\alpha + \sum_\mathbf{q} \hbar w_\mathbf{q}\, a_\mathbf{q}^\dagger a_\mathbf{q} + \sum_\mathbf{q} \hbar\Omega_\mathbf{q}\, C_\mathbf{q}^\dagger C_\mathbf{q} \\ &+ \sum_{\alpha\beta\mathbf{q}} t_{\alpha\beta}^\mathbf{q} (a_\mathbf{q}^\dagger + a_{-\mathbf{q}}) B_\alpha^\dagger B_\beta + \sum_{\alpha\mathbf{q}} \left[m_{\alpha\mathbf{q}}\, B_\alpha\, C_\mathbf{q}^\dagger + m_{\alpha\mathbf{q}}^*\, B_\alpha^\dagger\, C_\mathbf{q} \right] \end{aligned} \tag{3.18}$$

In the first line of Eq. (3.18) the energies $\epsilon_\alpha^{(0)}$ are referred to the energy $\hbar\omega_X$ of the $1s$ exciton in a QW of average well width L_z; also the dispersions $\omega_{\mathbf{q}} = s|\mathbf{q}|$ of the acoustical phonons and $\Omega_{\mathbf{q}} = c|\mathbf{q}|$ of light appear. In the second line are the interaction terms. The deformation potential interaction between excitons and phonons is mediated by matrix elements $t^{\mathbf{q}}_{\alpha\beta}$ that are discussed in detail in App. (B.1). The dipole matrix elements $m_{\alpha\mathbf{q}}$ are evaluated in App. (B.2).
Deriving the dynamics of the exciton polarization $P_\alpha = \left\langle B^\dagger_\alpha \right\rangle$ according to the Heisenberg equation $-i\hbar\partial_t B^\dagger_\alpha = \left[\mathcal{H}, B^\dagger_\alpha\right]_-$, an infinite hierarchy of equations of motion is generated. This has to be truncated at some point for achieving a solution. According to [78], truncation is done at the level of the 2nd Born (2B) approximation by factorizing expectation values of terms containing more than one phonon operator:

$$\begin{aligned} \left\langle a^\dagger a B\right\rangle &\rightarrow \left\langle a^\dagger a\right\rangle \left\langle B\right\rangle \\ \left\langle a^\dagger a B^\dagger B\right\rangle &\rightarrow \left\langle a^\dagger a\right\rangle \left\langle B^\dagger B\right\rangle \end{aligned} \tag{3.19}$$

Then, the phonon population is assumed to be at equilibrium and thus described by the Bose distribution,

$$\left\langle a^\dagger_{\mathbf{q}} a_{\mathbf{q}}\right\rangle = n(\hbar\omega_{\mathbf{q}}) = \left[\exp(\hbar\omega_{\mathbf{q}}/k_B T) - 1\right]^{-1} . \tag{3.20}$$

We consider the dynamical variables

$$\begin{aligned} \text{exciton polarization} \quad & P_\alpha &&= \left\langle B^\dagger_\alpha \right\rangle ; \\ \text{exciton density matrix} \quad & N_{\alpha\beta} &&= \left\langle B^\dagger_\alpha B_\beta \right\rangle ; \\ \text{(phonon) emission assisted polarization} \quad & \hat{T}_{\alpha\mathbf{q}} &&= \left\langle a^\dagger_{\mathbf{q}} B^\dagger_\alpha \right\rangle ; \\ \text{(phonon) absorption assisted polarization} \quad & \tilde{T}_{\alpha\mathbf{q}} &&= \left\langle a_{-\mathbf{q}} B^\dagger_\alpha \right\rangle ; \\ \text{(phonon) emission assisted density matrix} \quad & T_{\alpha\beta\mathbf{q}} &&= \left\langle a^\dagger_{\mathbf{q}} B^\dagger_\alpha B_\beta \right\rangle . \end{aligned}$$

We treat the radiative decay in $P_\alpha(t)$ and $N_{\alpha\beta}(t)$ at the Markov level, as explained in the following section. This leads to decay rates r_α for polarization and density matrix,

$$r_\alpha = \frac{2\pi}{\hbar} \sum_{\mathbf{q}} |m_{\alpha\mathbf{q}}|^2 \left(g^{TE}_{\mathbf{q}} + g^{TM}_{\mathbf{q}}\right) \delta(\epsilon^{(0)}_\alpha - \hbar\Omega_{\mathbf{q}}) , \tag{3.21}$$

where the $g_{\mathbf{q}}$'s restrict the summation to the light cone, see Sect. (B.3).
Neglecting further terms of the type

$$\left\langle B^\dagger_\alpha B^\dagger_\beta B_\gamma \right\rangle \tag{3.22}$$

(low excitation density) and factorizing terms

$$\langle aC\rangle \rightarrow \langle a\rangle \langle C\rangle , \tag{3.23}$$

we derive the following equations of motion (master equation):

$$
\begin{aligned}
(-i\hbar\partial_t - \epsilon_\alpha^{(0)} - i\frac{\hbar r_\alpha}{2})P_\alpha(t) &= S_\alpha(t) + \sum_{\beta\mathbf{q}} t^{\mathbf{q}}_{\beta\alpha}\left(\hat{T}_{\beta\mathbf{q}}(t) + \tilde{T}_{\beta\mathbf{q}}(t)\right) \\
(-i\hbar\partial_t - \hbar\omega_{\mathbf{q}} - \epsilon_\beta)\hat{T}_{\beta\mathbf{q}}(t) &= \sum_\eta t^{-\mathbf{q}}_{\eta\beta}\left[n(\hbar\omega_{\mathbf{q}}) + 1\right]P_\eta(t) \\
(-i\hbar\partial_t + \hbar\omega_{\mathbf{q}} - \epsilon_\beta)\tilde{T}_{\beta\mathbf{q}}(t) &= \sum_\eta t^{-\mathbf{q}}_{\eta\beta}\, n(\hbar\omega_{\mathbf{q}})\, P_\eta(t) \\
(-i\hbar\partial_t - \epsilon_\alpha^{(0)} + \epsilon_\beta^{(0)} - i\hbar\frac{r_\alpha + r_\beta}{2})N_{\alpha\beta}(t) &= Q_{\alpha\beta}(t) \\
&\quad + \sum_{\gamma\mathbf{q}} t^{\mathbf{q}}_{\gamma\alpha}\left(T_{\gamma\beta\mathbf{q}}(t) + T^\dagger_{\beta\gamma-\mathbf{q}}(t)\right) \\
&\quad - \sum_{\gamma\mathbf{q}} t^{-\mathbf{q}}_{\beta\gamma}\left(T^\dagger_{\gamma\alpha-\mathbf{q}}(t) + T_{\alpha\gamma\mathbf{q}}(t)\right) \\
(-i\hbar\partial_t - \hbar\omega_{\mathbf{q}} - \epsilon_\alpha + \epsilon_\beta)T_{\alpha\beta\mathbf{q}}(t) &= \sum_\gamma t^{-\mathbf{q}}_{\gamma\alpha}[n(\hbar\omega_{\mathbf{q}}) + 1]N_{\gamma\beta}(t) \\
&\quad - t^{-\mathbf{q}}_{\gamma\beta}\, n(\hbar\omega_{\mathbf{q}})\, N_{\alpha\gamma}(t)
\end{aligned}
\tag{3.24}
$$

with source terms (at normal incidence, $\mathbf{q} = 0$) [2]

$$
\begin{aligned}
S_\alpha(t) &= m_{\alpha 0} E_{\text{in}}(t) e^{-i\omega_{\text{in}} t} \\
Q_{\alpha\beta}(t) &= S_\alpha(t) P^*_\beta(t) - S^*_\beta(t) P_\alpha(t)
\end{aligned}
\tag{3.25}
$$

where the incoming laser field has envelope $E_{\text{in}}(t)$ and is centered at the frequency $\omega_{\text{in}} = \omega_X + \delta\omega$. The bare 2B level has been improved toward self consistency including shifts of the exciton energies $\epsilon_\alpha = \epsilon_\alpha^{(0)} + \Delta_\alpha$ in the closing equations of the hierarchy. Without this correction, the exciton polarization and its two phonon-assisted quantities would exhibit poles at different energies. Since the energy shifts are due to the deformation potential interaction, we call them deformation shifts. They account for the deformation of the band structure in presence of the phonon cloud. Beginning in the next section, where we consider $\epsilon_\alpha = \epsilon_\alpha^{(0)}$ as a part of the Markov approximation in the exciton-phonon interaction, we will neglect these shifts in the remaining of this Chapter. However, in Chapter 5 we go beyond this approximation and show how to compute the deformation shifts (Eq. (5.4)).

3.3 Markov approximation

The master equation Eq. (3.24) contains memory effects and cross correlations between exciton states, as it is clear solving for instance the equation for $\hat{T}_{\beta\mathbf{q}}(t)$. Indeed, assuming $\langle a^\dagger_{\mathbf{q}} B^\dagger_\beta \rangle_{t_0} = 0$ at a time t_0 just before the excitation pulse arrived, we get ($\hbar\omega_\alpha \equiv \epsilon_\alpha$)

$$
\hat{T}_{\beta\mathbf{q}}(t) = \frac{i}{\hbar}\int_{t_0}^{t} dt' \sum_\eta e^{i(\omega_{\mathbf{q}} + \omega_\beta)(t-t')}[n(\hbar\omega_{\mathbf{q}}) + 1] t^{-\mathbf{q}}_{\eta\beta} P_\eta(t')\,. \tag{3.26}
$$

---

[2] In the following, normalization to the pulse area is used: $A_p = \int dt\, E_{\text{in}}(t) = 2\pi E_{\text{in}}(\Omega = 0) = 1$

This is inserted in the equation of motion for $P_\alpha(t)$, that therefore depends on all the past values of *each* $P_\eta(t)$. For remaining with a treatable problem, we resort to three distinct approximations, which we use to call collectively "Markov approximation".
i) Only the leading frequency ω_η is kept into the time dependence of the $P_\eta(t)$ appearing in the equation of motion for $\hat{T}_{\beta\mathbf{q}}(t)$, Eq. (3.26). In the same way, the density matrix is approximated as $N_{\alpha\beta} \sim e^{i(\omega_\alpha-\omega_\beta)t}$ in the equation for $T_{\alpha\beta\mathbf{q}}(t)$. Thus, extracting the slowly varying terms $e^{-i\omega_\eta t'}P_\eta(t') \approx e^{-i\omega_\eta t}P_\eta(t)$ from the integral in Eq. (3.26), one can analytically integrate to

$$\hat{T}_{\beta\mathbf{q}}(t) = -\frac{1}{\hbar}\sum_\eta \frac{1-e^{i\Delta\omega(t-t_0)}}{\Delta\omega}[n(\hbar\omega_\mathbf{q})+1]t^{-\mathbf{q}}_{\eta\beta}\, P_\eta(t) \tag{3.27}$$

with $\Delta\omega = \omega_\mathbf{q} + \omega_\beta - \omega_\eta + i0^+$. Allowing now for $t_0 \to -\infty$, the small imaginary part in $\Delta\omega$ is responsible for a factor

$$\frac{1}{\Delta\omega} = -i\pi\delta(\Delta\omega) + \mathcal{P}\frac{1}{\Delta\omega}\,, \tag{3.28}$$

which is expressed in terms of the Dirac equality. The first term contains the kernel of a conservation rule for the energy, which will appear in the exciton-phonon scattering rate. This step (i) is responsible for neglecting memory effects.
ii) The second term in Eq. (3.28) is responsible for the deformation shifts $\Delta_\alpha = \epsilon_\alpha - \epsilon^{(0)}_\alpha$ of the exciton energy, and is neglected because small (in the μeV-range, see Chapter 5).
iii) Still, we are left with the correlation between different exciton states. Again a leading frequency argument is applied. Only those $\hat{T}_{\beta\mathbf{q}}(t)$ contribute to the dynamics of $P_\alpha(t)$, which are in resonance: $\epsilon_\eta \approx \epsilon_\alpha$. Assuming non degenerate states, this condition translates into $\eta = \alpha$. [3]
Applying altogether the three steps of the Markov approximation, we find

$$t^\mathbf{q}_{\beta\alpha}\hat{T}_{\beta\mathbf{q}}(t) = i\pi\delta(\hbar\omega_\mathbf{q} + \epsilon_\beta - \epsilon_\alpha)[n(\hbar\omega_\mathbf{q})+1]|t^\mathbf{q}_{\beta\alpha}|^2 P_\alpha(t)\,. \tag{3.29}$$

A similar result for the phonon-absorption assisted polarization $\tilde{T}_{\beta\mathbf{q}}(t)$ allows to rewrite the r.h.s. (apart from the source term) of the equation for $P_\alpha(t)$ in system Eq. (3.24) in a compact way as:

$$\sum_{\beta\mathbf{q}} t^\mathbf{q}_{\beta\alpha}\left(\hat{T}_{\beta\mathbf{q}}(t) + \tilde{T}_{\beta\mathbf{q}}(t)\right) = \frac{i\hbar}{2}\sum_\beta \gamma_{\beta\leftarrow\alpha}P_\alpha(t)\,. \tag{3.30}$$

These terms represent a damping of the polarization via exciton-phonon scattering rates that are given by

$$\begin{aligned}\gamma_{\beta\leftarrow\alpha} = \frac{2\pi}{\hbar} &\sum_\mathbf{q} \Big(n(\hbar w_\mathbf{q})\,\delta\left(\epsilon_\beta - \hbar w_\mathbf{q} - \epsilon_\alpha\right) \\ &+ \quad (n(\hbar w_\mathbf{q})+1)\,\delta\left(\epsilon_\beta + \hbar w_\mathbf{q} - \epsilon_\alpha\right)\Big)\left|t^\mathbf{q}_{\beta\alpha}\right|^2\,.\end{aligned} \tag{3.31}$$

---

[3] This identification might be questionable, since in an infinite system states are infinitely close in energy. However, in each equation where this assumption is done, phonon matrix elements $t^\mathbf{q}_{\beta\alpha}t^{-\mathbf{q}}_{\eta\beta}$ appear, which assure that state α and state η need to have a spatial overlap with state β. Thus, if α and η have the same energy and are localized in the same region, they are almost certainly the same state because of level repulsion [79].

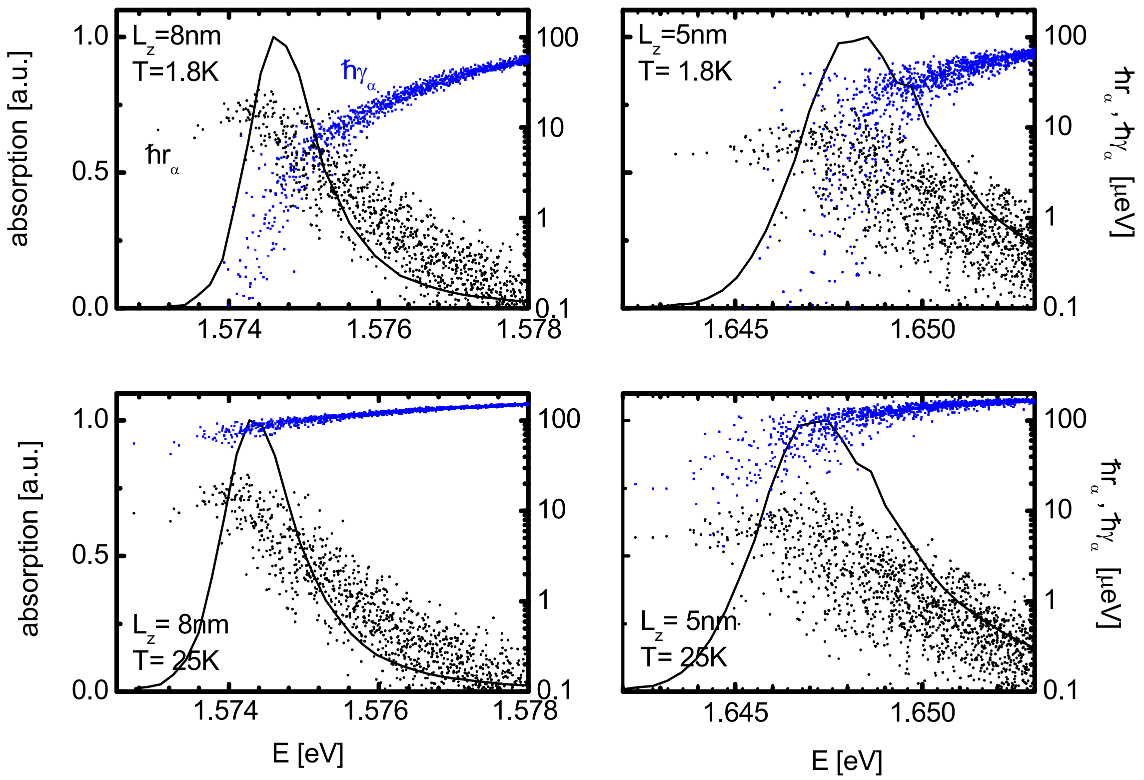

Figure 3.3: *Phonon (blue circles) and radiative (black circles) scattering rates* $\hbar\gamma_\alpha$ *and* $\hbar r_\alpha$ *according to the Markov approximation and simulated absorption lineshapes (solid lines). Top row: at* $T = 1.8$ *K; bottom row: at* $T = 25$ *K; left panels: for QW width* $L_z = 8$ *nm; right panels: for* $L_z = 5$ *nm.*

The structure of a transition rate within 2nd order perturbation theory is readily recognized: it is now clear that the Markov approximation in this three-step formulation leads to the appearance of Fermi's golden rule. In Chapter 5 we will show how to improve this approximation.

The total phonon (out-)scattering rates $\gamma_\alpha = \sum_\beta \gamma_{\beta\leftarrow\alpha}$ are reported in Fig. 3.3 for two different QW widths and temperatures [4]. At lower temperature they are dominated by phonon emission processes and essentially reflect the increasing density of states across the resonance. In the narrower QW phonon scattering is more effective, since exciton states are more extended in momentum space (due to both in-plane and growth direction localization) and thus couple to a larger number of phonon degrees of freedom.

One has to be more careful in deriving the Markov limit of the phonon assisted density matrix $T_{\alpha\beta\mathbf{q}}$. Indeed application of the steps i) and ii) leads to

$$\begin{aligned} T_{\alpha\beta\mathbf{q}} &= i\pi \sum_{\eta} \delta\left(\hbar w_{\mathbf{q}} + \epsilon_\alpha - \epsilon_\eta\right)\left(n(\hbar w_{\mathbf{q}}) + 1\right) t^{-\mathbf{q}}_{\eta\alpha}\, N_{\eta\beta} \\ &- i\pi \sum_{\eta} \delta\left(\hbar w_{\mathbf{q}} + \epsilon_\eta - \epsilon_\beta\right) n(\hbar w_{\mathbf{q}})\, t^{-\mathbf{q}}_{\beta\eta}\, N_{\alpha\eta} \qquad (3.32) \end{aligned}$$

---

[4] For a given QW width, the energy of the relaxation rates are shifted in such a way that the peak of the simulated SE match the experimental ones, see Sect. (3.6).

When inserted into the equation for $N_{\alpha\beta}(t)$ in system Eq. (3.24), the resonance condition implies $\eta = \alpha$ for the first line of the r.h.s of Eq. (3.32) and leads to the formation of an out-scattering term, similarly to Eq. (3.30). But $\epsilon_\gamma - \epsilon_\eta = \epsilon_\alpha - \epsilon_\beta$ holds for the leading frequency of the second line. The case $\{\gamma, \eta\} = \{\alpha, \beta\}$ is ruled out for $\omega_{\mathbf{q}} \neq 0$ by the delta-function in the scattering rate Eq. (3.31). Thus, the exciton-phonon scattering manifests itself with two qualitatively different contributions in the density matrix dynamics: the first one of out-scattering nature (like for the polarization) and the second one, originating from terms like (the arrow reminds that the r.h.s. is just a part of the l.h.s.)

$$\sum_{\gamma\mathbf{q}} \left(t^{\mathbf{q}}_{\gamma\alpha}\, T_{\gamma\beta\mathbf{q}} + t^{\mathbf{q}}_{\gamma\alpha}\, T^{\dagger}_{\beta\gamma-\mathbf{q}} \right) \longrightarrow -\, \delta_{\alpha\beta}\, \frac{i\hbar}{2} \sum_{\gamma} \gamma_{\alpha\leftarrow\gamma}\, N_{\gamma\gamma}(t)\,, \tag{3.33}$$

which is of in-scattering nature.

Summarizing, the system Eq. (3.24) reduces after application of the Markov approximation to the following coupled equations:

$$\begin{aligned} (-i\hbar\partial_t - \epsilon_\alpha - i\hbar\Gamma_\alpha) P_\alpha(t) &= S_\alpha(t) \\ (-i\hbar\partial_t - \epsilon_\alpha + \epsilon_\beta - i\hbar(\Gamma_\alpha + \Gamma_\beta)) N_{\alpha\beta}(t) &= S_\alpha(t) P^*_\beta(t) - S^*_\beta(t) P_\alpha(t) \\ &- i\hbar\delta_{\alpha\beta} \sum_{\gamma} \gamma_{\alpha\leftarrow\gamma} N_{\gamma\gamma}(t)\,, \end{aligned} \tag{3.34}$$

where the total scattering rate $2\Gamma_\alpha = r_\alpha + \gamma_\alpha$ has been introduced. As we shall see, it is convenient to consider the quantity

$$D_{\alpha\beta}(t) = N_{\alpha\beta}(t) - P_\alpha(t) P^*_\beta(t) \tag{3.35}$$

which, as a consequence of Eq. (3.34), is diagonal and satisfies:

$$\partial_t D_{\alpha\alpha}(t) = \sum_{\eta} \gamma_{\alpha\leftarrow\eta} |P_\eta(t)|^2 + \sum_{\eta} \gamma_{\alpha\leftarrow\eta} D_{\eta\eta}(t) - 2\Gamma_\alpha D_{\alpha\alpha}(t)\,. \tag{3.36}$$

We recognize here the structure of a rate equation, that is fed by a source term depending on the polarization. We call $D_{\alpha\beta}(t)$ either incoherent density, since it does not contribute to the speckled emission (see next section), or correlated density, for stressing the affinity with its non-Markovian extension that is non diagonal, as we shall see in Sect. (5.1).

Finally, we remark that the dipole coupling between exciton and light field operators also leads to equations of motion with memory and inter-state correlation, analogous to what the exciton-phonon interaction does. Therefore, we apply the Markov approximation for the exciton-light interaction as well. The macroscopic classical field $E_{\mathrm{in}}(t) = e^{i\omega_{\mathrm{in}} t} \langle C_{\mathbf{q}=0} \rangle$ is used. The photon distribution is set to zero (emission into the field vacuum). With these ingredients, the radiative rate r_α as in Eq. (3.21) is derived. Their values for our simulation QW are displayed in Fig. 3.3.

3.4 Frequency-resolved detection

The electrical field emitted into a direction with in-plane momentum $\mathbf{k}$ is given by the expectation value of

$$C^\dagger_{\mathbf{k}}(t) = \sum_\alpha m^*_{\alpha\mathbf{k}} B^\dagger_\alpha(t)\,. \tag{3.37}$$

The corresponding light intensity is

$$I_{\mathbf{k}}(t) = \left\langle C^\dagger_{\mathbf{k}}(t) C_{\mathbf{k}}(t) \right\rangle = \sum_{\alpha\beta} m^*_{\alpha\mathbf{k}} m_{\beta\mathbf{k}} N_{\alpha\beta}(t)\,. \tag{3.38}$$

This expression describes the speckle pattern in the time-resolved SE. Indeed replacing the single-time density matrix $N_{\alpha\beta}(t) = D_{\alpha\beta}(t) + P_\alpha(t) P^*_\beta(t)$, we obtain two terms,

$$I_{\mathbf{k}}(t) = I^{\mathrm{inc}}(t) + I^{\mathrm{coh}}_{\mathbf{k}}(t) = \sum_\alpha m^2_{\alpha 0} D_{\alpha\alpha}(t) + \left| \sum_\alpha m^*_{\alpha\mathbf{k}} P_\alpha(t) \right|^2\,. \tag{3.39}$$

The incoherent intensity does not depend on direction because for large wavelengths the phase factor in the dipole matrix elements is extracted, $m_{\alpha\mathbf{k}} \approx m_{\alpha 0} \exp(i\mathbf{k}\cdot\mathbf{R}_\alpha)$. Only the term containing the polarization is responsible for speckled emission. Thus, the time- resolved SE is completely determined by the polarization and the *single*-time incoherent density matrix.

Driven by the newer achievements of the experimental investigation, we want now to describe the *frequency*-resolved SE. Indeed this allows to overcome the limitation of time-resolved experiments to obtain very short time resolution, which would be necessary for following the SE dynamics of states with larger dephasing rates r_α and γ_α.

For determining the frequency resolved SE, we have to augment the information contained in the time resolved dynamics. The object doing this task is the spectrometer, which correlates signals at different times for giving the frequency resolution [45]. We model its action by convoluting the emitted field with a spectrometer response function $\mathcal{G}(\omega, t)$, obtaining the following electric field and intensity:

$$\begin{aligned} E_{\mathbf{k}}(\omega, t) &= \int dt_1\, \mathcal{G}(\omega, t - t_1) \left\langle C^\dagger_{\mathbf{k}}(t_1) \right\rangle \\ I_{\mathbf{k}}(\omega, t) &= \int dt_1\, \mathcal{G}(\omega, t - t_1) \int dt_2\, \mathcal{G}^*(\omega, t - t_2) \left\langle C^\dagger_{\mathbf{k}}(t_1) C_{\mathbf{k}}(t_2) \right\rangle\,. \end{aligned} \tag{3.40}$$

Thus, the frequency resolution naturally introduces as a new dynamical variable for the computation of the intensity spectra the *two-time* density matrix,

$$N_{\alpha\beta}(t_1, t_2) = \left\langle B^\dagger_\alpha(t_1) B_\beta(t_2) \right\rangle\,. \tag{3.41}$$

In App. (B.4) we show that it is given in terms of single time variables as

$$N_{\alpha\beta}(t_1, t_2) = \underbrace{\delta_{\alpha\beta}\, e^{i\omega_\alpha(t_1 - t_2) - \Gamma_\alpha |t_1 - t_2|} D_{\alpha\alpha}(\min\{t_1, t_2\})}_{\text{incoherent}} + \underbrace{P_\alpha(t_1) P_\beta(t_2)^*}_{\text{coherent}}\,. \tag{3.42}$$

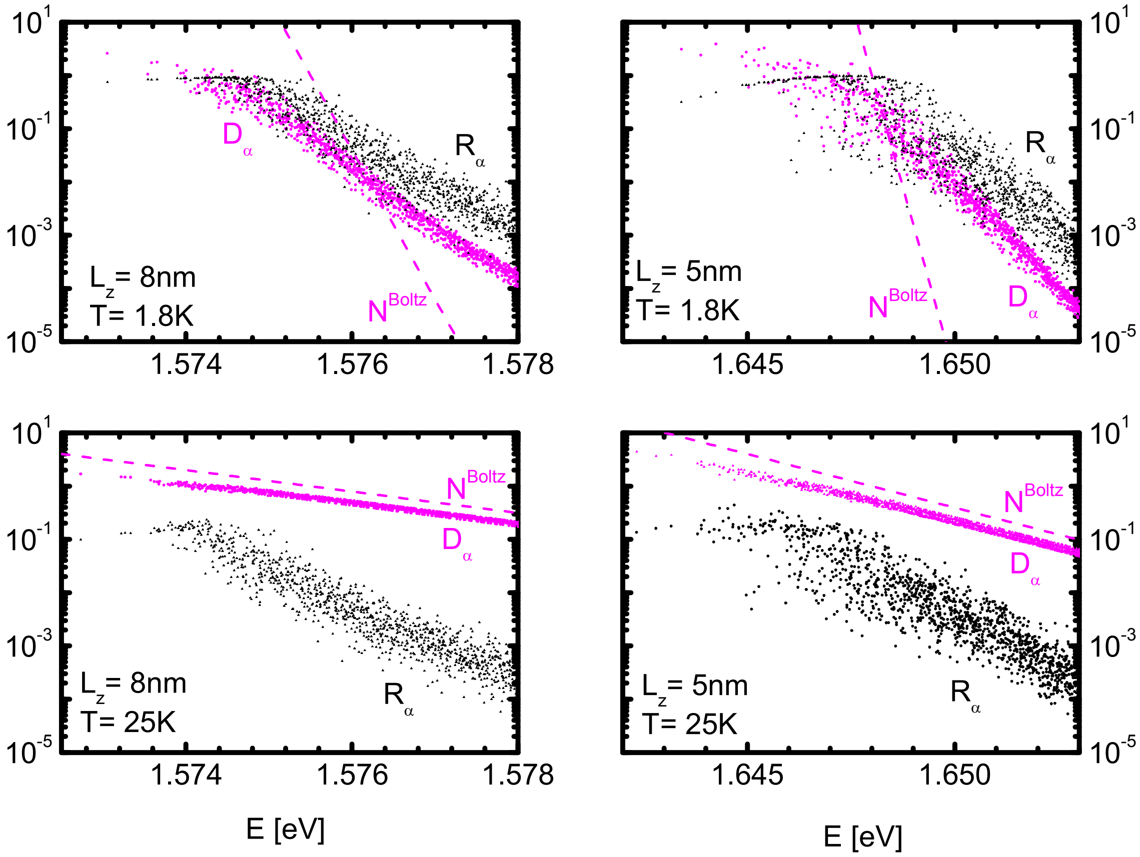

Figure 3.4: *Incoherent density* D_α *(magenta symbols) and source term* R_α *(black symbols) for a 8 nm (left panels) and 5 nm wide (right panels) QW at* $T = 1.8$ *K and* $T = 25$ *K. The Boltzmann distribution* N^{Boltz} *is plotted as a dashed line.*

Still we can distinguish a diagonal contribution, that will allow us to define an incoherent intensity and thus a coherence degree of the frequency resolved SE, cp. Eq. (2.5). The spectral speckle pattern is given by the time averaged quantity $I_{\mathbf{k}}(\omega) = \int dt\, I_{\mathbf{k}}(t,\omega)$. For computing it we need to specify the spectrometer response function. For algebraic simplicity we use as response function $\mathcal{G}(\omega,t) = \theta(t)\exp((i\omega-\delta)t)$, but the final result will not depend on it, since we will take the limit of ideal resolution, $\delta \to 0$. This leads to the expected separation of coherent and incoherent intensity,

$$I_{\mathbf{k}}(\omega) = I^{\mathrm{inc}}(\omega) + I^{\mathrm{coh}}_{\mathbf{k}}(\omega)\,. \tag{3.43}$$

The incoherent intensity is produced by the radiative recombination of the incoherent exciton density,

$$I^{\mathrm{inc}}(\omega) = \sum_\alpha |m_{\alpha\mathbf{k}}|^2 \frac{\Gamma_\alpha}{(\omega-\omega_\alpha)^2+\Gamma_\alpha^2} D_\alpha\,. \tag{3.44}$$

The integrated density $D_\alpha = \int dt\, D_{\alpha\alpha}(t)$ satisfies

$$0 = \sum_\eta \gamma_{\alpha\leftarrow\eta}\left[R_\eta + D_\eta\right] - 2\Gamma_\alpha D_\alpha\,, \tag{3.45}$$

where $R_\alpha = \int dt\,|P_\alpha(t)|^2$ is the coherent population defined by Eq. (B.25). As proved in App. (B.5), for high phonon temperature, D_α approaches an equilibrium distribution. This is clearly seen in Fig. 3.4, where the incoherent exciton density is compared to the Boltzmann distribution.
The speckling results from (normal incidence excitation)

$$I_{\mathbf{k}}^{\mathrm{coh}}(\omega) = E_{\mathrm{in}}^2(\omega) \sum_{\alpha\beta} m_{\alpha\mathbf{k}}^* m_{\beta\mathbf{k}} m_{\alpha 0} m_{\beta 0}^* \frac{1/2}{(\omega - \omega_\alpha - i\Gamma_\alpha)(\omega - \omega_\beta + i\Gamma_\beta)} \tag{3.46}$$

with the Fourier transform $E_{\mathrm{in}}(\omega)$ of the laser pulse envelope $E_{\mathrm{in}}(t)$. The speckle average (i.e., over $\mathbf{k}$) of the coherent intensity is the Rayleigh spectrum which, replacing $(m_{\alpha 0}/\hbar)^2 \to r_\alpha$ (localized states approximation, cp. App. (B.3)), reads

$$\left\langle I_{\mathbf{k}}^{\mathrm{coh}}(\omega) \right\rangle_{\mathbf{k}} = E_{\mathrm{in}}^2(\omega) \sum_\alpha \frac{r_\alpha^2}{2} \frac{1}{(\omega - \omega_\alpha)^2 + \Gamma_\alpha^2} \,. \tag{3.47}$$

This RRS is resonant with the excitation, as expected [41]. The frequency resolved coherence degree, given by application of Eq. (2.5) in the spectral domain, is then

$$c(\omega) = \frac{\left\langle I_{\mathbf{k}}^{\mathrm{coh}}(\omega) \right\rangle_{\mathbf{k}}}{\left\langle I_{\mathbf{k}}^{\mathrm{coh}}(\omega) \right\rangle_{\mathbf{k}} + I^{\mathrm{inc}}(\omega)} \,. \tag{3.48}$$

3.5 Intensity correlation

As already mentioned, further information can be extracted from the speckle pattern when the speckle correlation function is computed. Correlating intensities at detuned frequencies, we will gain information about the total dephasing rates within the inhomogeneously broadened exciton resonance.
We consider the correlation function

$$C(\omega, \Delta\omega) = \frac{\langle I_{\mathbf{k}}(\omega - \Delta\omega/2) I_{\mathbf{k}}(\omega + \Delta\omega/2) \rangle_{\mathbf{k}}}{\langle I_{\mathbf{k}}(\omega - \Delta\omega/2) \rangle_{\mathbf{k}} \cdot \langle I_{\mathbf{k}}(\omega + \Delta\omega/2) \rangle_{\mathbf{k}}} - 1 \,, \tag{3.49}$$

As proved in App. (A.2), in the numerator it suffices to consider the coherent intensity. The numerator is then given by $E_{\mathrm{in}}^2(\omega) E_{\mathrm{in}}^2(\omega + \Delta\omega)\; |\xi(\omega, \Delta\omega)|^2$ with the auxiliary correlation function ($(m_{\alpha 0}/\hbar)^2 \to r_\alpha$)

$$\xi(\omega, \Delta\omega) = \sum_\alpha \frac{r_\alpha^2/2}{(\omega - \Delta\omega/2 - \omega_\alpha - i\Gamma_\alpha)(\omega + \Delta\omega/2 - \omega_\alpha + i\Gamma_\alpha)} \,. \tag{3.50}$$

Putting all statistical information into a compound distribution

$$W(\Omega, \Gamma) = \frac{1}{2} \sum_\alpha r_\alpha^2\, \delta(\Omega - \omega_\alpha)\, \delta(\Gamma - \Gamma_\alpha) \,, \tag{3.51}$$

we rewrite $\xi(\omega, \Delta\omega)$ as

$$\xi(\omega, \Delta\omega) = \int d\Omega\, d\Gamma\, \frac{W(\Omega, \Gamma)}{(\omega - \Delta\omega/2 - \Omega - i\Gamma)(\omega + \Delta\omega/2 - \Omega + i\Gamma)} \,. \tag{3.52}$$

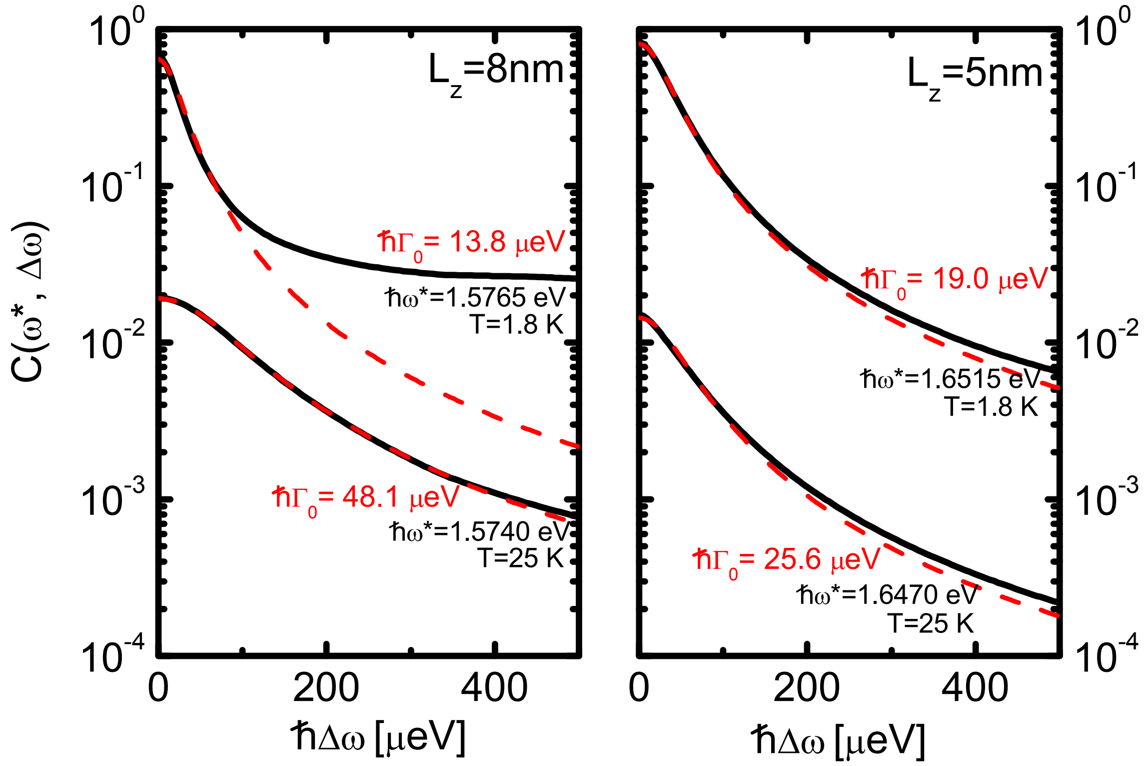

Figure 3.5: *Sections of the correlation functions $C(\omega^*, \Delta\omega)$ at the frequency ω^* for which the coherence degree $c(\omega)$ is maximum. Simulations for the 8 nm and 5 nm QW at different temperatures (black solid lines) are compared to Lorentz fits (red dashed lines) according to the expression Eq. (3.53). The corresponding fit parameters Γ_0 are given.*

Thus, the correlation function depends on the distribution of exciton energies ω_α and dephasing rates Γ_α and their mutual correlation, as given by $W(\Omega, \Gamma)$. At this point we simplify the treatment by assuming two approximations to hold:
i) Large inhomogeneous broadening $\sigma \gg \Gamma_\alpha$.
Since the magnitude of the Γ_α's sets the range $\Delta\omega \approx 2\Gamma_\alpha$ of $\xi(\Delta\omega)$, this approximation allows to neglect the exciton energy dependence: $W(\Omega, \Gamma) \approx W(\omega, \Gamma)$ for $|\Omega - \omega| \lesssim \Delta\omega$. Furthermore, the denominator in Eq. (3.49) can be evaluated at $\Delta\omega = 0$, since the SE spectra that appear there have widths of the order of $\sigma \gg \Delta\omega$.
ii) Negligible distribution of the Γ_α's at fixed energy.
As shown in Fig. 3.8, even at fixed exciton energy, the dephasing rates Γ_α are spread into a cloud. Approximating this distribution with an energy dependent mean value $\Gamma_0(\omega)$, $W(\omega, \Gamma) \approx A_\omega\, \delta(\Gamma - \Gamma_0(\omega))$, the pole contributions in Eq. (3.52) can be evaluated in a straightforward way.
Applying both i) and ii) we end up with

$$C(\omega, \Delta\omega) = c^2(\omega) \frac{1}{1 + \left(\dfrac{\Delta\omega}{2\Gamma_0(\omega)}\right)^2} \, . \tag{3.53}$$

Apart of the expected normalization $C(\omega, 0) = c^2(\omega)$, we find that the dependence on the detuning $\Delta\omega$ is of Lorentzian type. Thus, we decide to extract the homogeneous broadening as the "quarter-width" half maximum of the speckle correlation as a function of $\Delta\omega$: this value coincides with $\Gamma_0(\omega)$ if $C(\omega, \Delta\omega)$ is a good Lorentzian in $\Delta\omega$. In Fig. 3.5 it is seen that this is a fair approximation, though deviations in the tail are noticed, especially for the 8nm QW. This sample is less disordered and thus poorly satisfies approximation (i).
Further refinements are possible, for instance by modelling the distribution of dephasing rates Γ_α at fixed energy, but they lead for realistic parameters to minor deviations. Much more important is the effect of the finite spectral resolution in the experiment. The detected intensity is a convolution of the emitted intensity and the detector response function f_ω, which is a Voigt profile,

$$\mathcal{V}(\omega, \gamma_D, \sigma_D) = \frac{1}{N} \int d\omega' \frac{\exp\left(-\frac{(\omega'-\omega)^2}{2\sigma_D^2}\right)}{\omega'^2 + \gamma_D^2} . \tag{3.54}$$

The Lorentzian and Gaussian parts have FWHM $4\hbar\gamma_D$ and $\hbar\sigma_D\sqrt{8\ln 2}$, respectively; N is the normalization constant. The Lorentzian part results from the diffraction limit of the grating spectrometer, while the Gaussian part originates from finite input slit size, detector pixel size, and optical aberrations altogether [35]. Now, the correlation function $C_D(\Delta\omega)$ computed from the detected intensities can be shown to be the convolution of the correlation function $C(\Delta\omega)$, computed out of the emitted intensities, with the self-convolution of the response function f_ω. If $C(\Delta\omega)$ is the Lorentzian given by Eq. (3.53) , $C_D(\Delta\omega)$ is then proportional to a Voigt profile $\mathcal{V}(\Delta\omega, 2\Gamma_0(\omega) + 2\gamma_D, \sqrt{2}\sigma_D)$. Thus, the finite spectral resolution leads to a overestimation of the dephasing rates $\Gamma_0(\omega)$ [30]. In the used experimental setup, the response function was characterized with $\hbar\gamma_D = 1.8\mu\text{eV}$ and $\hbar\sigma_D = 9.6\mu\text{eV}$, and the rates $\Gamma_0(\omega)$ could be extracted through a Voigt fit of $C_D(\Delta\omega)$ and are shown in Fig. 3.8.

3.6 Comparison with the experiment

The investigated samples are GaAs/$\text{Al}_{0.3}\text{Ga}_{0.7}$As single quantum wells (SQW) of various thicknesses grown by molecular beam epitaxy (MBE). They were kept at temperatures between 1.8 K and 25 K. All data were taken through an analyzer parallel to the linearly polarized excitation impinging on the sample in Brewster angle, in a directional range centred normal to the sample. The directionally and spectrally resolved SE intensities are shown in Fig. 3.6 for the dominantly inhomogeneously broadened excitonic transitions in the investigated SQW, which have SE linewidths (FWHM) of 0.94 meV and 3 meV for the 8 nm and the 5 nm SQW respectively. After averaging over about 10^{10} laser pulses, the incoherent intensity contributes as a direction-independent background, and $\left\langle I_{\mathbf{k}}^{\text{coh}}(\omega)\right\rangle_{\mathbf{k}}$ is proportional to the intensity contrast, Eq. (3.48). This allows to extract the RRS from the total SE at any frequency of the spectrum, with an accuracy increasing with the number of collected speckles (about 4000 speckles in our case).

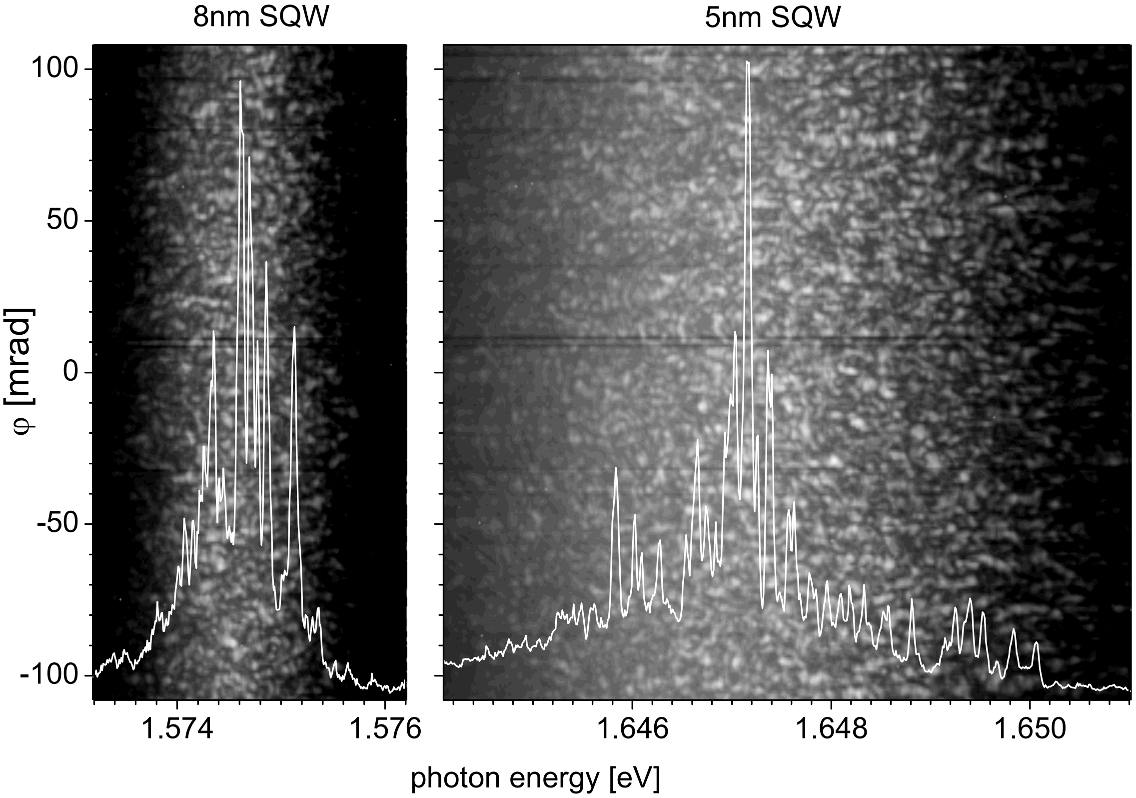

Figure 3.6: *Directionally and spectrally resolved emission intensity (2 decades logarithmic grey scale) of the 8 nm and 5 nm GaAs SQW at T=1.5 K. The white lines are examples of spectra at fixed emission directions. Figure after [30].*

For comparing to the experimental data, we have calculated eigenstates $\psi_\alpha(\mathbf{R})$ (Fig. 3.2) and eigenenergies $\epsilon_\alpha^{(0)}$ on a square simulation area using a grid-step $\Delta_x = a_B/6$ [5]. The correlation length of the disorder potential is related to the exciton Bohr radius in the well a_B, which is given for different well widths in Tab. 3.1. As long as the monolayer island size is below a_B, both inverted and normal interface add up to give a single potential variance $\hbar\sigma$. This is our *sole* free parameter, which is adjusted to fit the RRS spectrum at low temperature, giving $\hbar\sigma$ values according to Tab. 3.1 for the different QW. We use material constants after [56]. The kinetic equation Eq. (3.45) has been solved and the coherent and incoherent intensities were evaluated according to Eq. (3.47) and Eq. (3.44) respectively.

Results from a large number N_{real} (see Tab. 3.1) of disorder realizations have been added to obtain the dashed curves in Fig. 3.7, where we compare them with the experimental results [6] at two different lattice temperatures.

The peak positions of the simulated SE are adjusted on the experimental ones. They reflect the ideal exciton energy, which depends on confinement effects ($\sim L_z^{-2}$) as well as on temperature (redshift of the Gap energy [2]). The spectral width of the

---

[5] Diagonalization of the problem Eq. (3.5) was numerically achieved within the package PR98WAVE by E. Runge, who is kindly acknowledged.

[6] Experimental data for the 5 nm SQW at 25 K are published in the PhD-Thesis by G. Kocherscheidt [29].

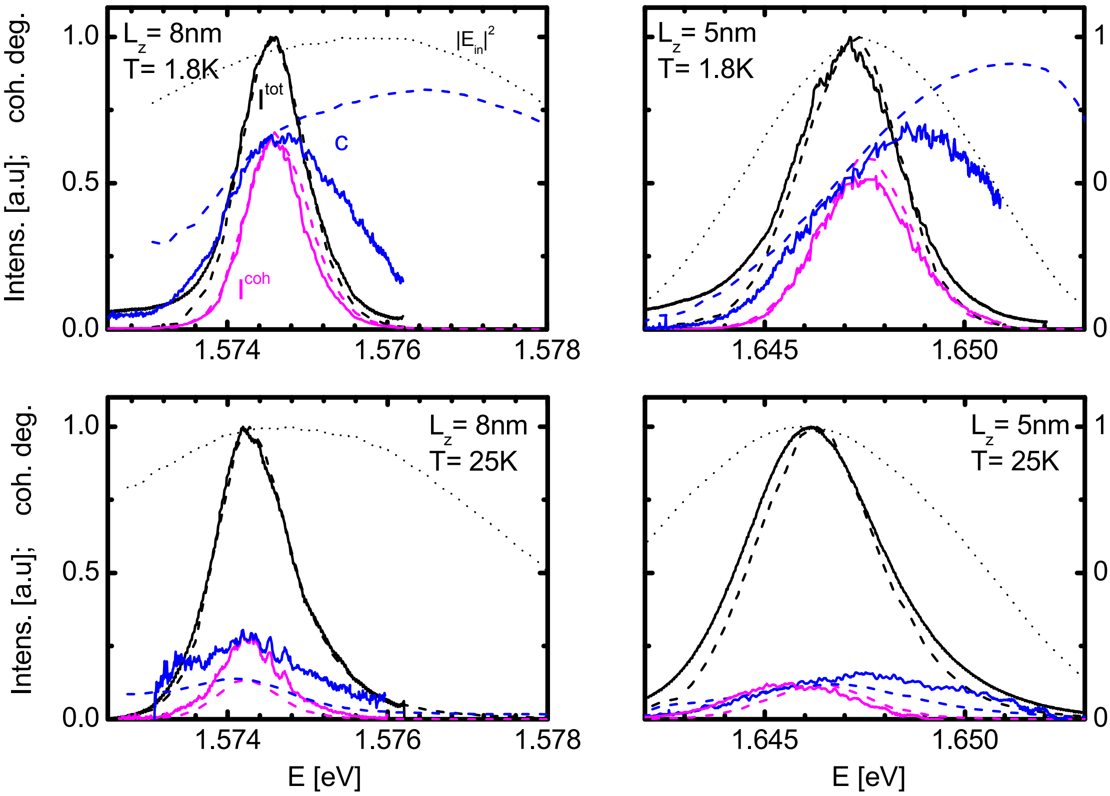

Figure 3.7: *Comparison of experimental (solid) and simulated (dashed) spectral results for the 5 and 8 nm wide QW at two phonon temperatures. Laser spectrum* $|E_{\text{in}}|^2$ *,speckle averaged secondary emission* I^{tot} *(black), coherent part* I^{coh} *(magenta), and coherence degree c (blue).*

SE is larger in the 5nm SQW because of the larger interface disorder. The RRS intensity drops with increasing temperature, as a consequence of the increased phonon scattering. This effect is more important for the 5nm SQW, in which the dephasing is phonon dominated. The coherence degree c is maximum at the centre and vanishes in the low energy tail of the resonances. This is due to the piling of the exciton population D_α that has experienced (phase-destroying) phonon scattering, Fig. 3.4. The drop of $c(\omega)$ on the high energy side is not trivial and is discussed later (cp. Fig. 3.9).

In general, the agreement between experimental results and simulations is rather good, though full quantitative agreement is not always reached. At this place we have to recall that the simulations have only one free parameter, the disorder variance $\hbar\sigma$, and we have adopted the policy not to tune the material constants, but to take them from the existing literature [56].

For obtaining these spectra the coherent and incoherent exciton densities have to be computed first and were shown in Fig. 3.4. The coherent exciton density R_α sharply drops with energy because the phonon scattering dominates the ratio $r_\alpha/2\Gamma_\alpha$ for higher energies (see Eq. (B.25)). The incoherent density D_α is in thermal equilibrium with the lattice at $T_{\text{ph}} = 25$K, but not at $T_{\text{ph}} = 1.8$K: at low temperatures, there are not enough phonon scattering events during the radiative lifetime of the

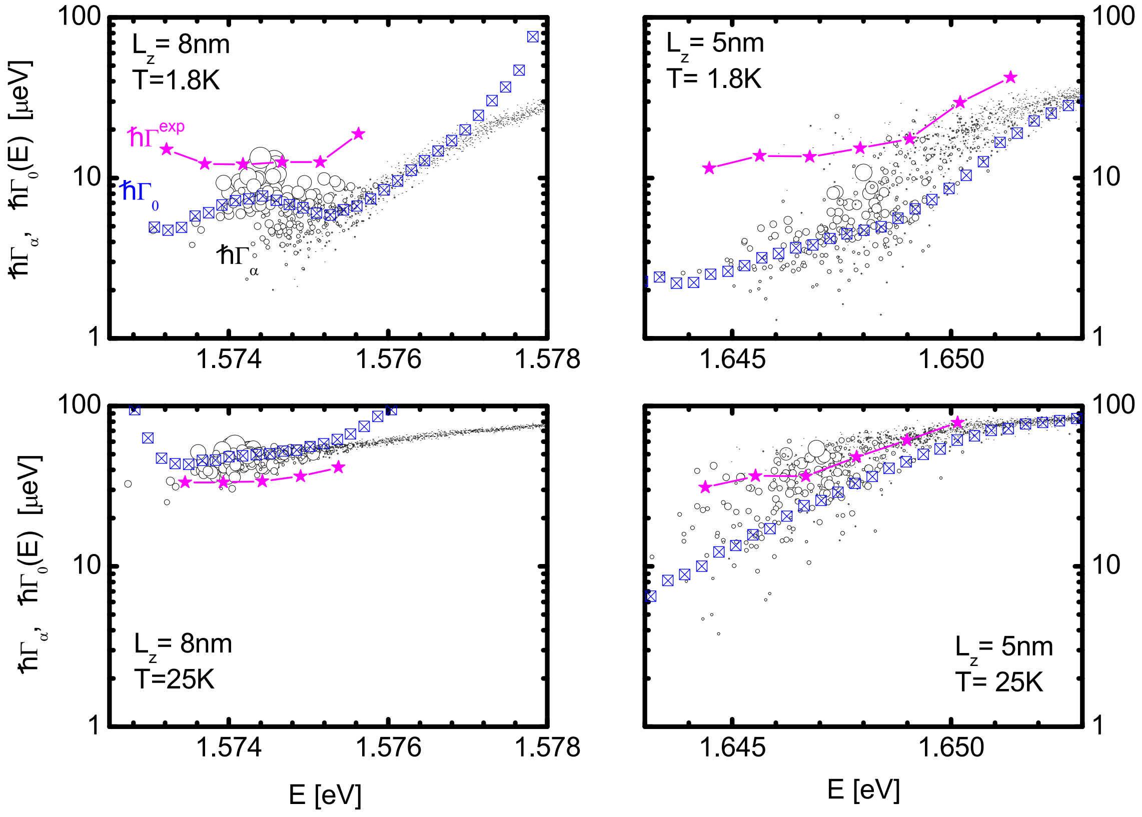

Figure 3.8: *Comparison of experimental (magenta stars) and simulated (blue crossed boxes) dephasing rates* $\Gamma_0(\omega)$ *for the 5 and 8 nm wide QW at two phonon temperatures. The individual total dephasing rates* Γ_α *resulting form the simulations are plotted as circles with radius proportional to the radiative part* r_α*.*

excitons to achieve thermalization.

As shown in Sect. (3.5), from these data the frequency resolved homogeneous broadening $\Gamma_0(\omega)$ can be extracted. In Fig. 3.8 we compare experimental and simulation results. The resulting rates are in the range 5-100 μeV. We notice that we move between a radiative dominated dephasing in the 8 nm QW at low temperature to a phonon dominated situation for the 5 nm QW at high temperature. This is clearly seen from the radii of the individual relaxation rates Γ_α, which are proportional to the radiative part r_α. The difference between mainly radiative and mainly phononic dephasing is especially striking in the low energy region, where the phonon rates are small. Thinner QW have more localized states; thus their size in momentum space can exceed the light-cone size, leading to a reduction of the radiative rates (cp. App. (B.3)). On the other side, thinner QW have more extended confinement wavefunctions along growth direction. Thus a coupling to a larger range of phonon states is present (cp. App. (B.1)). In general, the simulated results reproduce the trend observed in the experiment; quantitative disagreement could be due to the used material constants or to neglect of other dephasing mechanisms possibly present in the experiment.

We finally address the question of the coherence degree $c(\omega)$.

As already mentioned, $c(\omega)$ decreases on the low-energy tail at any temperature

L_z [nm]	$\hbar\sigma$ [meV]	Δ_x [nm]	N_{size}	N_{psi}	N_{real}
5	4.750	1.65	128	300	493
8	1.800	1.78	128	200	412
15	0.283	2.07	256	150	40

Table 3.1: *Parameters used in the simulations for different QW widths L_z: potential variance $\hbar\sigma$, grid-step Δ_x, number of grid step along each spatial dimension N_{size}, number of computed eigenstates for each realization N_{psi}, number of realizations N_{real}.*

because the incoherent density D_α piles there as a consequence of phonon emission processes. At high temperature phonon absorption comes into play as well and thus the coherence degree decreases also on the high energy tail, having a maximum at the centre of the excitation spectrum. According to this argument, $c(\omega)$ should be maximum on the high-energy tail for low temperature, since in this case phonon in-scattering is suppressed. The vanishing coherence degree in the top panels Fig. 3.7 is in contrast with this simple explanation. The reason for this is that especially the incoherent intensity can profit from the finite homogeneous linewidths Γ_α which are used for the Lorentz broadening of the intensities (cp. Eq. (3.44) and Eq. (3.47)). This is proved with the results shown in Fig. 3.9, where spectra with and without broadening are computed. At low temperature, this makes a huge difference and it is seen that the coherence degree can actually reach unity, in the absence of broadening. A further reduction of $c(\omega)$ in the experimental data of Fig. 3.7 comes from the finite bandwidth of the laser pulses. It is therefore important to use the recorded laser spectrum $|E_{\mathrm{in}}(\omega)|^2$ in the numerical simulations, as we have done throughout.

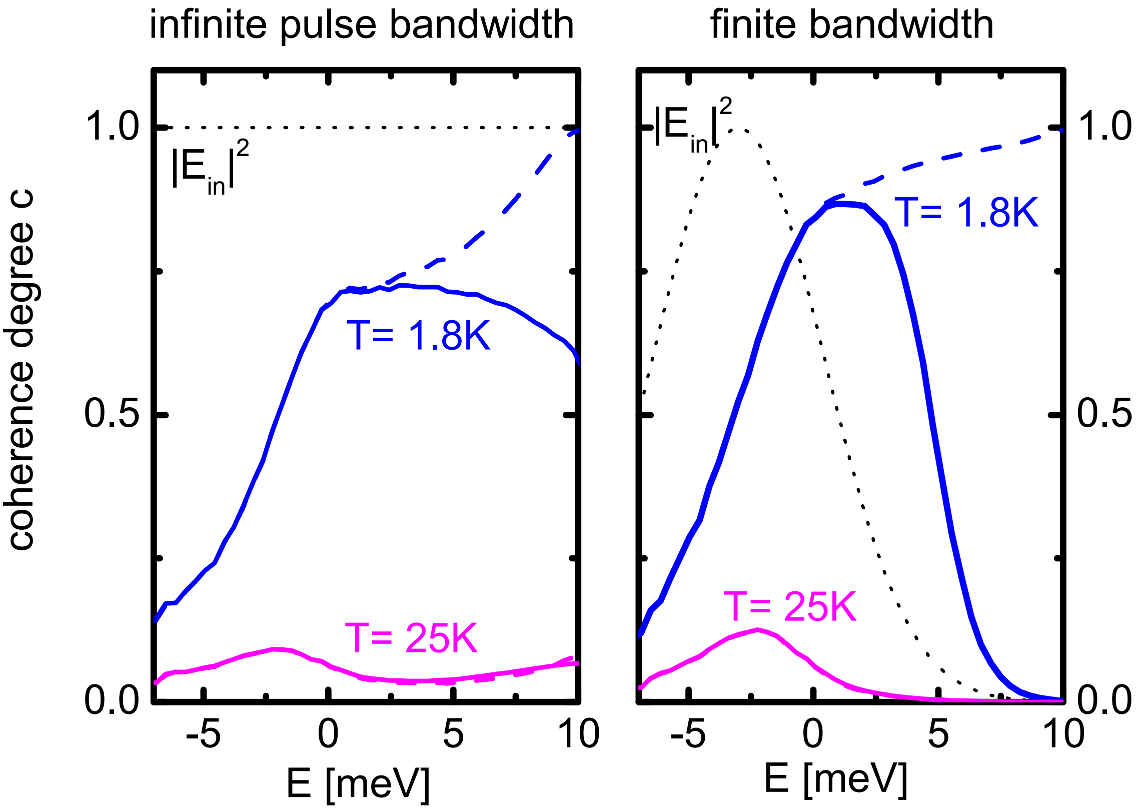

Figure 3.9: *Coherence degree c in presence (solid lines) and without Lorentz broadening (dashed lines) at $T = 1.8\,K$ (blue data) and $T = 25\,K$ (magenta). Laser spectrum as dotted lines. Left panel: for delta-like excitation; right panel: using Gaussian pulses with spectral $FWHM = 8\,meV$.*

Chapter 4

Sloped Speckles

Semiconductor nanostructures are sometimes affected by various types of mechanical stress. While in some cases this is regarded as a defect or an unwanted feature, there is also the possibility to exploit stress for tailoring transport and optical properties [17, 59], thus improving the performance of nano-devices such as low threshold laser diodes, metal-oxide-semiconductor devices and near-infrared detectors [40].

In this Chapter we discuss the consequences of in-plane stress in a semiconductor QW, applied by the purpose of modifying the optical properties of the sample. Both experimental and simulation results are presented. The most prominent effect of stress for the SE is the tilting of the speckle pattern in the momentum-time space. These *sloped speckles* allow to measure local gradients of the long-range potential created by the stress. Though this information could be achieved also via space-resolved PL, the speckle technique relies only on coherent emission, which makes interpretation of data easier, and is done in the far-field, allowing in principle for imaging-free detection (this feature is exploited in soft X-ray scattering techniques, cp. [48] and references therein).

While the experimental results mostly concern with the SE, numerical simulations allow also to verify or confute speculations about exciton motion in such a strained sample. Stress indeed induces long-range potentials that could push the excitonic wavepacket down to regions of lower potential energy. The competition between this force and the "friction" resulting from in-plane disorder decides whether exciton delocalization takes place. Though this is not the case in the experimentally realized situation, it is found that delocalization can occur for large potential gradients and weak disorder.

4.1 Experiment

A sample containing GaAs SQW of various thicknesses with a barrier material $Al_{0.3}Ga_{0.7}As$ was investigated [43]. The sample was grown by MBE on undoped [001] oriented GaAs substrate of about $500\,\mu$m thickness. Cleaving along the [110] and $[1\bar{1}0]$ natural cleavage planes formed a $5\times5\,\mathrm{mm}^2$ square piece. Strain along the [100] in-plane direction was created by applying a force of several Newton at two opposite corners of the sample (see inset of Fig. 4.1). Due to the changing cross-section along the [100] direction, a varying spatial strain profile is created. The sample was placed

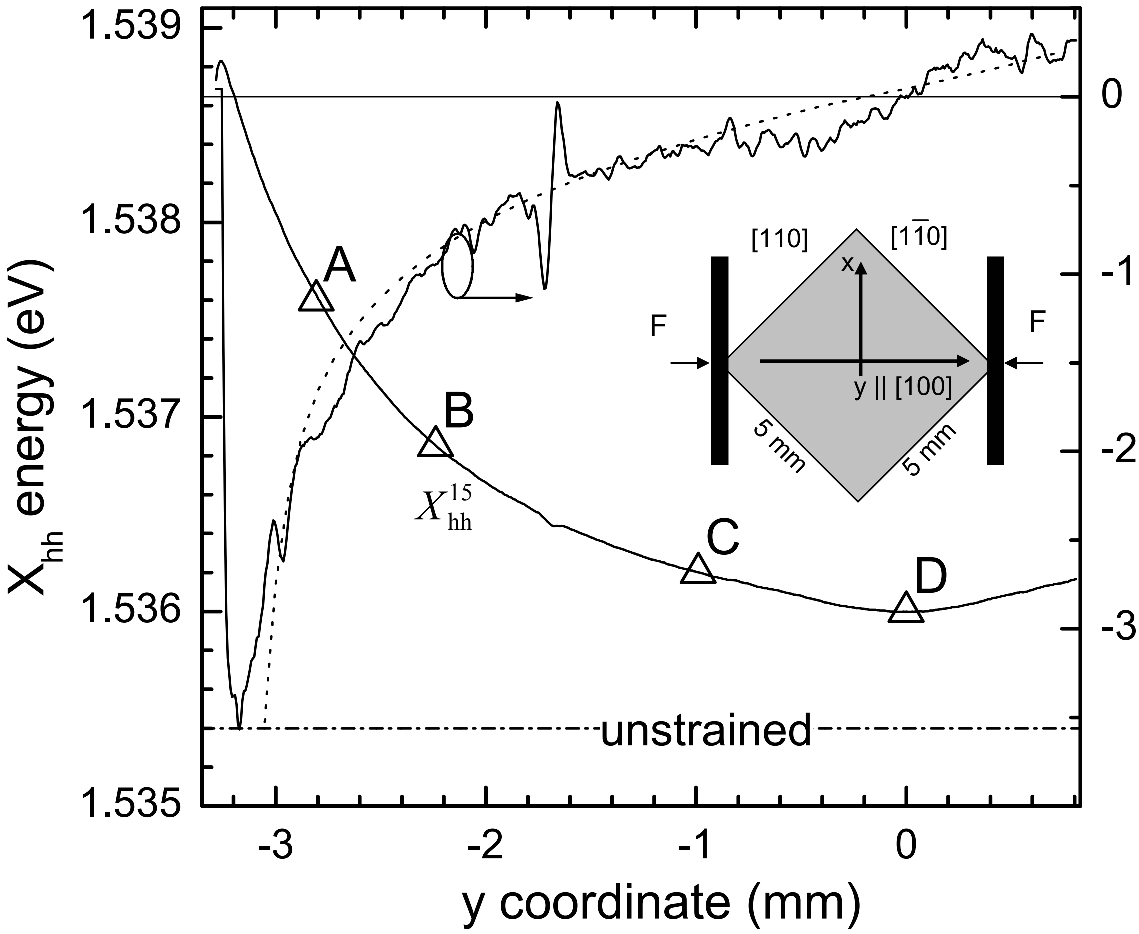

Figure 4.1: *Non-resonantly excited PL intensity at T=5*K *showing the spectral position of the heavy-hole (HH) exciton in the 15*nm *QW and its gradient along the sample diagonal* $(0, y)$. *The transition energy of the unstrained sample is displayed as a dot-dashed straight line. Selected points for the speckle measurements are indicated. The dotted line refers to the result of a* $\mathbf{k} \cdot \mathbf{p}$ *calculation. Inset: Schematic drawing of the sample and geometry of the applied force* F.

in a helium cryostat and kept at a temperature of 5 K. The fundamental HH1-E1 1s exciton resonance was resonantly excited p-polarized in the Brewster angle direction by optical laser pulses from a mode-locked Ti:sapphire laser of about 1 ps duration. The excitation spot diameter was chosen to be about 400 μm, the size of a region in which the strain gradient is well described by a parabolic behaviour. The SE in a directional range around the sample normal was imaged into two different detection systems. To measure the spatially resolved emission spectra, the sample near-field was imaged onto the input slit of a spectrometer with 20 μeV spectral resolution, and the intensity was detected by a cooled Si CCD array. The dimension along the slit was used to create a one-dimensional spatial image. Two dimensional (x, y) spatial images of the emission spectra were taken by scanning along the direction orthogonal to the slit. To measure the directionally and temporally resolved emission intensity, the emission far-field was imaged onto another imaging monochromator and its intensity was detected time, energy, and directionally resolved by a synchroscan streak camera. Using the second dimension of the streak-camera, the RRS dynamics can be directionally resolved in one dimension, resulting in the parallel detection of about 100 speckles. Scanning along the other dimension again enabled to take data of the emission intensity resolved in two directional (k_x, k_y) dimensions and in the temporal dimension. One of the resonances of the spatially and spectrally resolved, non-resonantly excited photoluminescence (PL) of intensity $I_{\mathrm{PL}}(x, y, \hbar\omega)$ along the sample diagonal $(0, y)$ is shown in Fig. 4.1. It is due to the HH exciton of the 15 nm wide QW (X^{15}_{hh}). The applied stress leads to a spatial variation of the resonance energies. Due to the mirror symmetry of the strain configuration, the gradient vanishes in the sample centre, creating a minimum of the resonance energies. Experiments on several exciton resonances were performed. Here we focus on the X^{15}_{hh} transition, whose energy gradient along the sample diagonal is given in Fig. 4.1. In particular four positions A, B, C, and D have been selected to exhibit different local energy gradients and curvatures.

The spatial variation of the resonance energy translates into the speckle dynamics. The directionally and time-resolved SE intensity $I(k_x, k_y, t)$ is measured for resonant excitation at different positions on the sample. An example taken at position A for various times after excitation is shown in Fig. 4.2(a). The observed strong speckle contrast reflects the large degree of coherence of the emission for short times after excitation. The temporal dynamics of the speckle pattern is apparent in the images of $I(k_x = 0, k_y, t)$ in Fig. 4.2(b). While in the case of a negligible energy gradient (position D) the speckle pattern streaks horizontally, for large gradients (position A) the pattern is tilted, i.e. it acquires a temporal shift along the energy gradient direction k_y. The temporal and directional speckles contain thus information on the local energy gradients in the sample.

4.2 QW with strain

In the experiment, the mechanical stress induced by the screws leads to a spatial dependent exciton transition energy, as seen in the space-resolved PL measurement of Fig. 4.1. This can be explained in terms of a spatially dependent crystal band structure which gives place to an extra potential for the exciton. In [43] a finite element method calculation was performed for modelling the strain tensor $\hat{\epsilon}(x, y)$ in the actual experimental geometry. $\hat{\epsilon}(x, y)$ was then employed in a $\mathbf{k} \cdot \mathbf{p}$ calculation for computing the exciton transition energy and the space dependent light-heavy hole splitting. The result was compared to the experiment in Fig. 4.1.

Thus, the minimal requirement for a theoretical description of the resulting sloped speckle patterns is inclusion of disorder effects and the systematic in-plane potential arising from the strain. We will neglect here the exciton phonon interaction: thanks to the speckle results we know that, at the low temperature at which the experiment was carried out, the SE is dominated by the coherent emission, at least for not too long times after excitation Fig. 4.2(c). We also neglect the radiative damping of the emission. As in Chapter 3, the relevant degrees of freedom in the energy window of interest will be the 1s exciton in-plane COM coordinates $\mathbf{R}$.

With these ingredients we can derive (App. (C.1)) an equation of motion for the

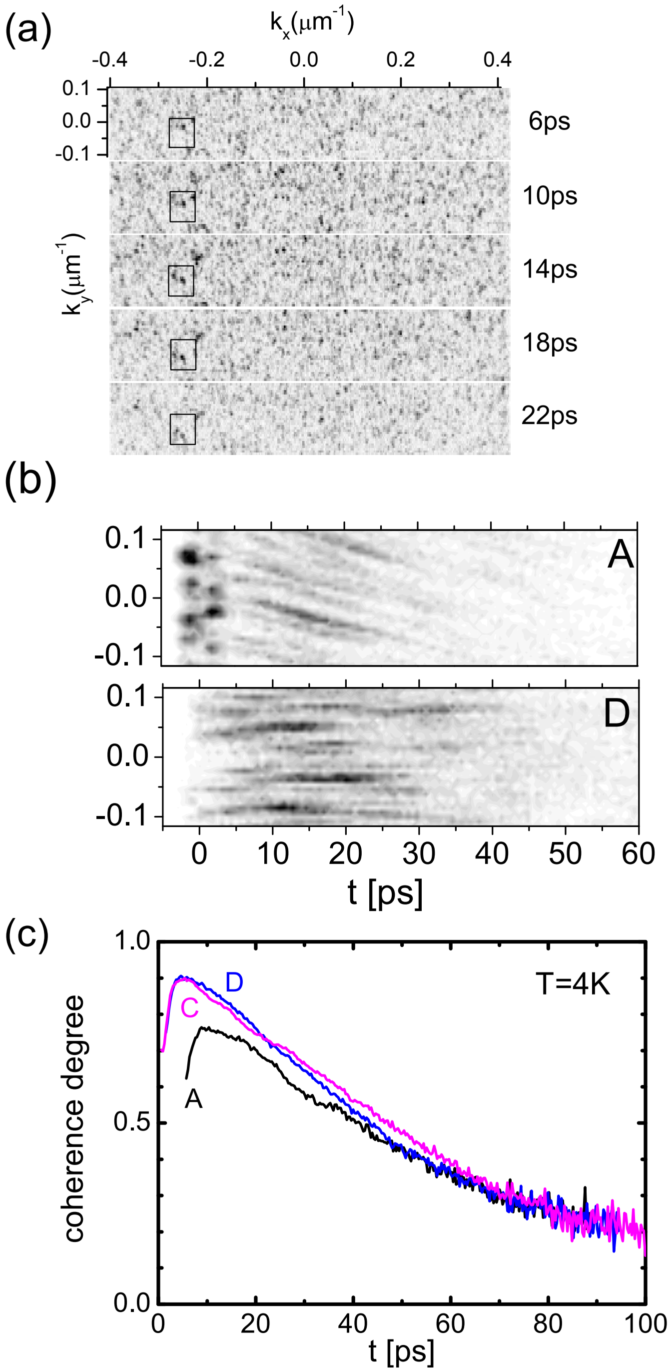

Figure 4.2: *Directionally resolved SE intensity* $I(k_x, k_y, t)$ *on a linear gray-scale after pulsed resonant excitation of the* X_{hh}^{15} *resonance. (a): As function of* k_x *and* k_y *at fixed delay times* t *as indicated, at position A. Rectangles at constant position are shown to visualize the speckle shift. (b): At* $k_x = 0$ *as function of* k_y *and time* t*, at positions A and D. (c): Coherence degree dynamics* $c(t)$ *at positions A, C, D. Data for* $t \lesssim 5\,ps$ *at position A are missing because of strong surface scattering (cp. panel A of part(b)).*

exciton polarization, which is a time-dependent Schrödinger equation with a source term proportional to the electrical field of the exciting laser pulse,

$$(i\hbar\partial_t + H_0(\mathbf{R}) + Z(\mathbf{R}))\, P(\mathbf{R},t) = \mu_{\mathrm{cv}} E_{\mathrm{in}}(\mathbf{R},t) e^{-i\omega_{\mathrm{in}}t}\,. \tag{4.1}$$

Here we have separated the Hamiltonian of a unstrained system with white noise disorder $W(\mathbf{R})$,

$$H_0(\mathbf{R}) = -\frac{\hbar^2 \Delta_{\mathbf{R}}}{2M} + W(\mathbf{R})\,, \tag{4.2}$$

from the potential $Z(\mathbf{R})$ introduced by the strain. We also notice that Eq. (4.1) is formally identical to the equation of motion Eq. (3.34) for the polarization in the disorder basis. In the following just the linear and the quadratic part of a Taylor expansion of the systematic potential $Z(\mathbf{R})$ will be considered,

$$Z(\mathbf{R}) = \hbar\mathbf{g}\cdot\mathbf{R} + \hbar R_i f_{ij} R_j\,. \tag{4.3}$$

The main axes of the tensor f_{ij} are along the direction of the gradient $\mathbf{g}$ and its normal.

4.3 Exact results without disorder

It is important to clarify first the situation expected in the absence of disorder, distinguishing the discrete case, that arises when we attempt to solve the problem numerically, from the continuum case, in which differentiation and integration are defined in the usual way.

In the continuum case, there are different methods for retrieving an exact solution for the problem Eq. (4.1). If we are interested in the real space dynamics, an expansion of the polarization in terms of Airy functions (in case of linear potential $Z(\mathbf{R})$) or in terms of eigenstates of the harmonic oscillator (for quadratic $Z(\mathbf{R})$) allows to retrieve the result. Actually, we are mostly interested in the dynamics in momentum space, since finally we would like to discuss the experimental results for the speckle [1] dynamics in the $(\mathbf{k},t)$ plane. In this case, an analytical result can be found if we restrict ourselves to the case of linear potential. Further, no information is lost if we consider a one-dimensional problem, since only the direction of the gradient $\hbar\,\mathbf{g}$ of the systematic potential is relevant. After delta pulse excitation at $t = 0$, the problem to be solved is thus ($g = |\mathbf{g}|$)

$$\left(i\hbar\partial_t - \frac{\hbar^2\partial_y^2}{2M} + \hbar g y\right) P(y,t) = 0\,, \tag{4.4}$$

with initial condition $P(y,0^+) = -(i/\hbar)\,E_{\mathrm{in}}(y)$. The solution is easily achieved by a Fourier transformation, as outlined in App. (C.2). The final result is that the coherent intensity $I = |P|^2$ depends only on the Fourier transform of the envelope of the excitation pulse, according to

$$I(k,t) = \hbar^{-2}\, E_{\mathrm{in}}^2(k+gt)\,. \tag{4.5}$$

---

[1] Strictly speaking, there is only one super-speckle in case disorder is absent. Indeed QW in-plane translation symmetry is preserved and the SE consists of the sole emission in specular direction.

This simple results describes a SE which drifts in the momentum-time plane, without changing shape and with a momentum acceleration $\hbar\, dk/dt$ given by the slope $\hbar g$ of the potential gradient. In case of Gaussian excitation spot, $E_{\rm in}(y) = \exp(-y^2/2\Phi^2)$, also the dynamics in real space can be calculated analytically. Fourier back-transforming the obtained $P(k,t)$ we arrive to

$$I(y,t) = \frac{1}{\hbar^2 S_{\rm lin}(t)} \exp\left(- \left(\frac{y - (\hbar g/2M)t^2}{\Phi S_{\rm lin}(t)} \right)^2 \right) \tag{4.6}$$

where $S^2_{\rm lin}(t) = 1 + (\hbar t/M\Phi)^2$. As time goes by, the exciton packet broadens, while sliding down along the potential gradient like a point mass M under action of a force $\hbar\mathbf{g}$ in classical mechanics.

In the discrete case, a tight-binding approach shows (App. (C.3)) that the constant force leads to Bloch oscillations of the probability density, centred at

$$y_c(t) = \frac{4T_0}{\hbar g} \sin^2(tg\Delta_x/2)\,, \tag{4.7}$$

with $T_0 = \hbar^2/(2M\Delta_x^2)$ being the "transfer energy" in a mesh with grid step Δ_x. The continuum case is reached as the limit in which Δ_x vanishes, for which we retrieve the ballistic motion,

$$y_c(t) \approx \frac{1}{2}\frac{\hbar g}{M} t^2\,. \tag{4.8}$$

4.4 Numerical results

For the description of the experimental data, the disorder free results are obviously not sufficient. Thus, we resort to a numerical integration of Eq. (4.1).

We compare the numerical results with the experiment at the positions A, B, C, and D of Fig. 4.1. Corresponding values of the used focus parameter Φ_y, of the local energy gradient $\hbar g$, and of the curvature parameter $\hbar f$ are given in Tab. 4.1. $\hbar f$ is the only component of the tensor describing the quadratic part of the systematic energy variation $Z(\mathbf{R}) = \hbar R_i f_{ij} R_j$ in case of uniaxial stress.

We aim to model the results referring to the HH exciton of the 15nm-wide SQW, setting the COM mass to $M = 0.36\ m_0$ (m_0=free electron mass) [57]. The systematic energy shift $Z(\mathbf{R})$ is supposed to be present only along the y direction, as in

Pos	Φ_y [mm]	$\hbar g$ [meV/mm]	$\hbar f$ [meV/mm^2]	$\hbar\sigma\sqrt{8\ln 2}$ [meV]
A	0.232	-2.06	1.37	0.162
B	0.296	-1.02	0.53	0.188
C	0.311	-0.32	0.09	0.188
D	0.298	0.01	0.34	0.186

Table 4.1: *Input parameters for the numerical simulations and for the analytical evaluations and fit parameters σ. The experimental FWHM of the Rayleigh spectrum of the unstrained sample is 0.186* meV.

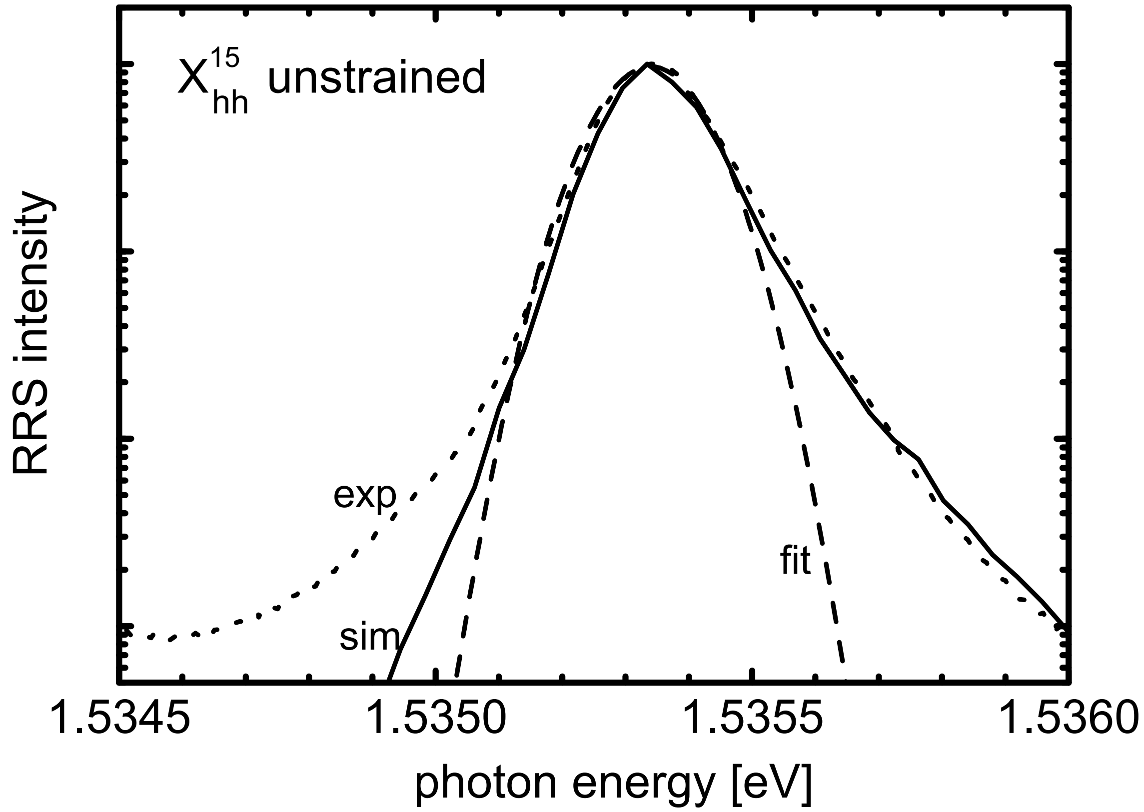

Figure 4.3: *Experimental (dots) and simulated (solid line) Rayleigh spectrum of the unstrained 15*nm *SQW in a semilogarithmic scale. A Gauss fit of the experimental data is also displayed (dashed line). The experimental data was obtained through spectral speckle analysis of a T=5*K *measurement.*

the experiment, Fig. 4.1. The short excitation pulse is modelled with a Gauss field amplitude, whose FWHM ~ 1 ps is chosen to reproduce the experimental width of the laser spectrum.

We discretize Eq. (4.1) with fixed boundary conditions on a box-shaped mesh of size $L_x \times L_y$ elongated along the strain direction y. We have verified that the results do not depend significantly on L_x and we have taken $(L_x, L_y) = (0.26\,\mu\mathrm{m}, 1.5\,\mathrm{mm})$. Correspondingly, the used excitation spot has an aspect-ratio of L_x/L_y. For treating such a large simulation area within of the present computational limitations, the grid points are taken on a quadratic lattice with spacing $\Delta_x = 10\,\mathrm{nm}$. We have checked that the final results (Rayleigh spectrum, speckle correlation function) do not differ significantly from the case we use $\Delta_x = 5\,\mathrm{nm}$. The $\Delta_x = 10\,\mathrm{nm}$ spacing approximately corresponds to the value of the exciton Bohr radius in this QW (see Tab. B.2), which sets the length scale for spatial correlations in the potential, as discussed in Sect. (3.1). A potential sampled on a grid with spacing of the order of its expected correlation length is mostly uncorrelated. Thus, we take the random part $W(\mathbf{R})$ to be an uncorrelated potential. Our approach is sufficient for a fair description of the experimental results of this Chapter, whose focus is the long-range (~mm) spatial correlation introduced by the systematic potential $Z(\mathbf{R})$.

The values of $W(\mathbf{R})$ are normal distributed with variance $\hbar\sigma_W$. In order to reproduce the width of the Rayleigh spectrum measured for the unstrained sample, (Fig. 4.3), we have taken $\hbar\sigma_W = 0.72$ meV. The Schrödinger equation Eq. (4.1) is solved by integration up to a time of about 100 ps, which is much larger than the typical speckle length. The resulting polarization $P(\mathbf{R}, t)$ and its Fourier transformations are used for computing the emitted intensity in time, real space, momentum, and frequency space.

Finally the speckle correlation function is calculated by averaging over a large number of speckles (about 10^3). In order to compare the experimental data to the results of our theoretical description, we eliminate the effect of incoherent emission (cp. Sect. (3.4)) by correcting the experimental intensity correlation. Only the denominator has to be corrected by the coherence degree c, since the numerator already correlates just the coherent parts, see Eq. (A.9). Thus, we replace $I(\mathbf{k}, t) \rightarrow c(t)I(\mathbf{k}, t)$ at the two involved times, obtaining

$$C^{\mathrm{exp}}(\Delta\mathbf{k}, t, \tau) = \frac{1}{c(t-\tau/2)c(t+\tau/2)} \left(\frac{\langle I_- \cdot I_+ \rangle_{\mathbf{k}}}{\langle I_- \rangle_{\mathbf{k}} \langle I_+ \rangle_{\mathbf{k}}} - 1 \right) , \tag{4.9}$$

where $I_\pm = I(\mathbf{k} \pm \Delta\mathbf{k}/2, t \pm \tau/2)$. Since no time averaging over t is done, the experimental correlation depends also on this variable.

We display in Fig. 4.4 the comparison of the experimental and simulated speckle correlation function for the positions A, B, C, and D. The tilting angle is clearly related to the local gradient of the transition energy and a quantitative agreement between experiment and simulation is found.[2]

The question whether this tilting of the speckle pattern implies a motion of the prepared wave packet can be answered by a real space simulation of the exciton

---

[2] We do not display here the Δk_x dependence of the speckle correlation, since the measured energy gradient (and therefore the speckle tilting) in the x-direction vanishes.

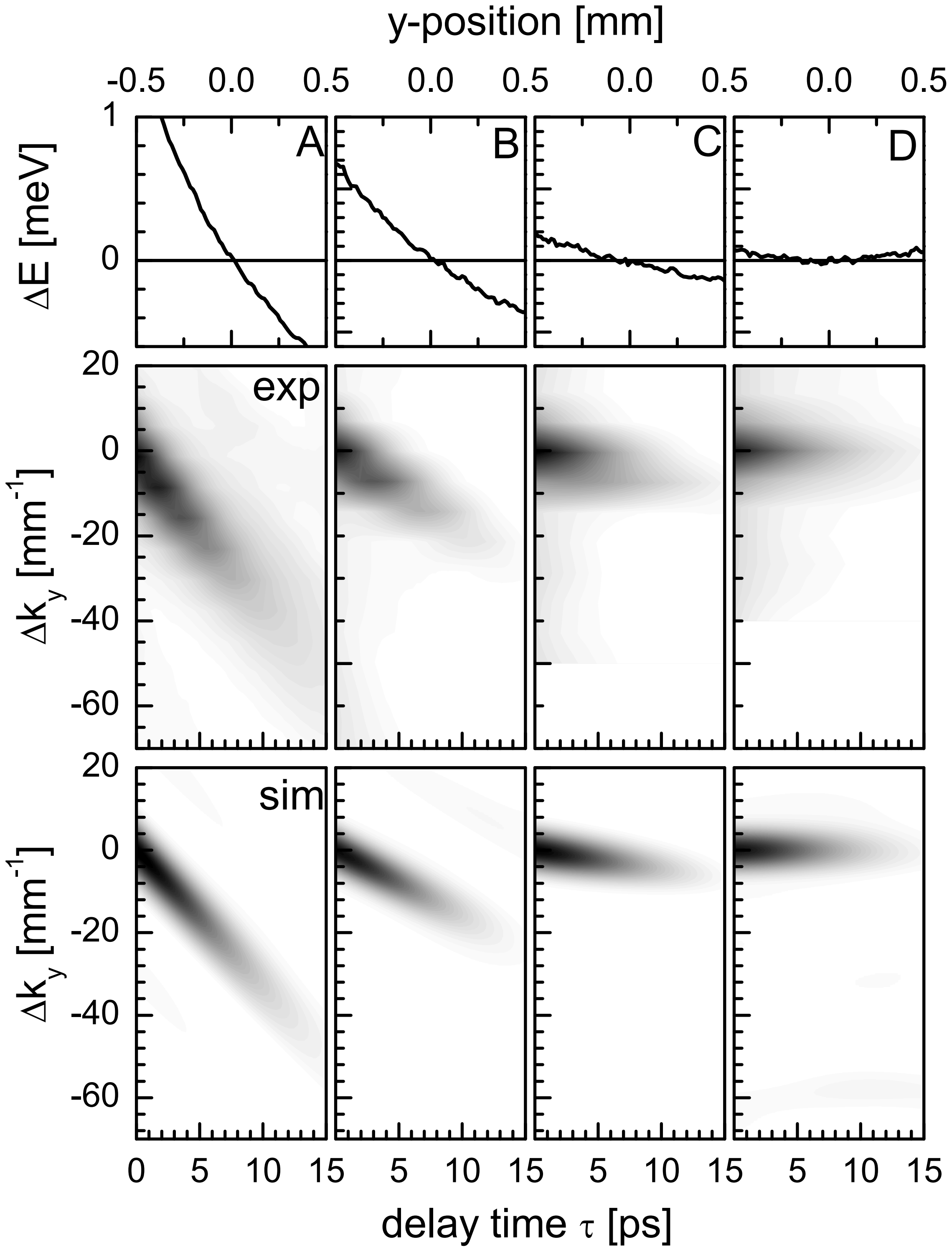

Figure 4.4: *First row: Experimental local transition energies with respect to the center of the excitation spots vs. position. Second and third row: Experimental* ($C^{\exp}(\Delta k_x = 0, \Delta k_y, t = 10\,ps, \tau)$) *and simulated* ($C(\Delta k_x = 0, \Delta k_y, \tau)$) *correlation functions; Linear gray-scale. Positions A, B, C, D of Fig. 4.1. The input parameters for the calculations are given in Tab. 4.1.*

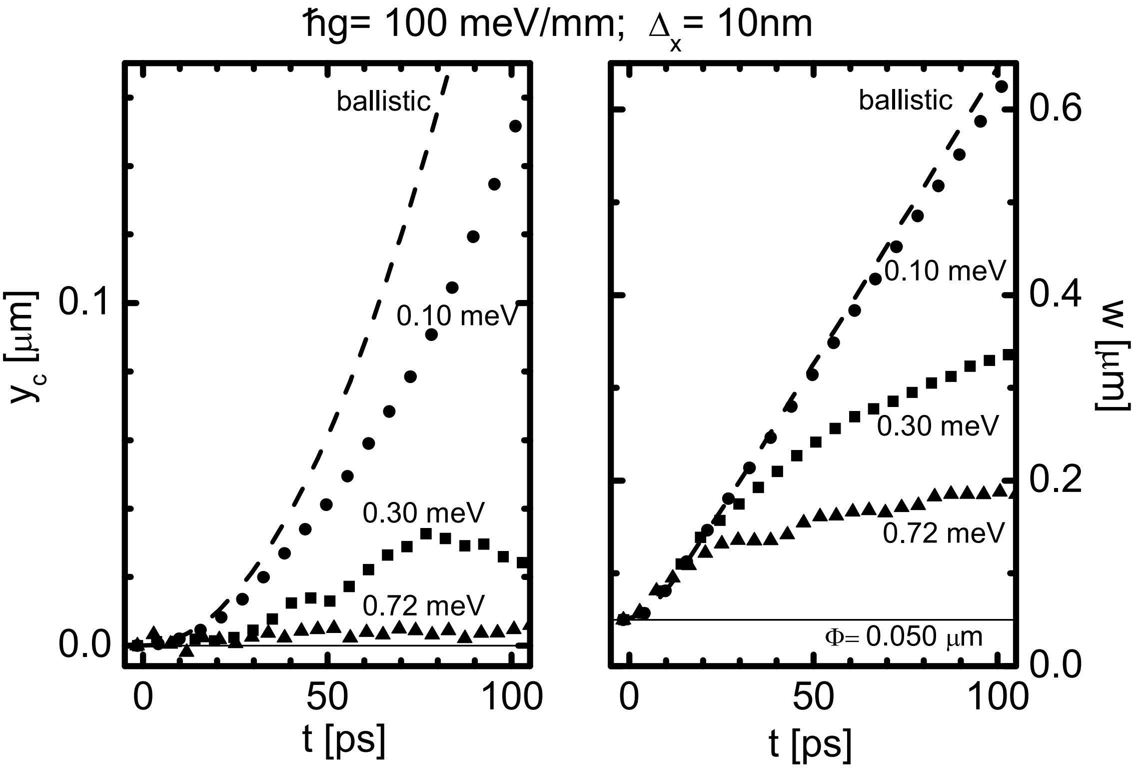

Figure 4.5: *Center position* $y_c(t)$ *and width* $w(t)$ *of a Gauss packet with variance* Φ *moving in a landscape with potential gradient* $\hbar g{=}10^2\,\mathrm{meV/mm}$ *and various strengths* $\hbar\sigma_W$ *of a white-noise disorder potential. The data points have been obtained by applying Eq. (4.10) on the the function* $P(0,y,t)$ *resulting from averaging over 50 disorder realizations. Step size* $\Delta_x = 10\,\mathrm{nm}$. *The ballistic case corresponds to the limit* $\hbar\sigma_W = 0\,\mathrm{meV}$ *and is given as dashed line.*

dynamics. We have used a simulation area of 400 μm^2 and a grid step $\Delta_x = 10$ nm. A Gauss packet is prepared at $t = 0$ and its time evolution in presence of an energy gradient $\hbar g$=10^2 meV/mm along the y direction is followed. We characterize the central position $y_c(t)$ and the width $w(t)$ of the wave packet by the moments

$$\begin{aligned} y_c(t) &= \int dy\, y\, |P(0,y,t)|^2 \Big/ \int dy\, |P(0,y,t)|^2 \\ w^2(t) &= 2\int dy\, y^2\, |P(0,y,t)|^2 \Big/ \int dy\, |P(0,y,t)|^2 \,. \end{aligned} \tag{4.10}$$

The width $w(t)$ is such that for a Gauss profile $P(\mathbf{R},t) = \exp(-\mathbf{R}^2/(2\Phi^2))\, P(t)$ it is $w(t) = \Phi$.

First it was checked that the free (i.e., in the absence of disorder) tight-binding dynamics is close enough to the ballistic motion for the used parameter range (see App. (C.3)). Then a white-noise disorder was added to the potential. The left panel in Fig. 4.5 shows the central position $y_c(t)$ for different disorder strengths. A weak disorder causes a smaller acceleration of the wavepacket with respect to the acceleration experienced in case of ballistic motion. For higher disorder strengths, a regime is entered where $y_c(t)$ does not increase monotonously any more. This is a sort of "localization transition": exciton motion occurs now only within the localization length (see below). For stronger disorder, the elongation from the preparation position is negligible: the packet stays localized, no motion in real space occurs. The disorder strength corresponding to this last situation is the same which was used for fitting the RRS spectrum in Fig. 4.3, but the module of the force $\hbar\mathbf{g}$ chosen here is about 50 times larger than the maximum obtained in the experiment. This allows us to conclude that no exciton acceleration was present in the investigated sample. Still speckle tilting can be explained also in terms of localized states in a landscape with systematic potential variation, as done in the next Section.

The right panel in Fig. 4.5 shows that the wavepacket broadening is almost ballistic for the case in which acceleration is possible, while a clearly sublinear diffusion process takes place for stronger disorder. The results about centre position and width dynamics can be summarized regarding the disorder potential as an effective "friction", though here dissipation is obviously absent.

For strong disorder (cases $\hbar\sigma_W = 0.30, 0.72$ meV in Fig. 4.5) the results can be interpreted expanding the polarization in a basis of localized states. In App. (C.4) it is shown that this leads to

$$\begin{aligned} y_c &\approx \langle y_\alpha \rangle = \sum_\alpha |c_{\alpha 0}|^2\, y_\alpha \Big/ \sum_\alpha |c_{\alpha 0}|^2 \\ w^2 &\approx \langle w_\alpha^2 \rangle = \sum_\alpha |c_{\alpha 0}|^2\, w_\alpha^2 \Big/ \sum_\alpha |c_{\alpha 0}|^2 \,, \end{aligned} \tag{4.11}$$

with

$$y_\alpha = \int dy\, y\, \psi_\alpha^2(0,y) \quad \text{and} \quad w_\alpha^2 = 2\int dy\, y^2\, \psi_\alpha^2(0,y)\,. \tag{4.12}$$

The average exciton position y_c vanishes for strong disorder since the systematic potential weakly breaks the inversion symmetry. Further, the width parameter w

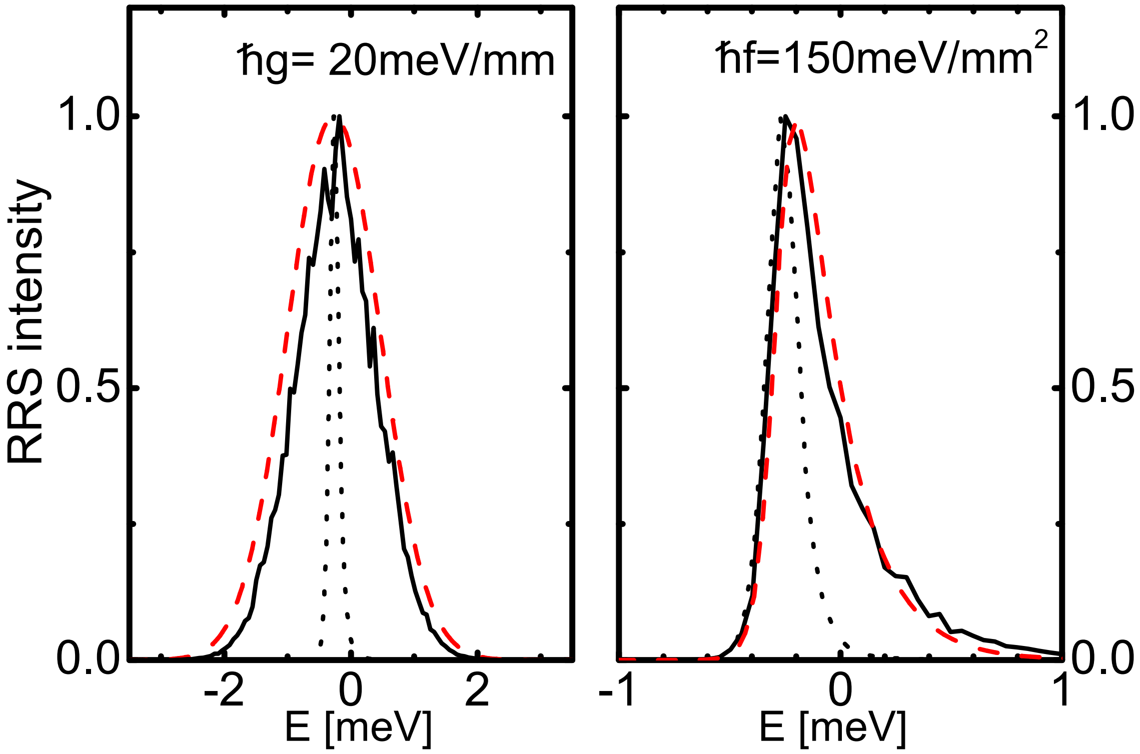

Figure 4.6: *RRS spectra in presence of linear (left panel) and quadratic systematic potential* $Z(\mathbf{R})$ *(right panel). Solid lines are the calculated spectra. The dotted lines are the spectra for the case* $Z(\mathbf{R}) = 0$*. The red dashed lines are their convolutions with the proper profile* $p(\omega)$*, given respectively by Eq. (4.26) and Eq. (4.27). Overall, disorder strength* $\hbar\sigma_W = 0.72\,\mathrm{meV}$ *and grid-step* $\Delta_x = 10\,\mathrm{nm}$ *were used.*

reaches an asymptotical value, which is an optically weighted average of the exciton localization lengths w_α.

4.5 Theory

Speckle tilting can originate from a systematic shifting of transition energies of localized excitons. This shift affects the phase factors of the emitted light, leading to a tilting in the speckle pattern without a real space motion.

The localized eigenstates $\psi_\alpha(\mathbf{R})$ and the corresponding eigenenergies $\epsilon_\alpha^{(0)}$ of the Hamiltonian H_0 appearing in Eq. (4.1) have been already introduced in Eq. (3.5). We further simplify the approach of Chapter 3 by taking a spatially uncorrelated potential $W(\mathbf{R})$, since only correlations on the (much larger) length-scale of $Z(\mathbf{R})$ are expected to be relevant for the present purpose. In case of delta pulse excitation, we have to solve the problem

$$\left(i\hbar\partial_t + H_0(\mathbf{R}) + Z(\mathbf{R})\right) P(\mathbf{R},t) = 0\,, \tag{4.13}$$

with the initial condition $P(\mathbf{R}, 0^+) = -i\mu_{\mathrm{cv}} E_{\mathrm{in}}(\mathbf{R})/\hbar$. We expand into eigenstates of H_0, thus we look for a solution of the type

$$P(\mathbf{R}, t) = \sum_\alpha c_\alpha(t) \psi_\alpha(\mathbf{R}) \,. \tag{4.14}$$

The dynamics of the expansion coefficients $c_\alpha(t)$ is given by

$$(i\hbar\partial_t + \epsilon_\alpha^{(0)} + Z_{\alpha\alpha}) c_\alpha(t) + \sum_{\beta\neq\alpha} Z_{\alpha\beta} c_\beta(t) = 0 \,, \tag{4.15}$$

with initial condition [3]

$$c_\alpha(t = 0^+) = -\frac{i}{\hbar}\mu_{\mathrm{cv}} \int d\mathbf{R}\, \psi_\alpha(\mathbf{R}) E_{\mathrm{in}}(\mathbf{R}) \approx -\frac{i}{\hbar}\mu_{\mathrm{cv}} E_{\mathrm{in}}(\mathbf{R}_\alpha) \int d\mathbf{R}\, \psi_\alpha(\mathbf{R}) \,, \tag{4.16}$$

and with matrix elements $Z_{\alpha\beta}$ defined as

$$Z_{\alpha\beta} = \int d\mathbf{R}\, \psi_\beta(\mathbf{R}) Z(\mathbf{R}) \psi_\alpha(\mathbf{R}) \,. \tag{4.17}$$

The off-diagonal elements in $Z_{\alpha\beta}$ are responsible for scattering between localized states, which could give rise to delocalization. Also the deformation potential matrix elements $t^{\mathbf{q}}_{\alpha\beta}$ (see App. (B.1)) are able to do this. However, as discussed in Sect. (4.2), in experiments carried out at a low enough temperature, phonon scattering should not be relevant for the SE.

Since $Z(\mathbf{R})$ has a macroscopic range (~ mm), it does not vary much over the typical exciton localization lengths (~ 10-100 nm). Thus the off-diagonal elements should get vanishing small for increasing inter-state distances $|\mathbf{R}_\alpha - \mathbf{R}_\beta|$ and we employ the adiabatic approximation

$$Z_{\alpha\beta} \approx Z(\mathbf{R}_\alpha)\, \delta_{\alpha\beta} \equiv Z_\alpha \,, \tag{4.18}$$

which allows to compute explicitly the coefficients $c_\alpha(t)$.

As usual, we switch to the momentum space with the Fourier definitions of Eq. (C.4), and find

$$P(\mathbf{k}, t) = -\frac{i\mu_{\mathrm{cv}}}{\hbar} \sum_\alpha e^{i(\mathbf{k}\cdot\mathbf{R}_\alpha + (\epsilon_\alpha^{(0)} + Z_\alpha)t/\hbar)} m_\alpha^2\, E_{\mathrm{in}}(\mathbf{R}_\alpha) \,. \tag{4.19}$$

We already notice that the effect of the systematic potential is a position dependent renormalization of the bare exciton energies, $\epsilon_\alpha^{(0)} \to \epsilon_\alpha^{(0)} + Z_\alpha$.

The frequency resolved polarization,

$$P(\mathbf{k}, \omega) = -\frac{2\pi i\mu_{\mathrm{cv}}}{\hbar} \sum_\alpha e^{i\mathbf{k}\cdot\mathbf{R}_\alpha} \delta(\hbar\omega - (\epsilon_\alpha^{(0)} + Z_\alpha))\, m_\alpha^2\, E_{\mathrm{in}}(\mathbf{R}_\alpha) \,, \tag{4.20}$$

allows to compute the RRS spectrum $J(\omega)$ from the speckle average of the SE intensity $|P(\mathbf{k}, \omega)|^2$. We obtain

$$J(\omega) = \sum_\alpha \delta(\hbar\omega - (\epsilon_\alpha^{(0)} + Z_\alpha))\, m_\alpha^4\, E_{\mathrm{in}}^2(\mathbf{R}_\alpha) \,. \tag{4.21}$$

---

[3] The condition that the excitation spot (~100 μm) is much larger than any exciton localization length (~100 nm) is always fulfilled in our experimental situation.

This can be recast in a way to make manifest its relation to the RRS spectrum $I^{\mathrm{coh}}(\omega)$ of an identical exciton system but without systematic potential $Z(\mathbf{R})$,

$$J(\omega) = \int d\omega_1 \, p(\omega_1) I^{\mathrm{coh}}(\omega - \omega_1) \,, \tag{4.22}$$

where the broadening function

$$p(\omega) = A \int d\mathbf{R} \, \delta(\hbar\omega - Z(\mathbf{R})) E_{\mathrm{in}}^2(\mathbf{R}) \tag{4.23}$$

enters and the RRS spectrum for $Z(\mathbf{R}) = 0$ is

$$I^{\mathrm{coh}}(\omega) = \frac{1}{A} \sum_{\alpha} m_\alpha^4 \delta(\hbar\omega - \epsilon_\alpha^{(0)}) \,, \tag{4.24}$$

with A normalization area in the QW plane. Analytical results are found using a Gaussian excitation spot,

$$E_{\mathrm{in}}(\mathbf{R}) = \exp\left(-\frac{\mathbf{R}^2}{2\Phi^2}\right) \,. \tag{4.25}$$

For a linear potential, a Gaussian broadening is obtained,

$$Z(\mathbf{R}) = \hbar\mathbf{g} \cdot \mathbf{R} \longrightarrow p(\omega) = c_{\mathrm{lin}} \exp\left(-\frac{(\hbar\omega)^2}{(\hbar g \Phi)^2}\right) \,, \tag{4.26}$$

while for a quadratic potential a Porter-Thomas function is found [4],

$$Z(\mathbf{R}) = \hbar f_{ij} \mathbf{R}^2 \longrightarrow p(s) = c_{\mathrm{quad}} \frac{\theta(\omega)}{\sqrt{\omega}} \exp\left(-\frac{\hbar\omega}{\hbar f_j \Phi^2}\right) \tag{4.27}$$

(c_{lin} and c_{quad} are constant prefactors). It is clear that the RRS broadening can be detected only if the variation of the potential $Z(\mathbf{R})$ across the spot size is comparable to the width of the RRS of a sample without systematic energy variation. This is the case in Fig. 4.6, where a focus variance $\Phi = 50\mu$m and systematic potentials with $\hbar g \Phi = 20$ meV/mm or $\hbar f \Phi^2 = 150$ meV/mm^2 were used in a simulation with disorder variance $\hbar\sigma_W = 0.72$ meV.

We return now to the study of the speckled SE. It is described by the intensity

$$I(\mathbf{k}, t) = \frac{\mu_{\mathrm{cv}}^2}{\hbar^2} \sum_{\alpha\beta} e^{i(\mathbf{k}\cdot(\mathbf{R}_\alpha - \mathbf{R}_\beta) + (\epsilon_\alpha^{(0)} - \epsilon_\beta^{(0)} + Z_\alpha - Z_\beta)t/\hbar)} m_\alpha^2 m_\beta^2 \, E_{\mathrm{in}}(\mathbf{R}_\alpha) E_{\mathrm{in}}(\mathbf{R}_\beta) \,. \tag{4.28}$$

Due to the renormalization in the phase factor, the SE exhibits speckles that are no more aligned along the time axis, see Fig. 4.7. The speckle averaged intensity selects only diagonal terms in the previous intensity and reads

$$\langle I \rangle_{\mathbf{k},t} = \frac{\mu_{\mathrm{cv}}^2}{\hbar^2} \sum_{\alpha} m_\alpha^4 E_{\mathrm{in}}^2(\mathbf{R}_\alpha) \,, \tag{4.29}$$

---

[4] for an uniaxial curvature tensor $f_{ij} = \delta_{ij} f_j > 0$.

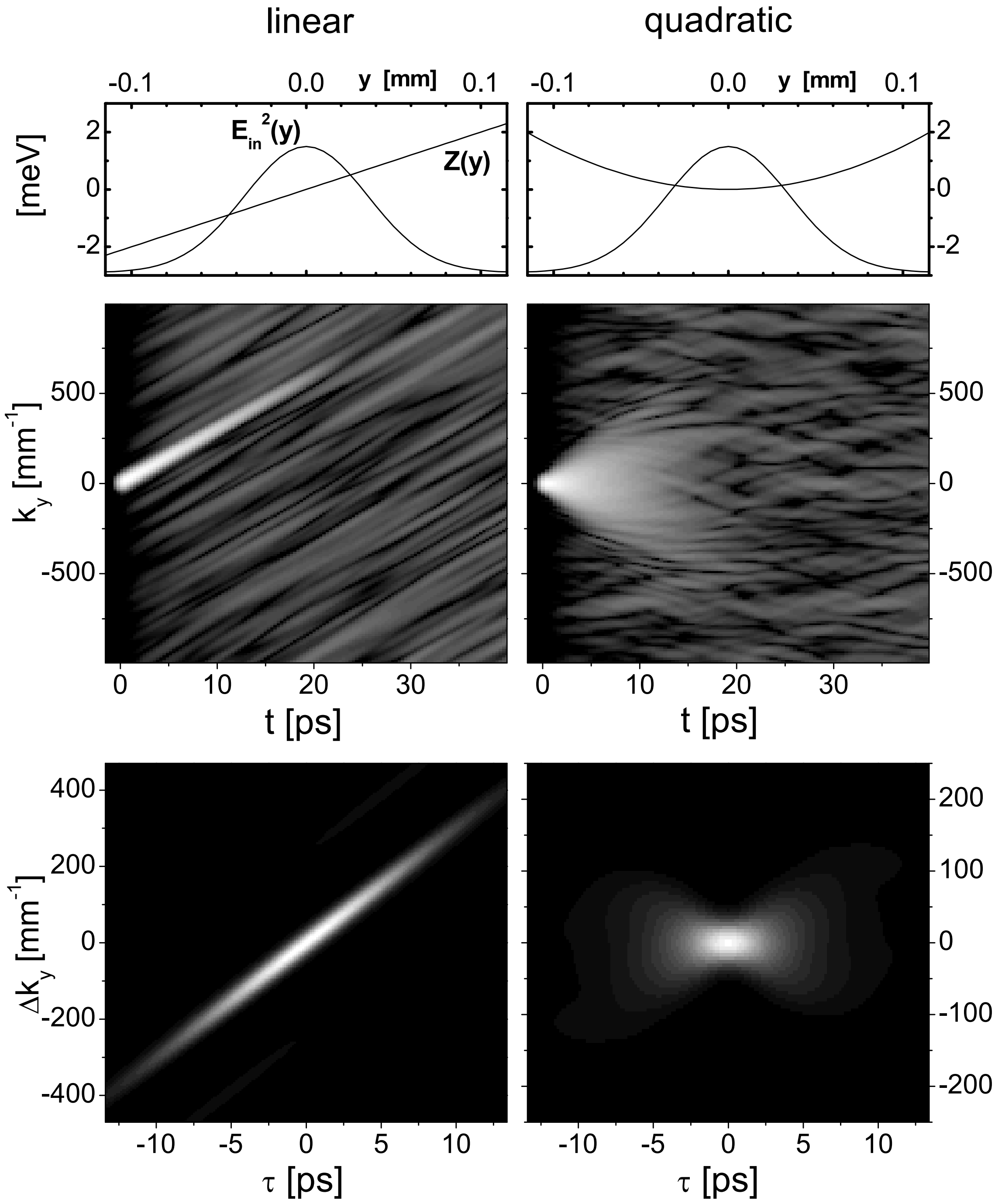

Figure 4.7: *Speckling in presence of a linear (left panels,* $\hbar g = 20$ meV/mm*) and of a quadratic systematic potential* $Z(y)$ *(right panels,* $\hbar f = 150\,\mathrm{meV/mm^2}$*). The first row shows the potentials* $Z(y)$ *in the region of the laser focus profile* $E_{\mathrm{in}}^2(y)$*. The second row contains the speckle patterns* $I(k_y, t)$ *in logarithmic gray scale over 5 orders of magnitude. In the third row, the corresponding speckle correlation functions* $C(\Delta k_y, \tau)$ *are plotted in linear gray-scale. Used disorder variance is* $\hbar\sigma_W = 0.72\,\mathrm{meV}$; *grid-step* $\Delta_x = 10\,\mathrm{nm}$.

where the brackets $\langle \cdots \rangle_{\mathbf{k},t}$ represent a directional and temporal average. This is used for computation of the speckle correlation function, which we define as

$$C(\Delta\mathbf{k}, \tau) = \left(\frac{\langle I_- \cdot I_+ \rangle_{\mathbf{k},t}}{\langle I_- \rangle_{\mathbf{k},t} \langle I_+ \rangle_{\mathbf{k},t}} - 1 \right) \tag{4.30}$$

with $I_\pm = I(\mathbf{k} \pm \Delta\mathbf{k}/2, t \pm \tau/2)$. This quantity contains information about the average speckle shape. If we introduce the auxiliary quantity

$$\varphi_0(\tau) = \left| \hbar \int d\omega \, e^{i\omega\tau} I^{\mathrm{coh}}(\omega) / \langle I \rangle_{\mathbf{k},t} \right|^2 , \tag{4.31}$$

then it can be shown (see App. (C.5)) that

$$\frac{C(\Delta\mathbf{k}, \tau)}{\varphi_0(\tau)} = \left| \int d\mathbf{R} \, e^{i(\Delta\mathbf{k}\cdot\mathbf{R} + Z(\mathbf{R})\tau/\hbar)} E_{\mathrm{in}}^2(\mathbf{R}) \right|^2 \tag{4.32}$$

holds.

In the case $Z(\mathbf{R}) = 0$ we retrieve the result that the speckle shape in momentum space is proportional to the Fourier transform of the excitation focus and that for Gauss RRS of variance $\hbar\sigma_R$ the correlation depends on delay τ only via the factor

$$\varphi_0(\tau) = \exp\left(-\sigma_R^2 \tau^2\right) . \tag{4.33}$$

For $Z(\mathbf{R}) \neq 0$ we have analytical results for both linear and quadratic potential, which are all what we need for an accurate description of the experimental situation. For a linear potential, we find that

$$C(\Delta\mathbf{k}, \tau) = C_0(\Delta\mathbf{k} + \mathbf{g}\tau, \tau) \tag{4.34}$$

(C_0 is the correlation function for the system with $Z(\mathbf{R}) = 0$). The effect of the potential is a tilting of the speckle pattern, exactly as it was found in the case that disorder is absent, Eq. (4.5): the tilting is proportional to the local gradient $\hbar\mathbf{g}$ of the systematic potential $Z(\mathbf{R})$. Very large potential gradients $\hbar\mathbf{g}$ have to be used in order to produce a break-down of the adiabatic approximation Eq. (4.18) and thus an exciton motion in real space in presence of disorder.

In case of quadratic curvature along two orthogonal axes in the plane of the QW and for Gaussian excitation spot, we have

$$\frac{C(\Delta\mathbf{k}, \tau)}{\varphi_0(\tau)} = \prod_{j=x,y} \frac{1}{S_j(\tau)} \exp\left[-\frac{1}{2} \left(\frac{\Phi_j \Delta k_j}{S_j(\tau)} \right)^2 \right] \tag{4.35}$$

with $S_j^2(\tau) = 1 + (f_j \Phi_j^2 \tau)^2$. The correlation broadens with time delay τ: this is because now speckles with different orientations appear in the SE, as shown in Fig. 4.7. Each orientation arises from the local gradient at a specific position in the quadratic potential $Z(\mathbf{R})$ [44].

Chapter 5

Non-Markovian Exciton-Phonon Dynamics

In the previous chapters the interaction between exciton and phonon has been treated within the so-called Markov approximation. This means that all the information on the scattering process between two exciton states α and β has been included into a scattering rate $\gamma_{\beta\leftarrow\alpha}$ which is found equivalent to the rate resulting from Fermi's golden rule (see Eq. (3.31)).

The physical idea for motivating this approach is that the exciton-phonon scattering is such a fast process that modifications of the dynamical variables during the collision time can be neglected. In other words, the assisted density matrixes $\hat{T}_{\alpha\mathbf{q}}, \tilde{T}_{\alpha\mathbf{q}}$ and $T_{\alpha\beta\mathbf{q}}$ can be adiabatically eliminated from the system Eq. (3.24), as a consequence of what we called step (i) of the Markov approximation, Eq. (3.27). The system has now no "memory" and different scattering events can be regarded as instantaneous and independent: this is the level of the Boltzmann kinetics. This approach was successfully implemented for the description of optical experiments and still represents the state of the art for exciton-phonon dynamics in QW.

The described approach can be questioned for instance if the time resolution of the experimental setup is shorter than the duration of a single scattering event. In the nineties, upconversion techniques with ultrafast laser pulses allowed to increase the time resolution of the detectors down to some tens of fs, opening the way to experimental investigation of non-Markovian or "quantum-kinetic" effects. At first, only interaction with longitudinal optical (LO) phonons was considered. Since they have a definite energy, memory effects were expected to be large and easier to detect than those related to longitudinal acoustic (LA) phonons, which have a dispersion.

Non-Markovian dynamics was predicted to affect the energy conservation rule in LO-mediated relaxation of an hot electron gas [53]. After nonresonant excitation, the conduction band electron distribution function is characterized by replicas of the initial distribution. These replicas are initially very broad and only after a finite time they resemble the spectral shape of the initial distribution: this effect was interpreted as a consequence of the energy-time uncertainty. It could be measured in a two-colour pump probe experiment in GaAs [16]. The differential transmission spectrum showed reshaping of the phonon cascade peaks after a LO phonon cycle (115 fs): this is the time the system needs for "remembering" its initial state. For explaining energy-time uncertainty in a closed (without external light coupling) system of electrons and phonons, Schilp *et al.* [54] showed that the energetic balance is still satisfied if the expectation value of the electron-phonon interaction Hamiltonian is taken into account.

However, all previous effects could be difficult to detect in practice, since they just lead to *quantitative* modifications of the distribution functions. It would be desirable to have a phenomenon that occurs only in a non-Markovian treatment, allowing for a clear proof of theoretical statements. This is thought to be present in the case of excitation by a short enough laser pulse: both a direct and a phonon-assisted optical transition are excited in this case. This leads to beating in the interband polarization, as measured by Four-wave-mixing (FWM), [7, 67]. An enhancement of this effect could be observed by Woggon *et al.* in both bulk and quantum dots (QD) of CdSe, which is a II-VI material and, as such, has got a larger polar (Fröhlich) coupling to optical phonons [70]. For the same reason, Hügel *et al.* [26] investigated non-Markovian effects in bulk CdTe, studying in particular the period of the oscillations. Since this electron-phonon quantum beats are a coherent effect, control of the beating feature by a second phase-locked pulse was also possible [58, 6].

The theoretical descriptions have been based so far either on the non-equilibrium Green's function approach [7] or on a density matrix formulation [71]. A review of quantum kinetic effects in photoexcited semiconductors can be found in Rossi *et al.* [49].

Non-Markovian dynamics affects the scenario of the so called pure dephasing, too. In the elastic (without population relaxation) interaction between exciton and phonon, phase relaxation is still possible. It is usually described by phenomenological damping rates, which leads to Lorentzian line shapes. However, in QD absorption profiles a more complicated scenario is observed. Typically, a narrow Lorentzian feature (zero phonon line, ZPL) is superimposed on top of a broader absorption band (broad band, BB) [8]. This band is due to a coupling between discrete electronic degrees of freedom (exciton) and the continuum of LA phonons states. Borri *et al.* [10] have intensively studied both spectral and time-resolved properties of an ensemble of InGaAs QD. Two distinct time-scales have been found in the time-integrated FWM signal: the shorter one of the order of 1ps and related to the broad band seen in absorption; the longer one strongly temperature dependent and extending up to some hundreds of ps. The initial dephasing has been successfully reproduced within the frame of the independent boson model (BM) [76]. As long as the exciton-phonon interaction is diagonal (in the space of the exciton states), an analytical solution for the exciton polarization is available and memory effects are accounted for exactly. This is indeed the case in small QD, where the exciton levels are much more distant than the energies of the LA phonons. The problem to explain the long-time decay or the finite linewidth of the ZPL without introducing a phenomenological decay was recently faced by Muljarov *et al.* [47]. The model was extended to include non-diagonal coupling. This introduces a quadratic term into the interaction term, but an exact result is still retrieved.

Pure dephasing has been found to be relevant in QW, too. As seen in Chapter 3, COM states are localized not only along growth direction, but, due to disorder, also in the plane of the well. Therefore, specially for thin QW, these states resemble QD

states. Photon echo experiments on thin QW have allowed to measure separately the total dephasing rate and the population relaxation rate [14]. The difference of both (pure dephasing) overcomes the half of the population relaxation rate for temperature higher than 25K. This pure dephasing is attributed to the coupling to LA phonons. In particular, deformation potential interaction should be dominant with respect to piezoelectric coupling in GaAs materials because of crystal symmetry [33]. All this motivates investigation of non-Markovian effects in QW, where they manifest both in population relaxation and pure dephasing. We stay within the frame of linear optics and we specially concentrate on the modifications of the linear absorption spectrum. This offers a chance to experimentally detect differences between Markovian and non-Markovian dynamics by simply varying the bath temperature.
The chapter is organized in five sections. After deducing the general theory in Sect. (5.1), the limiting cases of Markovian dynamics and single excitonic state are considered in Sect. (5.2) and Sect. (5.3) respectively. In Sect. (5.4) the results of the simulations with artificial and realistic QW exciton states are presented.

5.1 General theory

The starting point for this chapter is the system of equations of motion Eq. (3.24) for the exciton polarization and density matrix, which were given in 2B quality. There, they were solved within the Markov approximation for both the exciton-phonon and the exciton-photon interaction. In this Chapter, while we neglect the decay due to coupling to the light field ($r_\alpha = 0$) [1], we do not perform the Markov approximation for the exciton-phonon interaction. For numerical convenience, we transform these equations of motion into the frequency domain. Introducing selfenergy functions, this turns out to be a rather appropriate formalism. The numerical drawback of this transformation is that one has to properly deal with spiky features in the frequency domain such the zero phonon lines (ZPL). A convenient numerical technique for doing this is presented in App. (D.4).

5.1.1 Frequency-domain transformation

Integrating the system Eq. (3.24) in the time-domain presents the problem of solving a large number of coupled differential equations. Indeed the Hilbert space consists of discrete exciton states and of a continuum of phonon modes. Standard integration routines are not efficient for such a large system. Therefore, we transform Eq. (3.24) into frequency domain according to the Fourier definitions:

$$v(t) = \hbar \int d\Omega \, e^{+i\Omega t} v(\Omega) \, ; \quad v(\Omega) = \frac{1}{2\pi\hbar} \int dt \, e^{-i\Omega t} v(t) \tag{5.1}$$

Polarization
Using the definition Eq. (5.1) the first three equations in Eq. (3.24) are written in a

---

[1] That is, we have in mind a thin QW, where the decay due to phonon coupling is predominant (see Chapter3).

compact way as:

$$\sum_{\eta}\left((\hbar\Omega-\epsilon_{\alpha}^{(0)})\delta_{\alpha\eta}-\Sigma_{\alpha\eta}(\Omega)\right)P_{\eta}(\Omega)=S_{\alpha}(\Omega+\omega_{\text{in}}) \tag{5.2}$$

with the polarization selfenergy

$$\Sigma_{\alpha\eta}(\Omega)=\sum_{\beta\mathbf{q}}t_{\alpha\beta}^{\mathbf{q}}t_{\beta\eta}^{-\mathbf{q}}\left(\frac{n(\hbar\omega_{\mathbf{q}})+1}{\hbar(\Omega-\omega_{\mathbf{q}})-\epsilon_{\beta}-i0^{+}}+\frac{n(\hbar\omega_{\mathbf{q}})}{\hbar(\Omega+\omega_{\mathbf{q}})-\epsilon_{\beta}-i0^{+}}\right), \tag{5.3}$$

(we remind that the energies ϵ_{α} contain the deformation shifts: $\epsilon_{\alpha}=\epsilon_{\alpha}^{(0)}+\Delta_{\alpha}$). The phonon emission and absorption processes are readily identified by the numerators of this resolvent representation. The small imaginary parts $-i0^{+}$ are a reminder of the causality requirements. We specify from now on the proper complex frequency sheet by the shorthand notation $\Omega-i0^{+}\rightarrow\Omega$. Due to Eq. (5.2), the poles of $P_{\alpha}(\Omega)$ are given by the zeros of

$$\text{Det}\Big((\hbar\Omega-\epsilon_{\alpha}^{(0)})\delta_{\alpha\eta}-\text{Re}\Sigma_{\alpha\eta}(\Omega)\Big)=0 \tag{5.4}$$

These zeros are the renormalized energies $\epsilon_{\alpha}=\epsilon_{\alpha}^{(0)}+\Delta_{\alpha}$. Therefore Eq. (5.4) is the defining equation for the deformation shifts Δ_{α}. Since Eq. (5.4) has as many zeros as the number of exciton states N_S, we notice that *each* $P_{\alpha}(\Omega)$ has N_S poles.
The polarization allows to compute the absorption at normal incidence as

$$\alpha(\Omega)=\text{Im}\frac{1}{E_{in}(\Omega+\omega_{\text{in}})}\sum_{\eta}m_{\eta}P_{\eta}(\Omega)\,. \tag{5.5}$$

In the following, resonant excitation is always considered, $\omega_{\text{in}}=\omega_X$.

Density Matrix
The last two equations of Eq. (3.24) are transformed by the Fourier definition Eq. (5.1) into

$$\sum_{\eta,\theta}\Big((\hbar\Omega-\epsilon_{\alpha}^{(0)}+\epsilon_{\beta}^{(0)})\delta_{\alpha\eta}\delta_{\beta\theta}-\Xi_{\alpha\beta}^{\eta\theta}(\Omega)\Big)N_{\eta\theta}(\Omega)=Q_{\alpha\beta}(\Omega) \tag{5.6}$$

with the density matrix selfenergy $\Xi_{\alpha\beta}^{\eta\theta}(\Omega)=I_{\alpha\beta}^{\eta\theta}(\Omega)+O_{\alpha\beta}^{\eta\theta}(\Omega)$ which will be given below. The source term is [2]

$$Q_{\alpha\beta}(\Omega)=(S_{\alpha}\otimes P_{\beta}^{*})(\Omega)-(S_{\beta}^{*}\otimes P_{\alpha})(\Omega) \tag{5.8}$$

In the Markov approximation, it was found that the correlated density matrix

$$D_{\alpha\beta}(t)=(N_{\alpha\beta}-P_{\alpha}P_{\beta}^{*})(t) \tag{5.9}$$

---

[2] The convolution $\otimes$ is defined here by

$$(X\otimes Y^{*})(\Omega)=(Y^{*}\otimes X)(\Omega)=\hbar\int d\omega\,X(\omega)Y^{*}(\omega-\Omega)=\frac{1}{2\pi\hbar}\int dt\,e^{-i\Omega t}X(t)Y^{*}(t) \tag{5.7}$$

is diagonal ($\alpha = \beta$ only, see Sect. (3.3)). As a consequence, it could not contribute to the speckled (coherent) emission. In the non-Markovian dynamics, $D_{\alpha\beta}(\Omega)$ satisfies

$$\sum_{\eta,\theta} \Big((\hbar\Omega - \epsilon_\alpha^{(0)} + \epsilon_\beta^{(0)})\delta_{\alpha\eta}\delta_{\beta\theta} - \Xi_{\alpha\beta}^{\eta\theta}(\Omega) \Big) D_{\eta\theta}(\Omega) = \tilde{Q}_{\alpha\beta}(\Omega) \,. \tag{5.10}$$

Therefore the off-diagonal part in $D_{\alpha\beta}(\Omega)$ and, consequently, in $D_{\alpha\beta}(t)$ is in general not zero. Thus, at the non-Markovian level also the correlated density matrix contributes to the speckled emission and might modify the intensity statistics Eq. (2.4). We also notice that both in Eq. (5.6) and Eq. (5.10) the same Hamilton matrix appears. Just like in the Markov approximation, the sole difference between the equations of motion for $N_{\alpha\beta}(\Omega)$ and $D_{\alpha\beta}(\Omega)$ is their source term. In the case of the correlated density matrix, it reads

$$\tilde{Q}_{\alpha\beta}(\Omega) = A_{\alpha\beta}(\Omega) + B_{\alpha\beta}(\Omega) + C_{\alpha\beta}(\Omega) + \sum_{\eta,\theta} I_{\alpha\beta}^{\eta\theta}(\Omega)(P_\eta \otimes P_\theta^*) \,. \tag{5.11}$$

In writing Eq. (5.11) we have distinguished the matrixes $A_{\alpha\beta}, B_{\alpha\beta}, C_{\alpha\beta}$ that have the property to separately vanish both in the Markov and the single state limit. They read:

$$\begin{aligned}
A_{\alpha\beta}(\Omega) &= \hbar \sum_{\eta,\theta} \left\{ (\Omega P_\eta) \otimes P_\beta^* - (\Omega P_\theta)^* P_\alpha - \Omega(P_\eta \otimes P_\theta^*) \right\} \\
B_{\alpha\beta}(\Omega) &= \sum_{\eta,\theta} \left\{ -(\Sigma_{\alpha\eta} P_\eta) \otimes P_\beta^* + \delta_{\beta\theta}\Sigma_{\alpha\eta}(\Omega + \epsilon_\beta)(P_\eta \otimes P_\theta^*) \right\} \\
C_{\alpha\beta}(\Omega) &= \sum_{\eta,\theta} \left\{ (\Sigma_{\beta\theta} P_\theta)^* \otimes P_\alpha + \delta_{\alpha\eta}\Sigma_{\beta\theta}^*(-\Omega + \epsilon_\alpha)(P_\eta \otimes P_\theta^*) \right\} \,.
\end{aligned}$$

5.1.2 Integral representation

It is convenient to introduce the coupling matrix $f_{\alpha\delta}^{\beta\gamma}(E)$ such that

$$|E|^3 f_{\alpha\delta}^{\beta\gamma}(E) \equiv \sum_{\mathbf{q}} t_{\alpha\beta}^{\mathbf{q}} t_{\gamma\delta}^{-\mathbf{q}} \, \delta(|E| - \hbar\omega_{\mathbf{q}}) \,, \tag{5.12}$$

where a factor $|E|^3$ is extracted by the presence of the 3 dimensional $\mathbf{q}$-integration, the $\sqrt{E}$ prefactor in the deformation potential matrix elements $t_{\alpha\beta}^{\mathbf{q}}$, and the delta function. $f_{\alpha\delta}^{\beta\gamma}(E)$ is thus an even function of energy and the start value $f_{\alpha\delta}^{\beta\gamma}(E = 0)$ is finite. The coupling matrix can be interpreted [3]as a product of 2 one-phonon transition amplitudes among exciton states, $\alpha \leftarrow \beta$ and $\gamma \leftarrow \delta$. Exciton wavefunctions (in real space) are real, therefore the indexes can be permuted among pairs and within pairs, for instance:

$$(\alpha\beta)(\gamma\delta) \rightarrow (\beta\alpha)(\delta\gamma) \rightarrow (\delta\gamma)(\beta\alpha) \,, \tag{5.13}$$

---

[3] A full identification is prevented by the fact that $f_{\alpha\delta}^{\beta\gamma}(E)$ is not positive definite.

leading to a reduction of the computational task. Using the coupling matrix and extending to negative energies by using $n(-E) = -1 - n(E)$, the polarization self-energy Eq. (5.3) is written as [4]

$$\Sigma_{\alpha\eta}(\Omega) = \sum_{\beta} \int dE\, E^3 f^{\beta\beta}_{\alpha\eta}(E) \frac{n(E)}{\hbar\Omega + E - \epsilon_\beta}\,. \tag{5.14}$$

Real out-scattering processes, due to phonon absorption and emission, as well as virtual transitions are contained in this object and will be discussed later on. Reminding that Ω is complex, the real part of this selfenergy is non-locally related to the coupling matrix,

$$\mathrm{Re}\Sigma_{\alpha\eta}(\Omega) = \sum_{\beta} P \int dE\, E^3 f^{\beta\beta}_{\alpha\eta}(E) \frac{n(E)}{\hbar\Omega + E - \epsilon_\beta} \tag{5.15}$$

(P= principal value) while its imaginary part is simply given by

$$\mathrm{Im}\Sigma_{\alpha\eta}(\Omega) = \pi \sum_{\beta} (\epsilon_\beta - \hbar\Omega)^3 f^{\beta\beta}_{\alpha\eta}(\epsilon_\beta - \hbar\Omega)\, n(\epsilon_\beta - \hbar\Omega)\,. \tag{5.16}$$

The density selfenergy $\Xi^{\eta\theta}_{\alpha\beta}(\Omega)$, that is at the heart of the equation of motion for the density matrix, consists of two qualitatively different parts,

$$\Xi^{\eta\theta}_{\alpha\beta}(\Omega) = O^{\eta\theta}_{\alpha\beta}(\Omega) + I^{\eta\theta}_{\alpha\beta}(\Omega)\,. \tag{5.17}$$

The first part,

$$\begin{aligned} O^{\eta\theta}_{\alpha\beta}(\Omega) &= \delta_{\beta\theta} \sum_{\gamma} \int dE\, E^3 f^{\gamma\gamma}_{\alpha\eta}(E)\, \frac{n(E)}{\hbar\Omega + E + \epsilon_\beta - \epsilon_\gamma} \\ &+ \delta_{\alpha\eta} \sum_{\gamma} \int dE\, E^3 f^{\gamma\gamma}_{\beta\eta}(E)\, \frac{n(E)}{\hbar\Omega - E - \epsilon_\alpha + \epsilon_\gamma}\,, \end{aligned} \tag{5.18}$$

is of out-scattering nature, as it is clear taking its Markov limit (see Sect. (5.2)), and we observe that it is completely determined by the polarization selfenergy $\Sigma_{\alpha\eta}(\Omega)$ [5],

$$O^{\eta\theta}_{\alpha\beta}(\Omega) = \delta_{\beta\theta}\Sigma_{\alpha\eta}(\Omega + \epsilon_\beta) \;-\; \delta_{\alpha\eta}\Sigma^*_{\beta\theta}(-\Omega + \epsilon_\alpha)\,. \tag{5.19}$$

The in-scattering part depends on a coupling function with 4 different exciton labels:

$$\begin{aligned} I^{\eta\theta}_{\alpha\beta}(\Omega) &= -\int dE\, E^3 f^{\eta\theta}_{\alpha\beta}(E)\, n(E) \\ &\times \left(\frac{1}{\hbar\Omega - E - \epsilon_\eta + \epsilon_\beta} + \frac{1}{\hbar\Omega + E + \epsilon_\theta - \epsilon_\alpha} \right) \end{aligned} \tag{5.20}$$

and therefore cannot be expressed in terms of polarization selfenergies. Nevertheless, the dominant contributions in this matrix can be estimated observing the pole structure and the state distance dependence of the coupling matrix. Indeed $f^{\eta\theta}_{\alpha\beta}(E)$ depends on the overlap integrals between the states (α, η) and (β, θ) through the deformation potential matrix elements, (see Sect. (D.2)). Therefore $I^{\eta\theta}_{\alpha\beta}(\Omega)$ is dominated by the terms $I^{\alpha\beta}_{\alpha\beta}(\Omega)$.

---

[4] As a consequence of the properties of the coupling function, the polarization selfenergy is symmetric: $\Sigma_{\alpha\eta}(\Omega) = \Sigma_{\eta\alpha}(\Omega)$.

[5] $O^{\eta\theta}_{\alpha\beta}(\Omega) = O^{\alpha\beta}_{\eta\theta}(\Omega)$ inherited by the symmetry of $\Sigma_{\alpha\eta}(\Omega)$

	Σ	O	I
(i)	$\Sigma_{\alpha\alpha}(\Omega)$	$\mathrm{O}_{\alpha\beta}^{\alpha\beta}(\Omega)$	$\mathrm{I}_{\alpha\beta}^{\alpha\beta}(\Omega) + \mathrm{I}_{\alpha\alpha}^{\eta\eta}(\Omega)$
(i)+(ii)	$\mathrm{iIm}\Sigma_{\alpha\alpha}(\Omega)$	$\mathrm{iIm}\ \mathrm{O}_{\alpha\beta}^{\alpha\beta}(\Omega)$	$\mathrm{iIm}\ \mathrm{I}_{\alpha\beta}^{\alpha\beta}(\Omega) + \mathrm{i\ Im}\ \mathrm{I}_{\alpha\alpha}^{\eta\eta}(\Omega)$
(i)+(ii)+(iii)	$\mathrm{iIm}\Sigma_{\alpha\alpha}(\epsilon_\alpha)$	$\mathrm{iIm}\ \mathrm{O}_{\alpha\beta}^{\alpha\beta}((\epsilon_\alpha - \epsilon_\beta)/\hbar)$	$\mathrm{i\ Im}\ \mathrm{I}_{\alpha\alpha}^{\eta\eta}(0)$

Table 5.1: *Selfenergies after sequential application of the different steps of the Markov approximation.*

5.2 Markov limit

The polarization selfenergy is the Fourier transform of a memory kernel $\Sigma_{\alpha\eta}(t)$ which determines the dynamics of the time-dependent polarization. Taking the Fourier transform of Eq. (5.2), we have

$$(-i\hbar\partial_t - \epsilon_\alpha^{(0)})P_\alpha(t) = S_\alpha(t) + \sum_\eta \frac{1}{2\pi\hbar}\int dt'\Sigma_{\alpha\eta}(t-t')P_\eta(t') \tag{5.21}$$

Since in the Markov limit P_α decays with a rate $\hbar\gamma_\alpha$, the memory kernel reduces in this case to a delta-function:

$$\Sigma_{\alpha\eta}(t) \underset{\text{Markov}}{\longrightarrow} \frac{i}{2}\delta_{\alpha\eta}\hbar^2\gamma_\alpha\delta(t)\,. \tag{5.22}$$

The information on the history of the polarization and the cross correlation to all other polarization variables are lost.

We need now to specify rules for calculating the Markov limit from our formalism in the frequency domain. They are conditions that hold for the selfenergies and are the counterpart (in reverse order) of the three steps along which the Markov approximation in time domain was derived in Sect. (3.3). We require:

i) Conservation of the pole structure of polarization and density; the propagators

$$\frac{1}{\hbar\Omega - \epsilon_\alpha + \epsilon_\beta} \quad \text{and} \quad \Xi_{\alpha\beta}^{\eta\theta}(\Omega)\frac{1}{\hbar\Omega - \epsilon_\eta + \epsilon_\theta} \tag{5.23}$$

should have the same leading frequency behaviour. This introduces $\delta_{\alpha\eta}\delta_{\beta\theta}$ or $\delta_{\alpha\beta}\delta_{\eta\theta}$ factors;

ii) Null real parts of all selfenergies. According to Eq. (5.4), this means neglect of deformation shifts and (see Eq. (5.38)) unity weight for the ZPL;

iii) Neglect of the frequency dependencies: the selfenergies are evaluated at the poles of the propagators in in Eq. (5.23).

Tab. 5.1 shows the selfenergies after application of each of these steps [6] : That is, the Markov approximation reduces the selfenergies to

$$\begin{aligned}
\Sigma_{\alpha\eta}(\Omega) &\underset{\text{Markov}}{\longrightarrow} \frac{i}{2}\delta_{\alpha\eta}\,\hbar\gamma_\alpha \\
O_{\alpha\beta}^{\eta\theta}(\Omega) &\underset{\text{Markov}}{\longrightarrow} \frac{i}{2}\,\delta_{\alpha\eta}\delta_{\beta\theta}\,\hbar(\gamma_\alpha + \gamma_\beta) \\
I_{\alpha\beta}^{\eta\theta}(\Omega) &\underset{\text{Markov}}{\longrightarrow} -i\,\delta_{\alpha\beta}\delta_{\eta\theta}\,\hbar\gamma_{\alpha\leftarrow\eta}\,,
\end{aligned} \tag{5.24}$$

---

[6] Both $\mathrm{Im}O_{\alpha\alpha}^{\eta\eta}(\Omega)$ and $\mathrm{Im}I_{\alpha\beta}^{\alpha\beta}(\Omega = (\epsilon_\alpha - \epsilon_\beta)/\hbar)$ are zero because $E^3 f(E)$ is odd.

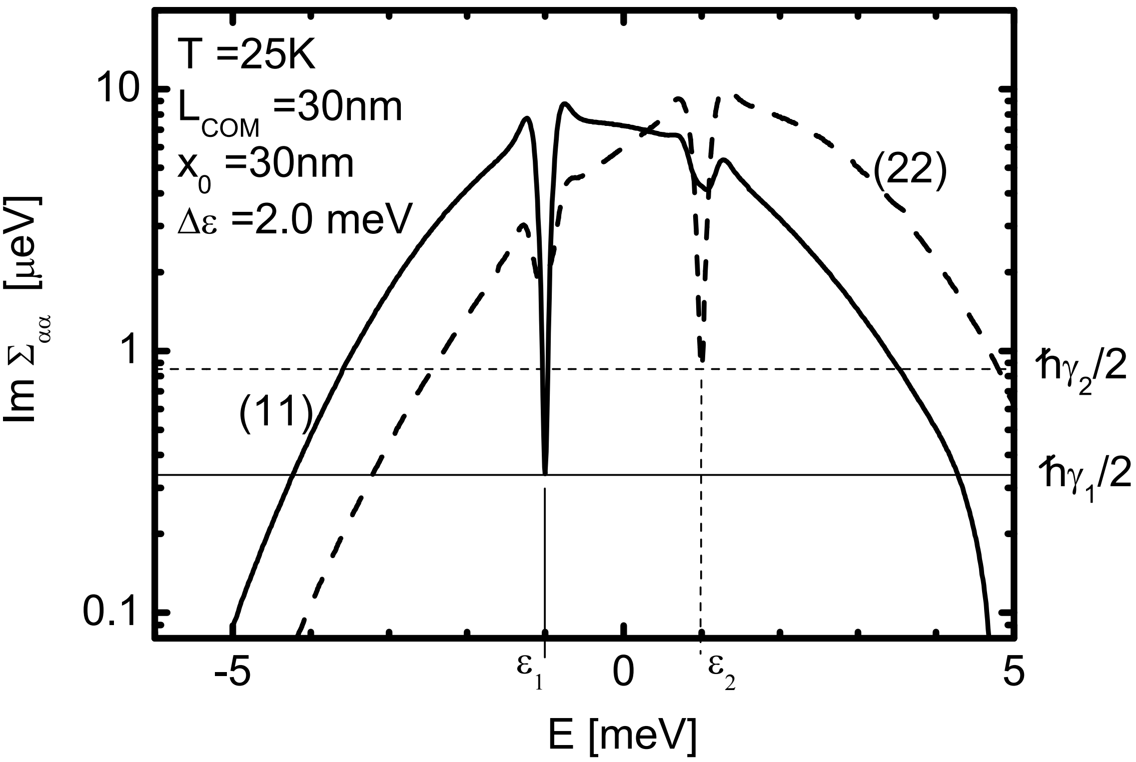

Figure 5.1: *Diagonal components of the imaginary part of the polarization selfenergy for 2 Gaussian model states (details of the states in Sect. (5.4)) whose bare energies are* $\epsilon_\alpha^{(0)} = -\epsilon_\beta^{(0)} = 1\,\mathrm{meV}$. *Im*$\Sigma_{11}(\Omega)$ *and* $\hbar\gamma_1/2$ *calculated according to Eq. (5.25) as solid lines; corresponding quantities for state 2 as dashed lines.*

where the scattering rates γ_α are given by [7]

$$\gamma_\alpha = \sum_{\beta\neq\alpha} \gamma_{\beta\leftarrow\alpha} = \frac{2\pi}{\hbar} \sum_{\beta\neq\alpha} (\epsilon_\beta - \epsilon_\alpha)^3 f^{\beta\beta}_{\alpha\alpha}(\epsilon_\beta - \epsilon_\alpha) n(\epsilon_\beta - \epsilon_\alpha)\,. \tag{5.25}$$

The relation between the imaginary part of the polarization selfenergy and the Markovian phonon rates in highlighted in Fig. 5.1, where the result of a numerical simulation with 2 model states is plotted.
With these prescriptions, we retrieve the Markov result for the polarization, which was already obtained in the time domain (setting $r_\alpha = 0$ in the first line in Eq. (3.34)):

$$P_\alpha(\Omega) = \frac{S_\alpha(\Omega)}{\hbar\Omega - \epsilon_\alpha^{(0)} - \frac{i}{2}\hbar\gamma_\alpha}\,. \tag{5.26}$$

The source term for the correlated density matrix is in the Markov limit a diagonal matrix,

$$\tilde{Q}_{\alpha\beta}(\Omega) = -i\delta_{\alpha\beta} \sum_\eta \hbar\gamma_{\alpha\leftarrow\eta} (P_\eta \otimes P^*_\eta)(\Omega) \approx -2\pi\delta_{\alpha\beta} \sum_\eta \hbar\gamma_{\alpha\leftarrow\eta} \frac{|S_\eta(\Omega)|^2}{\Omega - i\gamma_\eta}\,, \tag{5.27}$$

---

[7] These rates are identical to those of Eq. (3.31), as it is clear inserting here the definition of coupling matrix, Eq. (5.12).

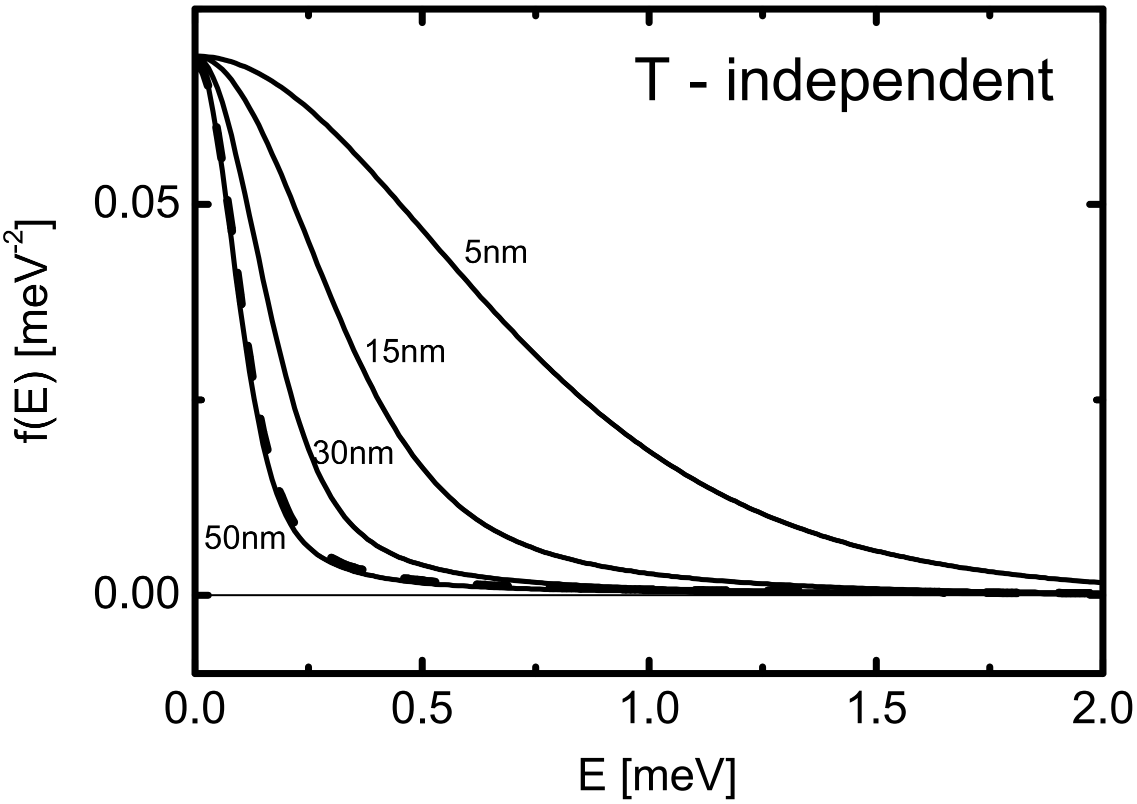

Figure 5.2: *Coupling function $f(E)$ for Gaussian states of different variance L_{COM}. The dashed line is the broad band part of ImP(E) (normalized to the peak value of the coupling functions) for the case $L_{COM} = 50\,\mathrm{nm}$ and $T = 25\,\mathrm{K}$.*

(short pulse approximation was done). Therefore, also the correlated density matrix is diagonal, as already stressed in Sect. (3.3). The correlated density matrix satisfies

$$\sum_{\eta} \left(\hbar(\Omega - i\gamma_\alpha)\delta_{\alpha\eta} + i\hbar\gamma_{\alpha\leftarrow\eta}\right) D_{\eta\eta}(\Omega) = \tilde{Q}_{\alpha\alpha}(\Omega)\,, \tag{5.28}$$

which is the Fourier transform of Eq. (3.36).

5.3 Single state limit

Though it could seem not very realistic to deal with a single exciton state, there are two good reasons for better understanding this situation:
i) it corresponds to the physical limit of (spatially or spectrally) distant states;
ii) it is a test for the theory and the numerics, since semi-analytic solutions are available in this case.
In this section we present both the 2nd Born and the exact (Independent Boson Model) results. Simple relations holding for the density matrix are also retrieved in the single state case.

2nd Born
If there is just one exciton state, the linear system of Eq. (5.2) has the explicit

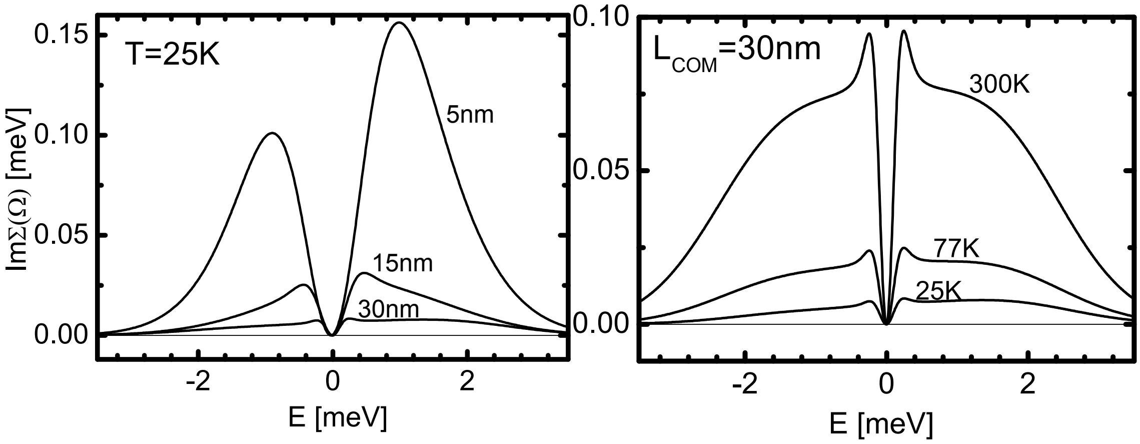

Figure 5.3: *Imaginary part of the frequency resolved selfenergy for a Gauss state with* $\epsilon_\alpha^{(0)} = 0\,\mathrm{meV}$. *Left panel: at* $T = 25\,\mathrm{K}$ *for different state sizes* L_{COM}*; Right panel: for* $L_{COM} = 30\,\mathrm{nm}$ *at different temperatures* T.

solution

$$P_1(\Omega) = \frac{S_1(\Omega)}{\hbar\Omega - \epsilon_1^0 - \Sigma(\Omega)}\,, \tag{5.29}$$

with the selfenergy

$$\Sigma(\Omega) = \int dE\, E^3 f(E) \frac{n(E)}{\hbar\Omega + E - \epsilon_1}\,. \tag{5.30}$$

The matrix $f_{\alpha\eta}^{\gamma\gamma}(E)$ has been replaced by the function $f(E)$ such that

$$|E|^3 f(E) \equiv \sum_{\mathbf{q}} |t_{11}^{\mathbf{q}}|^2\, \delta(|E| - \hbar\omega_{\mathbf{q}})\,. \tag{5.31}$$

It is displayed for different state size in Fig. 5.2. Smaller states couple more effectively to the phonon degrees of freedom since these states are more extended in momentum space. For Gaussian states of variance L_{COM}, the width of the coupling function is approximately set by $\hbar s/L_{COM}$, as discussed in App. (D.1). Thus, all non-Markovian effects (deformation shifts, ZPL weight reduction) are enhanced for smaller COM exciton states.

The real part of the selfenergy,

$$\mathrm{Re}\Sigma(\Omega) = P\int dE\, E^3 f(E) \frac{n(E)}{\hbar\Omega + E - \epsilon_1}\,, \tag{5.32}$$

allows to compute the single state deformation shift Δ_1 as (see Eq. (5.4)) [8]

$$\Delta_1 = \mathrm{Re}\Sigma(\epsilon_1/\hbar) = -\frac{1}{2}\int dE E^2 f(E) < 0\,. \tag{5.33}$$

Δ_1 is temperature independent and its dependence on the state size is displayed in Fig. 5.5. The imaginary part of the selfenergy is always non negative

$$0 \le \mathrm{Im}\Sigma(\Omega) = \pi(\epsilon_1 - \hbar\Omega)^3 f(\epsilon_1 - \hbar\Omega)\, n(\epsilon_1 - \hbar\Omega) \tag{5.34}$$

---

[8] Here and in the following, we exploit the decomposition of the Bose function into its even and odd part: $n(E) = -\frac{1}{2} + \frac{1}{2}\mathrm{cth}\,(E/(2k_BT))$.

and vanishes at the resonance, Fig. 5.3. $\mathrm{Im}\Sigma(\Omega)$ presents two bands corresponding to (virtual) phonon absorption and emission processes. Their asymmetry grows for smaller states and lower temperatures. The absorption spectrum is

$$\alpha(\Omega) = \frac{m_1}{E_{\mathrm{in}}(\Omega+\omega_{\mathrm{in}})} \frac{\mathrm{Im}\Sigma(\Omega)}{(\hbar\Omega - \epsilon_1^0 - \mathrm{Re}\Sigma(\Omega))^2 + (\mathrm{Im}\Sigma(\Omega))^2} \,. \tag{5.35}$$

In a range of temperature for which the selfenergy has small values ($\sim 10\,\mu$eV) with respect to the range of the coupling function ($\sim 1\,$meV) and the Bose function can be approximated as $k_B T/\hbar\Omega$, the absorption is simply related to the coupling function[9],

$$\alpha(\Omega) \sim f(\epsilon_1 - \hbar\Omega)\,. \tag{5.36}$$

In Fig. 5.2 it is seen that good agreement is reached for the case $(T, L_{COM}) = (25\,\mathrm{K}, 50\,\mathrm{nm})$.

The absorption spectrum and the time dynamics of the polarization amplitude are displayed for other exciton sizes and phonon temperatures in Fig. 5.4. The absorption consists of a delta-function at the resonance position $\Omega = \epsilon_1/\hbar$ which is called zero phonon line (ZPL), and of a broad band (BB) due to virtual transitions that involve LA phonons, see Fig. 5.4. The ZPL has zero width since in presence of a single state no transition to other states is possible. As a consequence, the time-resolved polarization [10] after impulsive excitation decreases from the initial value to a constant, whose value is set by the relative weight of the ZPL in the absorption spectrum, $ZPL = |P(t=\infty)/P(t=0)|$. The undershot feature seen in the 2B polarization for higher temperatures (bottom-right panel in Fig. 5.4) is related to the development of a plateau in the absorption spectrum (top-right panel in Fig. 5.4). This effect is an intrinsic inconvenience of the 2B approximation that therefore is no more reliable for too high temperatures.

Observing that for not too low temperature $\mathrm{Im}\Sigma(\Omega)$ starts quadratically at ϵ_1, the polarization in the vicinity of the resonance can be evaluated as [11]

$$P_1^{ZPL}(\Omega) = P_1(\Omega \approx \epsilon_1/\hbar) = \frac{S_1(\epsilon_1)}{(\hbar\Omega - \epsilon_1)(1+R')}\,, \tag{5.37}$$

having introduced the negative derivative R' as

$$R' = -\frac{d}{\hbar\, d\Omega}\mathrm{Re}\Sigma|_{\epsilon_1} = \int dE E f(E) n(E) > 0\,. \tag{5.38}$$

This allows to express the ZPL simply as

$$ZPL|_{2B} = \frac{1}{(1+R')}. \tag{5.39}$$

The quantity R' is thus a measure of the importance of non-Markovian effects. In the contest of the independent boson model (see below), it is called Huang-Rhys factor.

---

[9] Use Eq. (5.34) in Eq. (5.35), neglecting $\Sigma(\Omega)$ in the denominator.

[10] In the time frame we display always the amplitude $|P(t)|$, which is related to the results of FWM experiments, such as [10].

[11] A Taylor expansion for $\Sigma(\Omega)$ around $\Omega = \epsilon_1/\hbar$ is applied.

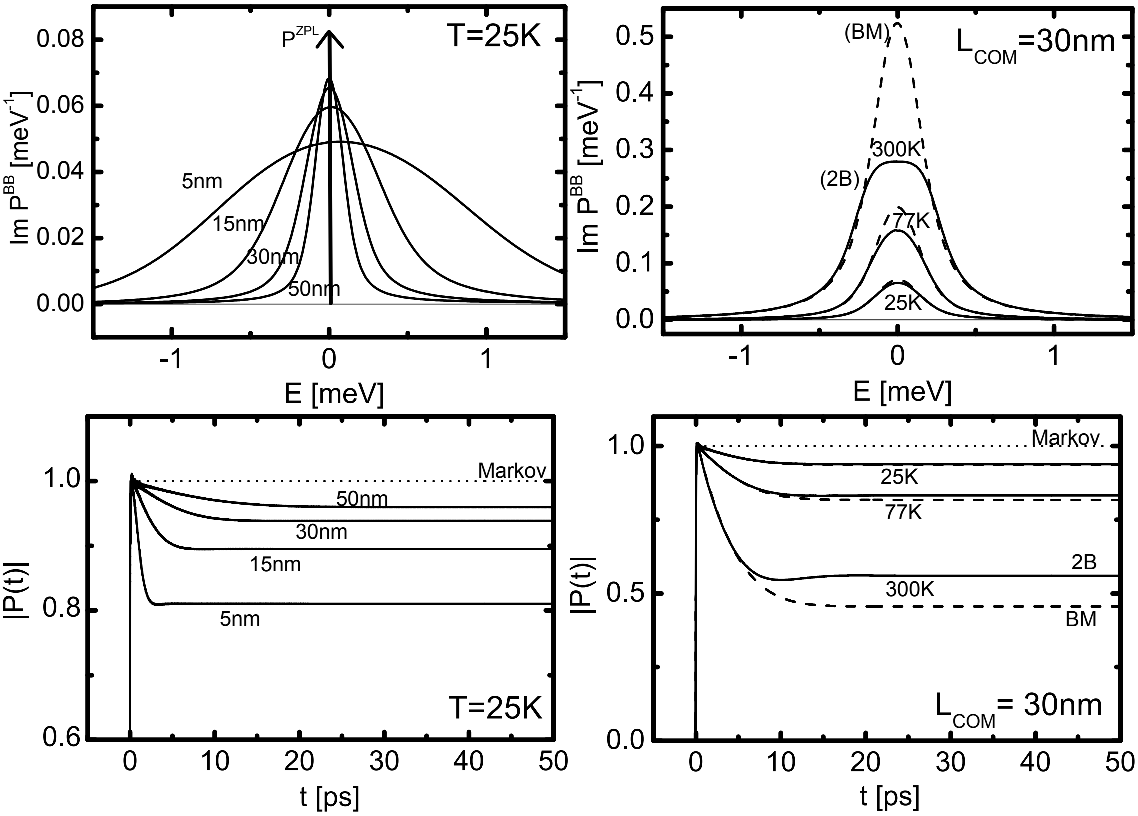

Figure 5.4: *BB part of the absorption spectrum (top row, the ZPL part is depicted as an arrow in the first panel) and corresponding dynamics of the polarization amplitude (bottom row). Left panels: at* $T = 25\,\mathrm{K}$ *for Gauss states of different variance* L_{COM} *and* $\epsilon_\alpha^{(0)} = 0\,\mathrm{meV}$. *Right panels: for* $L_{COM} = 30\,\mathrm{nm}$ *at different temperatures* T. *The 2B results (solid) are compared to the BM results (dashed). The Markov dynamics of the polarization amplitude is given as dotted lines.*

Markov limit

In the Markov limit the single-state polarization selfenergy is zero [12] : we have only one state and we do not allow for the virtual transitions mediated by the phonon bath. Thus the imaginary part of the polarization reduces to a ZPL,

$$\mathrm{Im}P_1(\Omega) = \mathrm{Im}\left(\frac{S_1(\Omega)}{\hbar\Omega - \epsilon_1^0}\right) = \pi S_1(\Omega)\,\delta(\hbar\Omega - \epsilon_1^0) \tag{5.41}$$

and the amplitude of the polarization stays constant after delta-like excitation, since

$$P_1(t) = \frac{i}{\hbar}\theta(t)\,m_1 \exp(i\epsilon_1^0 t/\hbar)\,. \tag{5.42}$$

The Markov ZPL weight is therefore always equal to unity.

---

[12] Just evaluate

$$\Sigma(\Omega) \underset{\mathrm{Markov}}{\longrightarrow} \mathrm{Im}\int dE\, E^2 f(E)\, n(E) = 0 \tag{5.40}$$

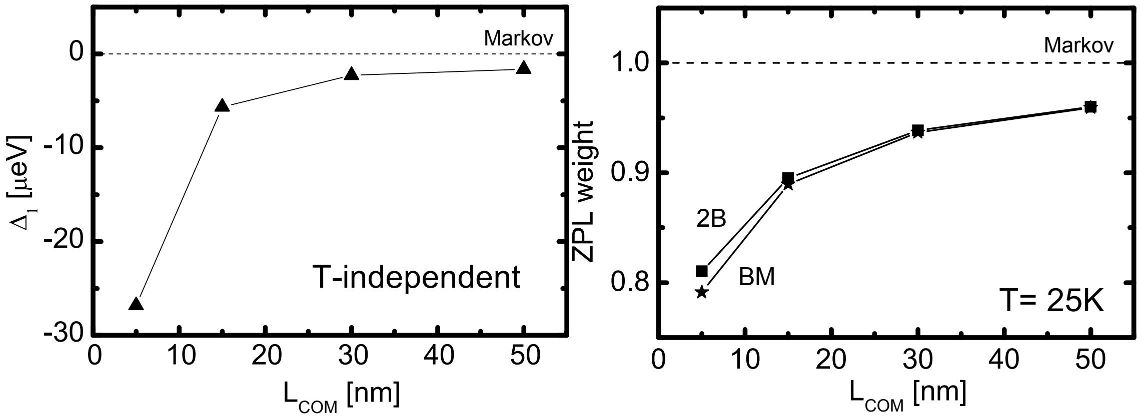

Figure 5.5: *Left panel: deformation shifts for different state sizes. Right panel: ZPL weight at* $T = 25\,\mathrm{K}$ *according to 2B (squares) and BM (stars) for different state sizes.*

Independent Boson Model

An exact solution for the exciton polarization is possible for the case that the interaction with the bosonic degrees of freedom is described by a diagonal coupling to the system of interest: i.e. if the interaction gives place only to virtual transitions. The exciton-phonon interaction term in Eq. (3.18) is in this case

$$H_{\text{int}} = \sum_{\alpha\mathbf{q}} t^{\mathbf{q}}_{\alpha\alpha}(a^\dagger_{\mathbf{q}} + a_{-\mathbf{q}})B^\dagger_\alpha B_\alpha \tag{5.43}$$

This model applies to the situation discussed in this section, since only one state interacts with the phonon bath. Without the term for the coupling to the light field, the model is known as Independent Boson Model [42]. Its result for the polarization reads [13]

$$P_1(t) = \frac{i}{\hbar} m_1 \theta(t) \exp(i\epsilon_1 t/\hbar - R' + Y(t)) \tag{5.44}$$

with the auxiliary function

$$Y(t) = \int dE E f(E) \Big[(n(E) + \frac{1}{2}) \cos(\frac{Et}{\hbar}) + \frac{i}{2} \sin(\frac{Et}{\hbar}) \Big] \tag{5.45}$$

whose start value $Y(0) = R'$ is called Huang-Rhys factor. Since $Y(t)$ vanishes for large time t after excitation, the ZPL weight within BM is

$$ZPL|_{BM} = \exp(-R')\,. \tag{5.46}$$

It agrees up to the first order in R' with the 2B results Eq. (5.39) to which it is compared in Fig. 5.5. The time-dependent oscillation frequency $\omega(t)$ is given by

$$\hbar\omega(t) = \epsilon_1 + \hbar\frac{d}{dt}\text{Im}Y(t) = \epsilon_1 + \frac{1}{2}\int dE E^2 f(E) \cos(\frac{Et}{\hbar})\,. \tag{5.47}$$

---

[13] For comparing with the 2B formulas, we take here a δ-pulse of area m_1. For the numerical results, the quantity $P = m_1 P_1 / m_1^2$ is displayed, that has the start-value $P(t=0) = i$.

It starts with $\hbar\omega(0) = \epsilon_1 - \Delta_1 = \epsilon_1^0$ and ends with $\hbar\omega(\infty) = \epsilon_1$. This renormalization of the oscillation frequency with the deformation shift is sometimes called "phonon dressing" of the exciton resonance.

Density Matrix
Since there is only one state, both in 2B, Markov limit, and BM the total population is conserved,

$$N_{11}(t) = \theta(t) m_1^2 . \tag{5.48}$$

Therefore the incoherent density is simply

$$D_{11}(t) = \theta(t)(m_1^2 - |P_1(t)|^2) . \tag{5.49}$$

In particular, within the BM we have the exact result

$$D_{11}(t) = \theta(t) m_1^2 (1 - e^{-2R' + 2\mathrm{Re}Y(t)}) . \tag{5.50}$$

5.4 Numerical results with more states

Here we present the results for application of the non-Markovian theory to systems containing more than one exciton state.
First artificial states are used, in order to understand the role of state shape, state energy and phonon temperature. The limit of single state dynamics is reached for large energetic or spatial separation. In the second part of this section, QW exciton states resulting from realistic simulations are used as inputs. A much richer combination of spatial overlaps is responsible for different behaviour in the low and in the high energy part of the absorption spectrum.
For both artificial and simulation states we consider QW of thin width $L_z = 5\,\mathrm{nm}$, since in this case (due to strong localization) the radiative rates are small (see App. (B.3)) and it is justified to neglect them. Furthermore, on the basis of the single state results, the importance of the BB is expected to be large for strongly localized states, Fig. 5.4. For all simulations, a finite pulse excitation was used, whose field has a Gaussian envelope $E_{\mathrm{in}}(t)$ with variance $\tau_P = 21$ fs.

5.4.1 Artificial states

We consider two mutually orthogonal model states,

$$\begin{aligned} \psi_1(x,y) &= A_1 \exp\left(-\frac{x^2+y^2}{2L_{COM}^2}\right) \\ \psi_2(x,y) &= A_2 \left(\frac{x - x_0/2}{L_{COM}}\right) \exp\left(-\frac{(x-x_0)^2+y^2}{2L_{COM}^2}\right) , \end{aligned} \tag{5.51}$$

where the constants A_1 and A_2 ensure normalization. The parameter x_0 sets not only the inter-state distance, but modifies also the oscillator strength m_2^2 of the state

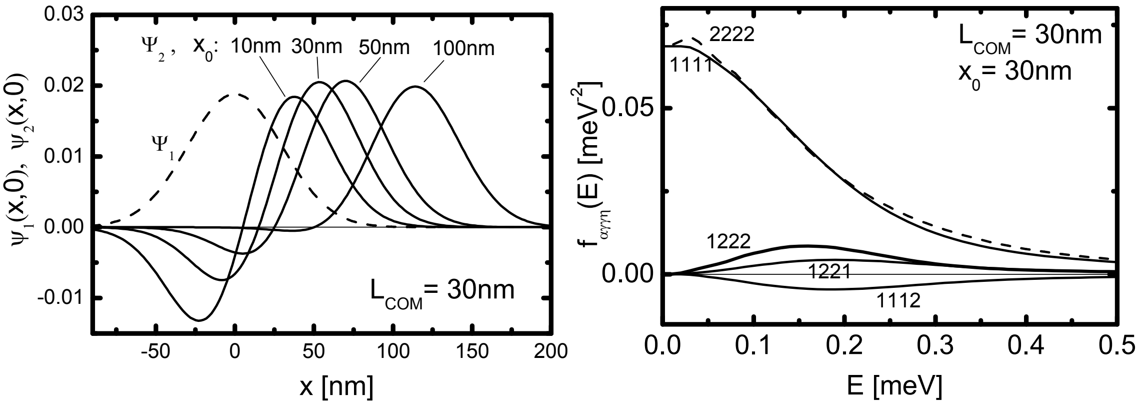

Figure 5.6: *Left panel: sections of the artificial states for varying spacing x_0 and other parameters as given. Right panel: coupling function $f^{\gamma\gamma}_{\alpha\eta}(E)$ for two states with the given parameters. The indexes are sorted as $\alpha\gamma\gamma\eta$.*

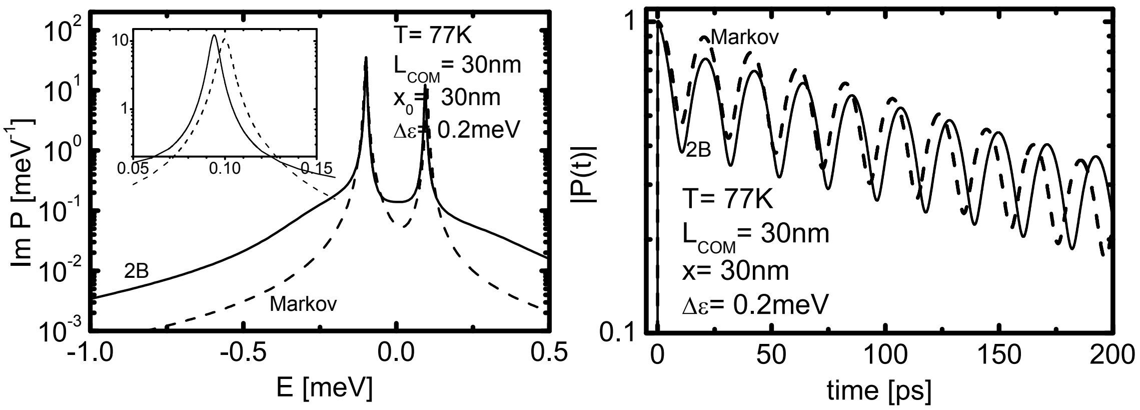

Figure 5.7: *Left panel: Absorption spectrum at* $T = 77\,\mathrm{K}$ *for two artificial states of the type of Eq. (5.51) with parameters as given. Markov: dashed; non-Markov (2B): solid. In the inset, the second state peak is blown up. Right panel: amplitude of the time resolved polarization for the same states; notice logarithmic scale.*

ψ_2. The eigenenergies can be adjusted independently of the spatial parameters and are taken to be $\epsilon_1 = -\Delta\epsilon/2$ and $\epsilon_2 = \Delta\epsilon/2$.

These wavefunctions are the first two eigenstates of a two-dimensional harmonic oscillator if $x_0 = 0$. For $x_0 \gg L_{\mathrm{COM}}$ they are two shifted Gaussians. The significant section of the used artificial states is given in Fig. 5.6. It is clear that for small separation x_0 the state ψ_2 has a very small oscillator strength m_2^2, while for $x_0 = 100\,\mathrm{nm}$ (and $L_{COM} = 30\,\mathrm{nm}$) it is almost Gaussian and has oscillator strength $m_2^2 \approx m_1^2$. These model states can be regarded as states of a QD molecule.

The first (and computationally most time-consuming) step for the calculation of the non-Markovian dynamics within our scheme is the coupling matrix $f^{\beta\gamma}_{\alpha\delta}(E)$. Exploiting its parity, it is displayed in Fig. 5.6 for positive energies E. The fully diagonal elements clearly dominate at any energy. The energetic width is about $\hbar s/L_{COM}$, as discussed for the single state case, Sect. (5.3).

After computation of the selfenergies $\Sigma_{\alpha\eta}(\Omega)$, the complex polarization $P(\Omega)$ is obtained. We display in Fig. 5.7 its imaginary part, that for a short pulse $E_{\mathrm{in}}(t)$ is

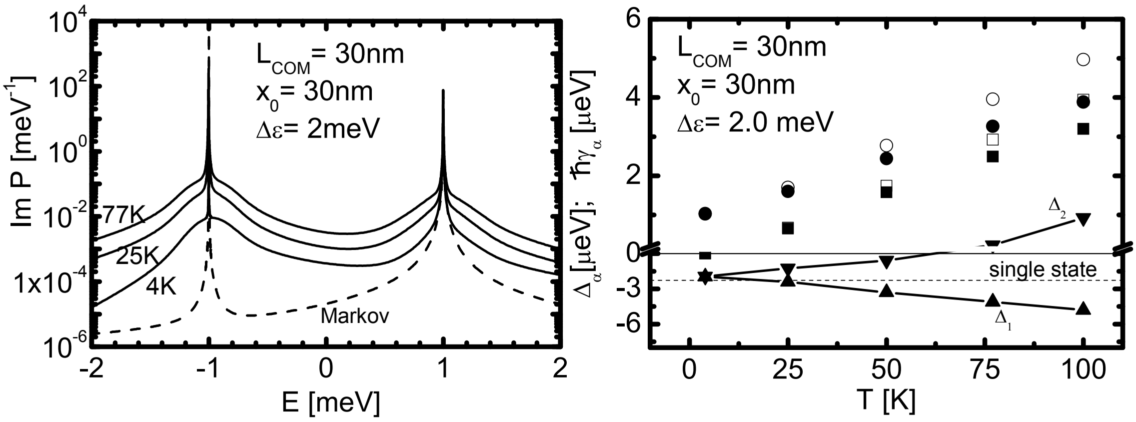

Figure 5.8: *Temperature dependence. Left panel: absorption spectrum at different temperatures compared to the Markov absorption at* 4 K. *Right panel: Deformation shifts* Δ_α *(triangles) and phonon scattering rates* $\hbar\gamma_\alpha$ *for state 1 (squares) and state 2 (circles). The single state (T-independent) deformation shift for a Gauss state with* $L_{COM} = 30\,\mathrm{nm}$ *is displayed as dashed line. Empty squares refer to the Markovian rates; full squares are the widths of the non-Markovian ZPL, fitted according to the procedure explained in App. (D.4).*

proportional to the absorption spectrum at normal incidence (Eq. (5.5)). The most prominent difference with respect to the Markovian absorption is the increased importance of the tails. This is the multi state manifestation of the BB found in the single state spectra, and represents the superposition of all phonon satellites. As seen in the inset of the left panel in Fig. 5.7, this broadening is accompanied by a tiny narrowing of the ZPL[14] with respect to the Lorentzian peaks of the Markovian spectrum. In the right panel of Fig. 5.7 the dynamics of the polarization amplitude $|P(t)|$ in the time frame is displayed. Apart from the beating feature, the Markov plot decays exponentially. The non-Markovian amplitude decays faster for short times: this is again similar to the single state situation, with an initial (*pure*) dephasing whose time-scale is about L_{COM}/s. For large times after impulsive excitation, an exponential decay with beating is seen. Its time constant is somewhat larger than the Markovian one, as a consequence of the ZPL narrowing.

In the Figures 5.8 to 5.12, the dependence on the simulation parameters is systematically investigated.

In the left panel of Fig. 5.8 the temperature dependence of the absorption is displayed. For increasing temperature, the BB gets more and more important with respect to the ZPL weights. In the right panel both the deformation shifts Δ_α and the phonon scattering rates $\hbar\gamma_\alpha$ for different temperatures are displayed. The deformation shifts are rather small, and like in the single state lay in the μeV-range, but now they can be also non negative. At low temperature, they seem to converge to the single state deformation shift: if the phonon occupation is low, the exciton states are effectively independent. We observe a trend towards increasing spectral separation ("level repulsion") as temperature is raised. The Markov phonon scatter-

---

[14] The name zero phonon line might be misleading in the contest of more than one states: indeed the ZPL are due in this case to the (phonon mediated) population relaxation among exciton states.

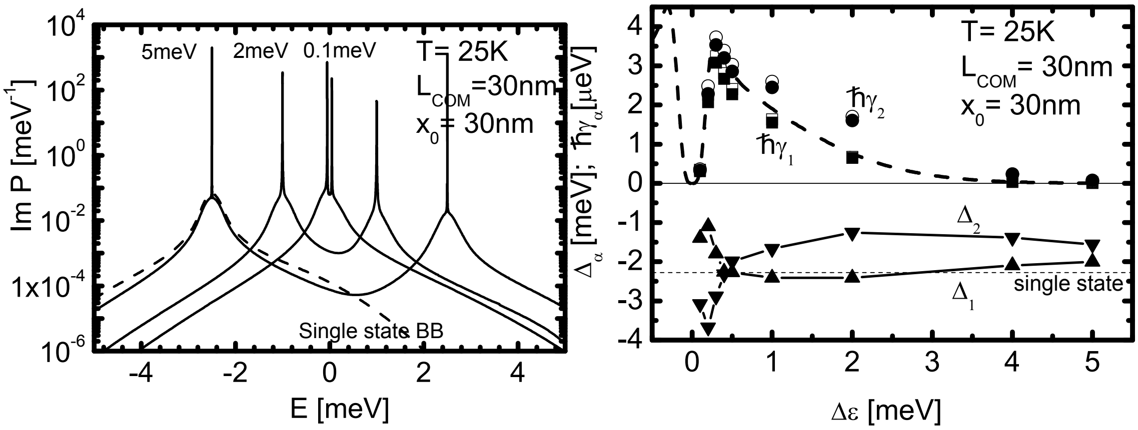

Figure 5.9: *Dependence on spectral separation* $\Delta\epsilon$. *Left panel: absorption spectrum; the single state BB of the ground state is given as a dashed line. Right panel: Deformation shifts* Δ_α *(triangles) and phonon scattering rates* $\hbar\gamma_\alpha$ *for state 1 (squares) and state 2 (circles). Symbols as in the right panel of Fig. 5.8. The dashed line is the Markov rate* $\hbar\gamma_1$*, calculated according to Eq. (5.25) using* $\epsilon_\beta - \epsilon_\alpha = \Delta\epsilon$.

ing rates differ of an amount which is temperature independent: this is the phonon emission rate at zero temperature. The non-Markovian phonon rates are defined by the widths of the ZPL, see App. (D.4). With this definition, it is found that they are always smaller than the Markovian rates calculated according to the Fermi golden rule, Eq. (5.25). This is possibly due to nondiagonal terms in the selfenergy. Both the discrepancy between Markovian and non-Markovian case and the module of the rates increase with temperature, because of increasing exciton-phonon interaction.

Fig. 5.9 shows the dependence on the spectral separation $\Delta\epsilon$. It is expected and found that if the separation is large compared to the width of the coupling function, single state BB are found. In the right panel, the $\Delta\epsilon$ dependence of the phonon rates exhibits a maximum. It is obvious that energetically very distant states are weakly coupled, while almost degenerate states are not favourite because of the bulk character of the phonon modes (see integration measure in Eq. (D.5)). Furthermore, the energy $\Delta\epsilon$ dependence is well reproduced by the Markov definition of scattering rate Eq. (5.25).

The dependence on size L_{COM} is shown in the left panel of Fig. 5.10. Like in the single state case, the BB get smaller for larger L_{COM} because the exciton states are localized in momentum space and thus couple to a fewer phononic degrees of freedom. However, the ZPL width displays the opposite behaviour, increasing for wider states. This is because the ZPL width is related to the offdiagonal matrix elements of the coupling matrix $f^{\beta\gamma}_{\alpha\delta}(E)$, which are responsible for real transitions (i.e., among different exciton states). Fig. 5.11 shows indeed that the largest of these matrix elements, $f^{22}_{11}(E)$ and $f^{22}_{12}(E)$, increase with increasing state size L_{COM}.

Finally in Fig. 5.12 absorption and phonon rates are calculated for varying state separation x_0. For small separation, the second state has very small oscillator strength, because of its node position; the second spectral peak gets optically more active for larger separations. The γ_α panel shows that the scattering efficiency dramatically decreases for large x_0: the deformation potential matrix elements $t^{\mathbf{q}}_{\alpha\beta}$ live of

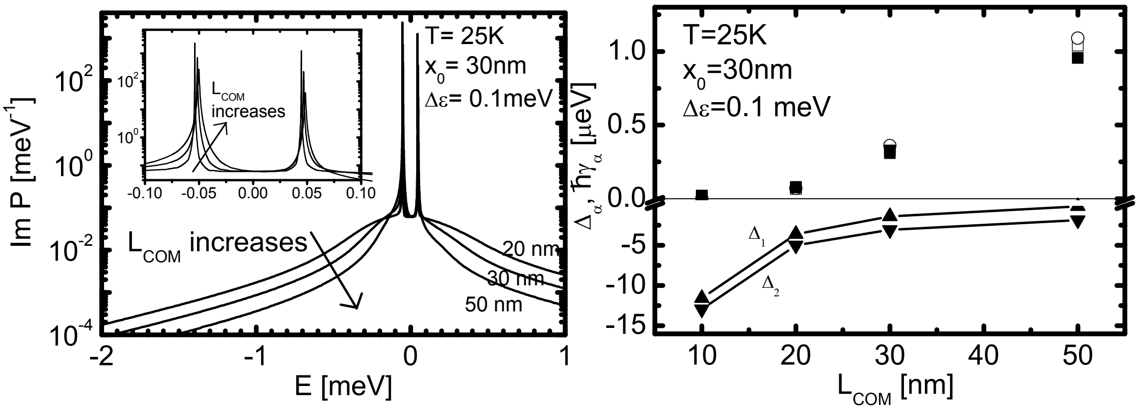

Figure 5.10: *Dependence on COM size L_{COM}. Left panel: absorption spectrum; notice that ZPL get larger whereas BB get smaller for increasing L_{COM}. Right panel: Markovian and non-Markovian rates $\hbar\gamma_\alpha$ and deformation shifts Δ_α, symbols as in the right panel of Fig. 5.8.*

the spatial overlap between wavefunction (Eq. (B.2)). For large separation x_0, the deformation shifts seem to converge to the single state value.

5.4.2 Simulation states

In this section the non-Markovian theory is applied to COM states resulting from realistic simulations of a disordered QW with $L_z = 5$nm. The material constants and the potential variance $\hbar\sigma$ =4.75 meV being used have already been chosen for the calculations of the Spectral Speckle Analysis close to the experiment (see Tab. 3.1). For this QW it is consistent to assume long radiative recombination times with respect to the phonon scattering times, especially at temperatures as high as $T = 25$K (see Fig. 3.3), thus neglecting r_α as we have done in our theoretical derivation in Sect. (5.1).

Attempting to compute a full non-Markovian absorption spectrum we soon meet a numerical limitation: the number of components of the coupling matrix $f^{\gamma\gamma}_{\alpha\eta}(E)$ scales as N_S^3, N_S being the number of COM states used. At the moment, the available computer memory limits us to use $N_S = 5$. Nevertheless, different groups of 5 states each can be used at different runs for exploring properties of energetically distinct regions of the absorption spectrum.

As shown in Fig. 5.13, we have studied groups of 5 adjacent states in the low-energy tail (A), around the absorption maximum (B), and in the high-energy tail (C) (see also top panel in Fig. 5.15). From the simulation with artificial states, we have learned that we can characterize non-Markovian effects by observing the importance of BB, the reduction of the individual rates γ_α and the size of the deformation shifts Δ_α.

The A states are well localized and do not have significant spatial overlaps, Fig. 5.14. They resemble the isolated Gaussian states used in Sect. (5.3). From the large values of the deformation shifts, we can infer a localization length $L_{COM} \sim 5$ nm or less, (cp. bottom panel in Fig. 5.15 to Fig. 5.5). The ZPL widths of these states (proportional to γ_α) are extremely small, both at Markov and non-Markovian level (bottom

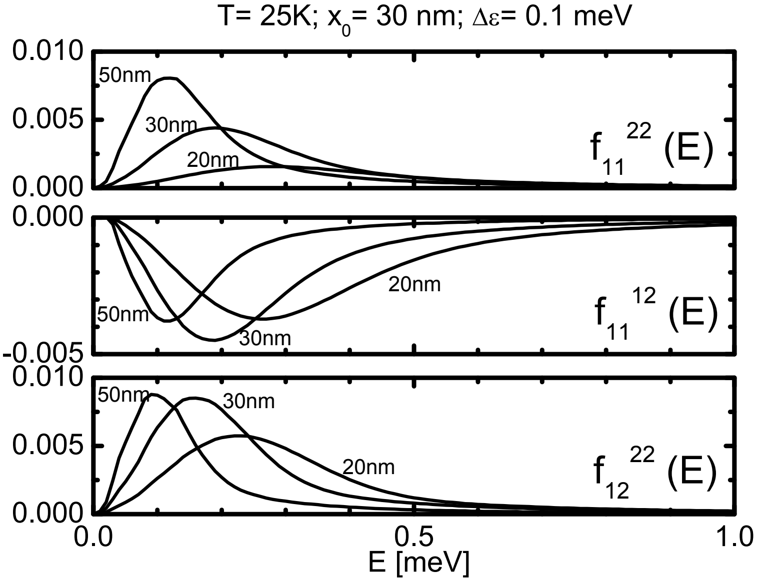

Figure 5.11: *Offdiagonal matrix elements $f_{11}^{22}(E)$ (top panel), $f_{11}^{12}(E)$ (middle panel), and $f_{12}^{22}(E)$ (bottom panel) for various state sizes L_{COM} as indicated.*

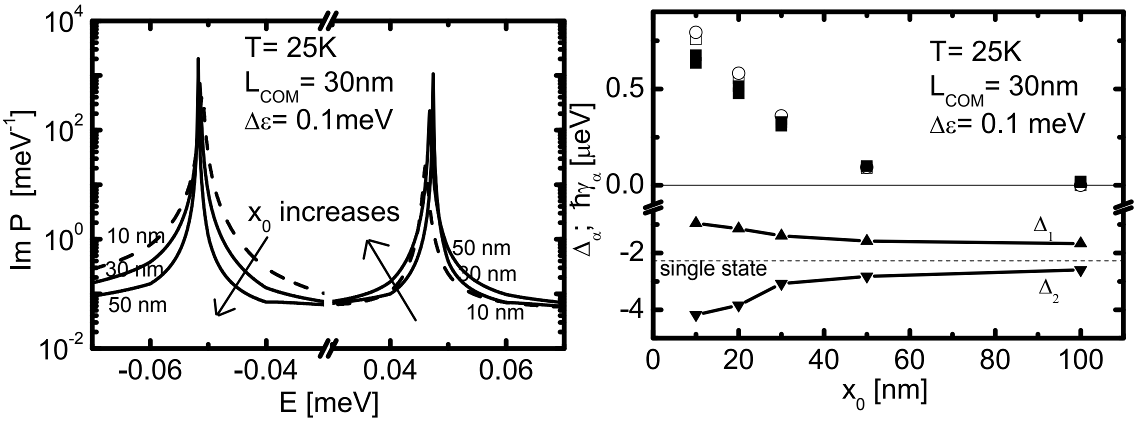

Figure 5.12: *Dependence on state separation x_0 . Left panel: absorption spectrum. Right panel: Markovian and non-Markovian rates $\hbar\gamma_\alpha$ and deformation shifts Δ_α, symbols as in the right panel of Fig. 5.8*

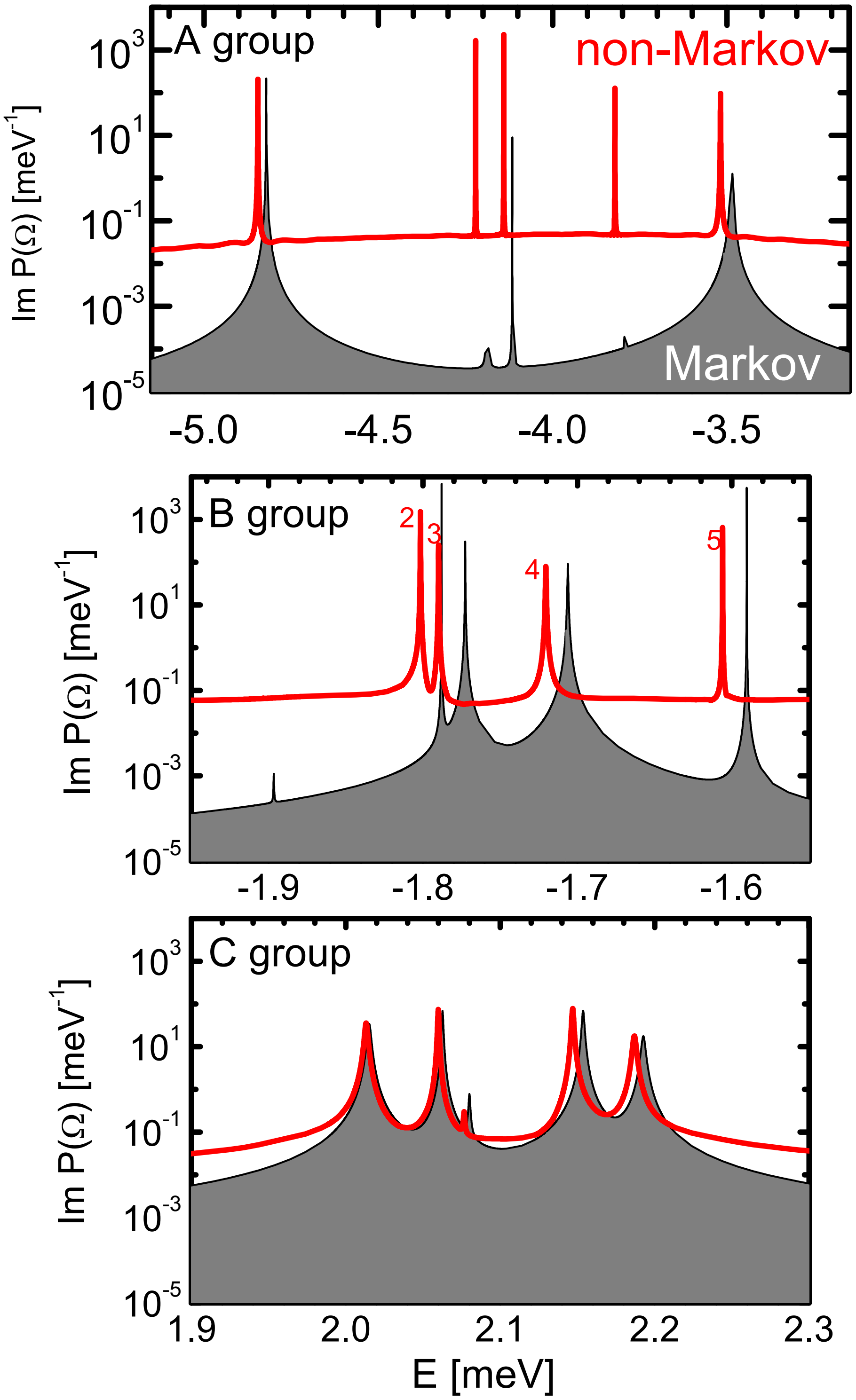

Figure 5.13: *Absorption spectra for 15 simulated QW states, organized in 3 groups of 5 states each. Black lines with shadows: Markov; red lines: non-Markovian. Notice that the energy window in the first panel is 5 times larger than in the other ones! The states of group B have been labelled for prompt identification. All results obtained for* $T = 25\,\mathrm{K}$.

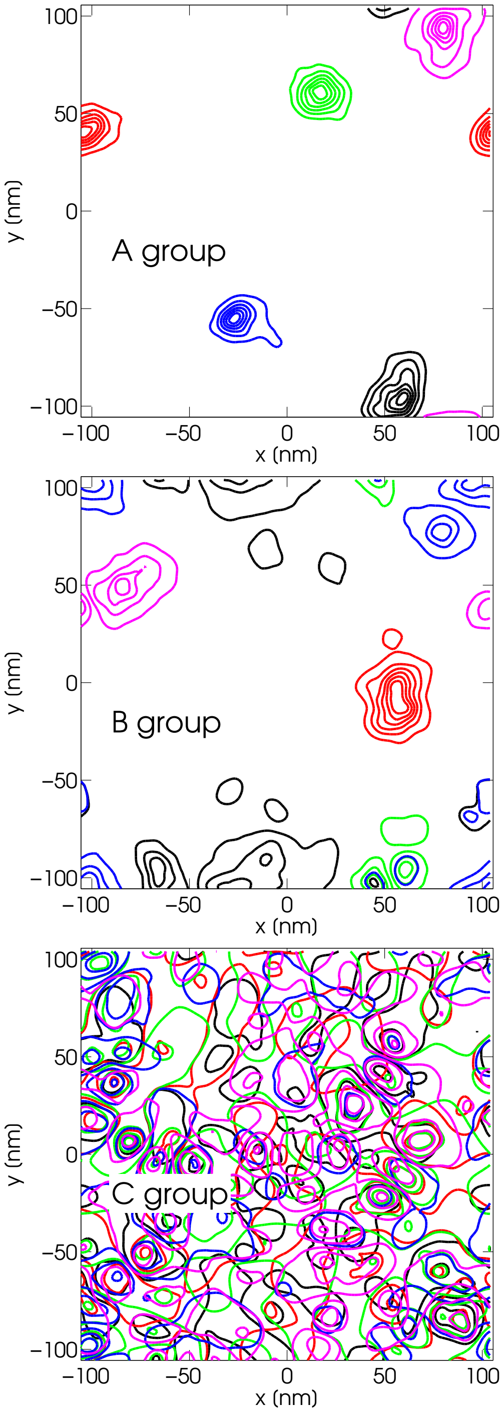

Figure 5.14: *Contour plots of the 3 groups of states used in the spectra of Fig. 5.13. Color code within each group: black=1st, red=2nd, green=3rd, blue=4th, magenta=5th state.*

panel in Fig. 5.15), as expected for spatially isolated states. The dominant effect is thus the background absorption between adjacent peaks, due to the non-Markovian BB. It manifests itself as a mostly constant contribution, due to the small L_{COM} size (cp. top left panel in Fig. 5.4).

The B states are also well localized, but some of them (like state 3 and 4) have some overlap with other states. This leads to wider ZPL and larger rates γ_α with respect to the A states. The deformation shifts are about half of the Δ_α obtained for the A states (notice that the energy window of the B panel is much smaller than in the A panel). Thus, the most important non-Markovian effect for this group is the BB formation.

The C states are qualitatively different from the others. They have many nodes and an appreciable overlap with all other states. The peak value of the oscillator strengths are reduced and the ZPL widths are much larger with respect to states A and B. The deviation between Markovian and non-Markovian γ_α is appreciable; we find confirmation for the trend that non-Markovian rates are smaller than Markovian ones, as already found for artificial states. Still the size of the computed γ_α could seem surprisingly small, when compared for instance to the results shown in Fig. 3.3. This is due to the small ($N_S = 5$) number of states here available for phonon-mediated transitions. The deformation shifts are strongly reduced. For this group of states, non-Markovian effect seem to be quantitatively not very important.

In conclusion, we can state that mostly the low-energy tail of the absorption is affected by non-Markovian exciton-phonon dynamics. These states exhibit large broad bands due to virtual transitions that do not involve relaxation of the exciton population.

The far-field absorption is probably only slightly affected by non-Markovian dynamics, since it is dominated by the ZPL of states with large scattering rates γ_α. A near-field PL-experiment would be desirable for checking the non-Lorentzian absorption lineshapes of the strongly localized states. The necessary resolution for selecting individual exciton wavefunctions ($\sim 30\,\text{nm}$, cp. top panel in Fig. 5.14) is within the range of nowadays' setups [46].

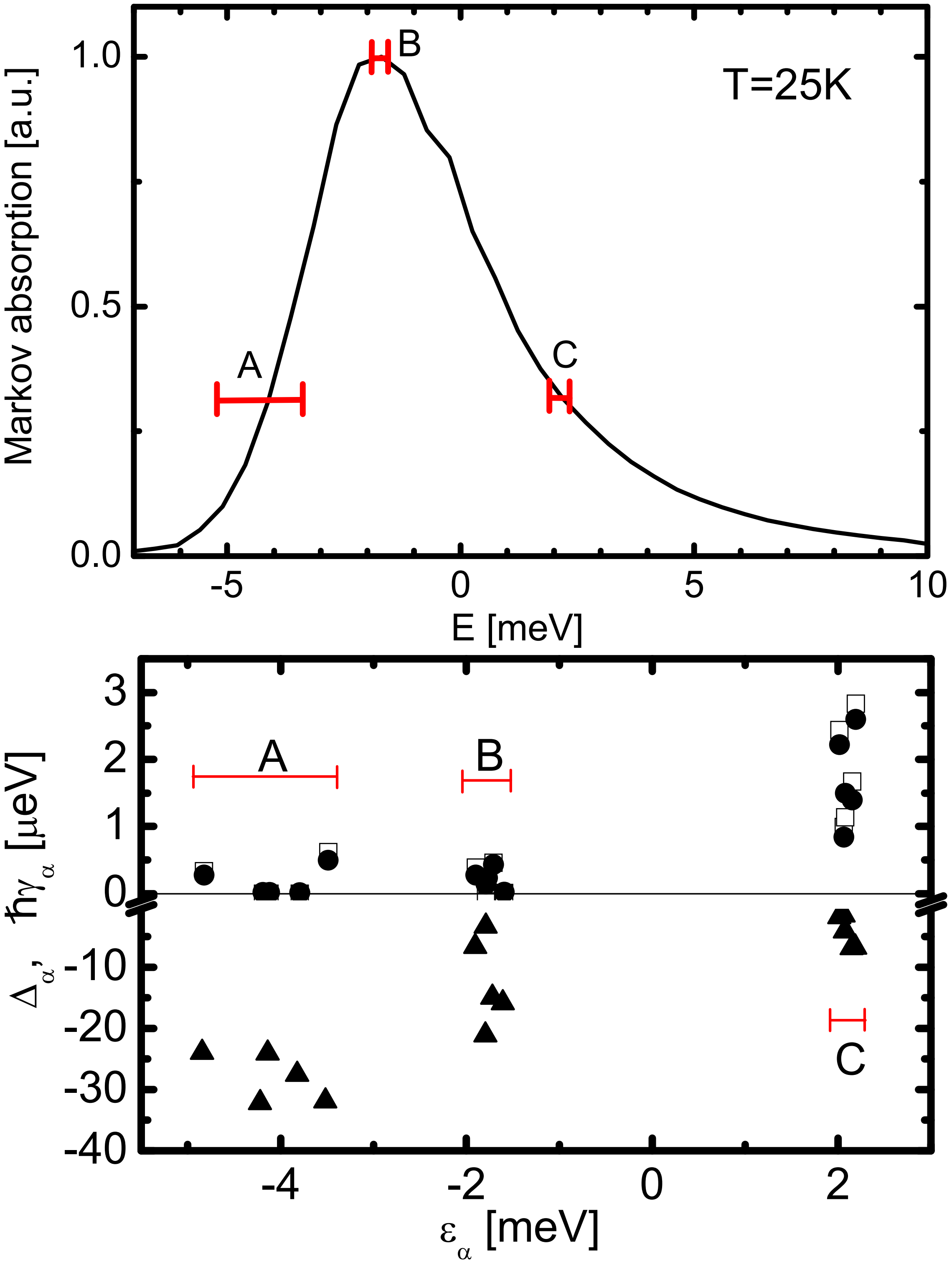

Figure 5.15: *Top panel: Markovian absorption spectrum for the same QW of Fig. 5.13, resulting from addition of about 150000 states. The energy windows of the panels of Fig. 5.13 are indicated. Bottom panel: deformation shifts* Δ_α *(triangles), Markovian (empty squares) and non-Markovian (full circles) phonon rates* $\hbar\gamma_\alpha$ *for the 15 states displayed in Fig. 5.14.*

Chapter 6

Summary and Outlook

The research work done along this PhD Thesis has dealt with three main topics, which are here summarized.

Spectral Speckle Analysis
The long-dated problem of the spectral features in the Rayleigh scattering in the SE from QW has been addressed. A microscopic density matrix approach allows to calculate both the coherent and the incoherent part of the spectra, accounting for disorder exactly (thanks to computer simulations of the corresponding eigenstates), and for exciton-phonon interaction in second order (all simulation results of this Chapter are within Markov approximation). The separation of the density matrix into a speckling part and a constant background is the key for the distinction between coherent and incoherent emission. Pulsed as well cw excitation can be taken into account within our formalism. Results for QW of different widths and at various bath temperature have been compared to experimental results. A good overall agreement is observed, with the coherent part of the emissions generally increasing at low temperature and for wider QW.

Sloped Speckles
The effect of the presence of both disorder and long range systematic potentials in QW samples has been investigated. A direct proportionality between local potential gradient and the tilting of the speckle pattern in momentum-time space is proved. Quadratic components in the potential are responsible for a widening of the speckle correlation function. While the major experimental outcome of these results is the possibility to replace space-resolved PL measurements (e.g., in situations where no optical imaging is possible), on the theoretical side the fascinating question of exciton delocalization could be addressed. For the experimentally realized strain (which causes the long-range potential) and for the optically observed disorder strength, it is found that excitons stay localized. However, numerical simulations show that, in presence of stronger potential gradients and weaker disorder, a delocalization transition occurs.

Non-Markovian exciton-phonon interaction
Here, an improvement of the state-of-the-art recipe for treating the exciton-phonon

interaction in QW is proposed. We have solved the 2nd Born density matrix equations of motion for systems containing more exciton levels, going beyond the usual Markov approximation for the exciton-phonon interaction. A frequency-domain formalism has been developed, which reduces the numerical task to the computation of proper selfenergy matrixes. After testing this theory on simple model functions for localized exciton states, realistic QW eigenstates resulting from numerical simulations of disordered landscapes have been employed. Non-Markovian effects manifest themselves as broad bands in the absorption spectrum, which are due to virtual transitions that do not change the exciton population (pure dephasing). These effects have been found to be mostly important in the low energy part of the spectra, originating from the most localized exciton states of the ensemble.

Open questions

Finally, it is clear that several questions are left unresolved by this work and could be investigated starting from the results achieved here.

In particular, it would be interesting to understand what is the origin of the quantitative discrepancies between theoretical and experimental results of the Spectral Speckle Analysis. Are they due only to our imperfect knowledge of the QW material constants, in particular of the deformation potential constants? Or do some other dephasing mechanism beyond the exciton-phonon interaction play a significant role in the experiment?

The question of the exciton delocalization in presence of long-range potential could be also addressed in a deeper way. The role of phonon scattering in this context should be clarified: would it help excitons to be accelerated to regions of lower potential energy? How should we characterize this transition between localized and delocalized regime? Are there scaling arguments applying here?

Perhaps, the most interesting questions arise from the non-Markovian dynamics part. First of all, it would be desirable to improve the numerical technique for dealing with larger sets of simulation states. Finally, a comparison with near-field experiments would be interesting. Computation of the non-Markovian dynamics for the full density-matrix could give access to modifications of the speckle statistics in the SE.

Part III

Appendix

Appendix A

Appendices to Chapter 2

A.1 Intensity probability density

For the computation of the intensity probability density an expansion in terms of moments of the electrical field is used. As a consequence of the conditions i), ii), iii) of Sect. (2.1), the following moments of the real part A_R of the emitted field are calculated (the average $\langle \cdots \rangle$ is here an ensemble average):

$$\begin{aligned}
\langle A_R \rangle &= \sum_{j=1}^{N} \langle a_j \cos(\Phi_j) \rangle \underset{i}{=} \sum_{j=1}^{N} \langle a_j \rangle \langle \cos(\Phi_j) \rangle \underset{\text{(ii)}}{=} 0 \\
\left\langle A_R^2 \right\rangle &= \sum_{j,k=1}^{N} \langle a_j a_k \rangle \langle \cos(\Phi_j) \cos(\Phi_k) \rangle \underset{\text{(iii)}}{=} \frac{1}{2} \sum_{j=1}^{N} \left\langle a_j^2 \right\rangle \equiv \frac{1}{2} I_0 \\
\left\langle A_R^{(2p-1)} \right\rangle &= 0 \\
\left\langle A_R^{(2p)} \right\rangle &= \frac{I_0^p}{2^p} (2p-1)(2p-3) \cdots 1 = I_0^p \, (2p-1)!! \, 2^{-p} \, .
\end{aligned} \tag{A.1}$$

Using these moments the characteristic function $\left\langle e^{iuA_R} \right\rangle$ can be evaluated as

$$\left\langle e^{iuA_R} \right\rangle = \sum_{p=0}^{\infty} (iu)^{2p} \frac{\left\langle A_R^{(2p)} \right\rangle}{(2p)!} = \sum_{p=0}^{\infty} \frac{(iu)^{2p} I_0^p}{p! \, 2^{2p}} = \exp\left(-\frac{u^2 I_0}{4} \right) \tag{A.2}$$

and the probability that the real part of the field is equal to E_x is given by

$$p(E_x) = \langle \delta(A_R - E_x) \rangle = \frac{1}{2\pi} \int du \, e^{-iuE_x} \left\langle e^{iuA_R} \right\rangle = \frac{1}{\sqrt{\pi I_0}} \exp\left(-\frac{E_x^2}{I_0} \right) . \tag{A.3}$$

This result is equivalent to the central limit theorem. Indeed the results for the pair contractions given in Eq. (A.1) are valid only in the limit of large N and the form of the distribution of the a_j's is unimportant. Since real and imaginary part of the field are uncorrelated,

$$\left\langle A_R^{(2p)} A_I^{(2q)} \right\rangle = \left\langle A_R^{(2p)} \right\rangle \left\langle A_I^{(2q)} \right\rangle , \tag{A.4}$$

the conditional probability is

$$p(E_x, E_y) = \frac{1}{\pi I_0} \exp\left(-\frac{E_x^2 + E_y^2}{I_0}\right) . \tag{A.5}$$

Using the Jacobian for the transformation into the new variables ($I = E_x^2 + E_y^2, \varphi = \mathrm{arctg}(E_x/E_y)$) an exponential probability density for the intensity I in terms of the average coherent intensity I_0 is obtained

$$p(I) = \int_0^{2\pi} d\varphi \, p(I, \varphi) = \frac{\theta(I)}{I_0} \exp\left(-\frac{I}{I_0}\right) . \tag{A.6}$$

A.2 Correlation function and coherence degree

Here we show that correlation function and coherence degree are simply related. If the total intensity can be decomposed as

$$I(s) = A(s) + B_{\mathbf{k}}(s) , \tag{A.7}$$

where $\langle A(s)\rangle_{\mathbf{k}} = A(s)$ and $\langle B_{\mathbf{k}}(s)\rangle_{\mathbf{k}} = B_0(s)$, then the intensity-intensity correlation,

$$C(s, \Delta s) = \frac{\langle I(s - \Delta s/2) I(s + \Delta s/2)\rangle_{\mathbf{k}}}{\langle I(s - \Delta s/2)\rangle_{\mathbf{k}} \cdot \langle I(s + \Delta s/2)\rangle_{\mathbf{k}}} - 1 , \tag{A.8}$$

due to subtraction of the product of average values, correlates in the numerator only the $\mathbf{k}$ depending part,

$$C(s, \Delta s) = \frac{\langle B_{\mathbf{k}}(s - \Delta s/2) B_{\mathbf{k}}(s + \Delta s/2)\rangle_{\mathbf{k}}}{\langle I(s - \Delta s/2)\rangle_{\mathbf{k}} \cdot \langle I(s + \Delta s/2)\rangle_{\mathbf{k}}} - 1 . \tag{A.9}$$

In particular for $\Delta s = 0$ it is,

$$C(s, 0) = \frac{\langle B_{\mathbf{k}}^2(s)\rangle_{\mathbf{k}} - \langle B_{\mathbf{k}}(s)\rangle_{\mathbf{k}}^2}{\langle I(s)\rangle_{\mathbf{k}} \cdot \langle I(s)\rangle_{\mathbf{k}}} = \kappa^2(s) , \tag{A.10}$$

where the second equality follows from the definition of contrast Eq. (2.3). Now, if $B_{\mathbf{k}}(s)$ is exponentially distributed, $p(B_{\mathbf{k}}) = \theta(B_{\mathbf{k}}) B_0^{-1} \exp(-B_{\mathbf{k}}/B_0)$, then it is

$$C(s, 0) = \left(\frac{B_0(s)}{\langle I(s)\rangle_{\mathbf{k}}}\right)^2 . \tag{A.11}$$

Since in our case $B_{\mathbf{k}}(s)$ corresponds to the coherent and $A(s)$ to the incoherent intensity, we have found that

$$C(s, 0) = c^2(s) \tag{A.12}$$

which, combined with Eq. (A.10), leads to

$$\kappa(s) = c(s) . \tag{A.13}$$

Thus, thanks to our definition Eq. (A.8), the normalization of the correlation is easily related to the coherence degree, and speckle contrast κ and coherence degree c are found to be identical.

Appendix B

Appendices to Chapter 3

B.1 Deformation potential matrix elements

The deformation potential matrix element between two exciton states $\Psi_\alpha(\mathbf{r}_e\mathbf{r}_h)$ and $\Psi^*_\beta(\mathbf{r}_e\mathbf{r}_h)$ is given in general by [62]

$$t^{\mathbf{q}}_{\alpha\beta} = \sqrt{\frac{\hbar w_{\mathbf{q}}}{2s^2\rho_B\,V}}\int\!\!\int d\mathbf{r}_e d\mathbf{r}_h\,\Psi^*_\beta(\mathbf{r}_e\mathbf{r}_h)\left(D_c e^{i\mathbf{q}\cdot\mathbf{r}_e}\;-\;D_v e^{i\mathbf{q}\cdot\mathbf{r}_h}\right)\Psi_\alpha(\mathbf{r}_e\mathbf{r}_h)\,. \tag{B.1}$$

Here, the deformation potential constants D_a, the bulk sound velocity s, the mass density ρ_B, and the normalization volume V appear. As discussed in Sect. (3.1), we perform a single-sublevel approximation and factorize COM and relative part of the in-plane motion. Now the deformation potential matrix element takes the form

$$t^{\mathbf{q}}_{\alpha\beta} = \sqrt{\frac{\hbar\,s\,q}{2s^2\rho_B V}}\left[D_c K_e(q_z)\chi(\mathbf{q}_\|/\eta_e) - D_v K_h(q_z)\chi(\mathbf{q}_\|/\eta_h)\right](\psi_\alpha\psi_\beta)_{\mathbf{q}_\|} \tag{B.2}$$

with

$$\begin{aligned}
K_a(q_z) &= \int dz\,u_a^2(z)\,e^{-iq_z z}\\
\chi(\mathbf{q}_\|) &= \int d\boldsymbol{\rho}\,\phi^2_{1s}(\boldsymbol{\rho})\,e^{-i\mathbf{q}_\|\cdot\rho}\\
(\psi_\alpha\psi_\beta)_{\mathbf{q}_\|} &= \int d\mathbf{R}\,\psi_\alpha(\mathbf{R})e^{-i\mathbf{q}_\|\cdot\mathbf{R}}\psi_\beta(\mathbf{R})\,.
\end{aligned} \tag{B.3}$$

$K_a(q_z)$ and $\chi(\mathbf{q}_\|)$ represent the Fourier transforms of the squared confinement and relative wavefunctions $u^2_{e,h}$ and ϕ^2_{1s}, respectively. In particular, Gauss confinement and hydrogenic relative motion are used, leading to:

$$\begin{aligned}
K_a(q_z) &= \exp\left(-\frac{1}{2}(q_z L_a)^2\right)\\
\chi(\mathbf{q}_\|) &= \left(1+(q_\| a_B/2)^2\right)^{-3/2}\,,
\end{aligned} \tag{B.4}$$

where the values for the electron and hole confinement lenghts L_a in growth direction and the exciton QW Bohr radius are used, that are listed in Tab. B.2 on page 90.

These values result from a variational computation.
The used material constants for bulk GaAs that enter formula Eq. (B.2) are given in Tab. B.1.

mass density [56]	ρ_B	5.37	g/cm^3
longitudinal sound velocity [56]	s	5330	m/s
def. pot. electrons [56]	D_c	-7000	meV
def. pot. holes [56]	D_v	+3500	meV
electron mass ratio	$\eta_e = M/m_h$	1/0.7	
hole mass ratio	$\eta_h = M/m_e$	1/0.3	

Table B.1: *Material constants for bulk GaAs that appear in Eq. (B.2).*

B.2 Dipole matrix elements

The dipole matrix element of a wavefunction $\Psi_\alpha(\mathbf{r}_e\mathbf{r}_h)$ is given by

$$m_{\alpha\mathbf{q}} = \langle \mathbf{q}|\mu_{\rm cv}|\Psi\rangle = \mu_{\rm cv}\int d\mathbf{r}\, e^{i\mathbf{q}\cdot\mathbf{r}}\Psi_\alpha(\mathbf{r},\mathbf{r}). \tag{B.5}$$

Within the factorization Ansatz,

$$m_{\alpha\mathbf{q}} = \mu_{\rm cv}\phi_{1s}(0)O_{eh}(q_z)\psi_{\alpha\mathbf{q}_\parallel}\,, \tag{B.6}$$

where

$$\psi_{\alpha\mathbf{q}_\parallel} = \int d\mathbf{R}\psi_\alpha(\mathbf{R})E_{\rm in}(\mathbf{R})e^{i\mathbf{q}_\parallel\cdot\mathbf{R}} \approx\; E_{\rm in}(\mathbf{R}_\alpha)\, e^{i\mathbf{q}_\parallel\cdot\mathbf{R}_\alpha}\int d\mathbf{R}\psi_\alpha(\mathbf{R})\,. \tag{B.7}$$

Since the focus profile $E_{\rm in}(\mathbf{R})$ and the light wavelength are usually much larger than the typical COM localization length, the corresponding factors have been extracted out of the integral and evaluated at the state center $\mathbf{R}_\alpha$ defined as

$$\mathbf{R}_\alpha = \int d\mathbf{R}\,\mathbf{R}\,\psi^2_\alpha(\mathbf{R})\,. \tag{B.8}$$

B.3 Radiative rates

For a correct treatment of the radiative coupling, also the light polarization has to be taken into account, [4]. It leads to the radiative rates

$$r_\alpha = \frac{2\pi}{\hbar}\sum_{\mathbf{k}}|m_{\alpha\mathbf{k}}|^2\left(g^{TE}_{\mathbf{k}} + g^{TM}_{\mathbf{k}}\right)\delta(\epsilon^{(0)}_\alpha - \hbar\Omega_{\mathbf{k}})\,, \tag{B.9}$$

where

$$g^{TE}_{\mathbf{k}} = g^{TM}_{\mathbf{k}}\frac{k^2}{k_z^2} = \frac{\pi\hbar\omega_{\mathbf{k}}}{\varepsilon_S V} \tag{B.10}$$

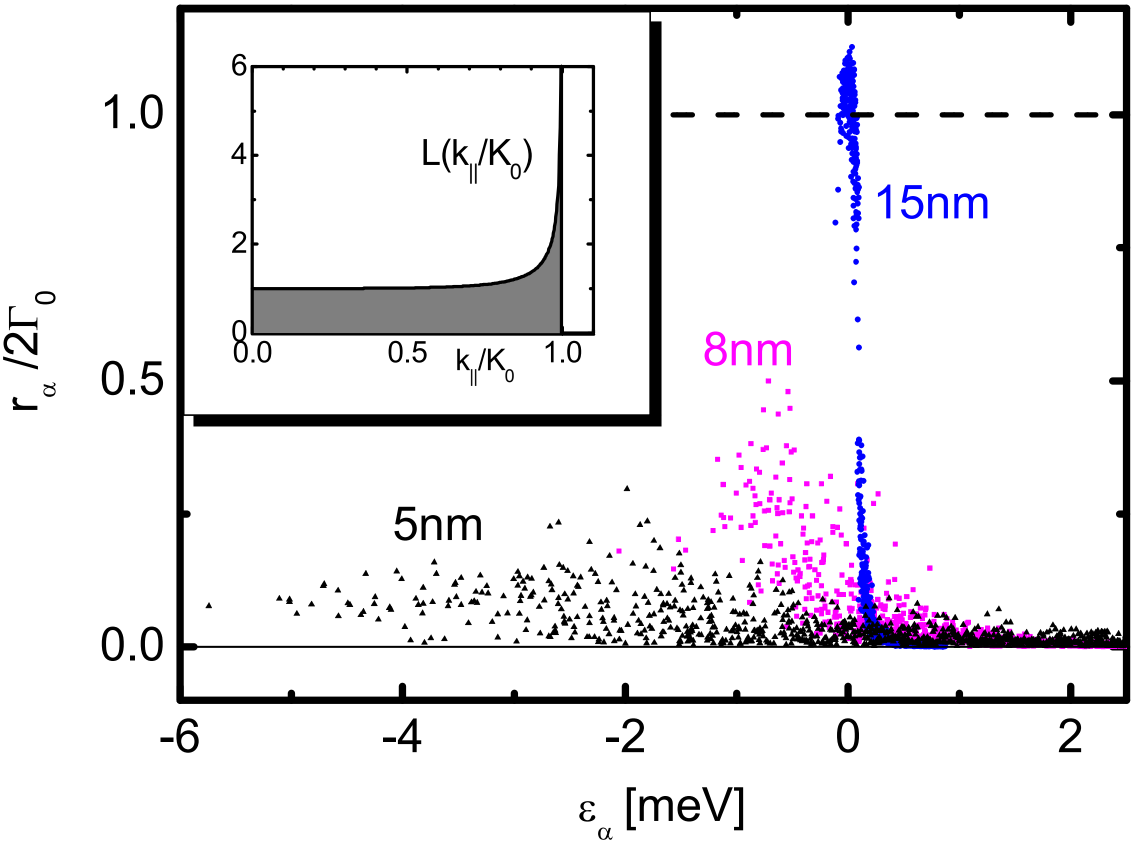

Figure B.1: *Radiative rates normalized to* $2\Gamma_0$ *for QW of different widths. Triangles:* L_z*=5 nm; squares:* L_z*=8 nm; circles:* L_z*=15 nm. The inset shows the light-cone function* $L(k_{\|}/K_0)$.

account for the transverse electric (TE) and magnetic (TM) modes (ε_b is the background dielectric constant in the excitonic region). The summation is meant over a three dimensional space; V is the normalization volume. Eliminating the delta function using $K_0^2 \equiv {k_{\|}}^2 + k_z^2 = \left(\epsilon_\alpha \sqrt{\varepsilon_b}/\hbar c\right)^2$, we get

$$r_\alpha = \frac{2\Gamma_0}{A} \sum_{\mathbf{k}_{\|}} L(k_{\|}/K_0)\, |\psi_{\alpha \mathbf{k}_{\|}}|^2 \tag{B.11}$$

with the light-cone function

$$L(x) = \frac{\Theta(1-x^2)}{\sqrt{1-x^2}}\,(1-x^2/2)\,. \tag{B.12}$$

The summation in Eq. (B.11) is over a two dimensional space; A is the normalization area in the QW plane. As a consequence of energy conservation, the in-plane momentum $k_{\|}$ has to be smaller than K_0. This region of photon momentum is called *light cone.*

The prefactor $2\Gamma_0$ has the physical meaning of radiative rate for a plane-wave exciton state $\psi_{\mathbf{Q}\mathbf{k}_{\|}} = \sqrt{A}\,\delta_{\mathbf{Q},\mathbf{k}_{\|}}$ at zero COM momentum, $Q = 0$. Nevertheless, the rate r_α can exceed $2\Gamma_0$ for plane waves with $Q \sim K_0$, which explore the light-cone

L_z[nm]	L_e[nm]	L_h[nm]	a_B [nm]	$\hbar\Gamma_0$ [μeV]	C [10^6 s^{-1} nm^{-2}]
5	1.69	1.34	9.9	34	9.3
8	2.10	1.86	10.7	29 (26)	8.0 (7.0)
15	3.47	3.15	12.4	22 (26)	6.0 (7.0)
∞	-	-	12.8	-	-

Table B.2: *Exciton Bohr radius a_B, electron L_e and hole L_h confinement lengths in growth direction z, coupling constants Γ_0 and overall radiative prefactors C for QW of different widths L_z. ($L_z = \infty$ refers to the bulk situation). The values among brackets were used in the computations.*

in proximity of its (integrable) singularity, cp. Fig. B.1.

We have used the matrix element of Eq. (B.6), which implies

$$\Gamma_0 = \frac{2\pi}{\hbar}\frac{K_0}{\varepsilon_S}\,\mu_{\rm cv}^2\,\phi_{1s}^2(0)\,O_{eh}^2\,. \tag{B.13}$$

An important simplification is possible for localized exciton states. In this case $|\psi_{\alpha\mathbf{k}_\|}|^2$ is practically constant within the light cone and we obtain

$$r_\alpha = C\cdot|\psi_{\alpha\mathbf{k}_\|=0}|^2\,;\quad C = \frac{2}{3\pi}\Gamma_0 {K_0}^2\,. \tag{B.14}$$

Andreani [5] computed $\hbar\Gamma_0 = 26\mu$eV for a SQW with $L_z = 10$nm. This allows to obtain the coupling also for other well widths, since the only L_z-sensitive factor is $\phi_{1s}^2(0) = 2/(\pi a_B^2)$. Using $K_0 = 0.0277\,\text{nm}^{-1}$ (GaAs bulk parameters: $\epsilon_\alpha \sim E_x = 1.516\,$eV and $n \equiv \sqrt{\epsilon_b} = 3.6$), we get the results listed in Tab. B.2.

In Fig. B.1 we see that, apart of the coupling constant Γ_0, exciton states belonging to wider QW have larger oscillator strengths. This is because a larger portion of these states is localized within the light cone.

B.4 Two-time density matrix

For obtaining the two-time density matrix, the time evolution of single-time operators is used. The equation of motion for $B_\alpha^\dagger(t)$ in 2nd Born Markov quality (cp. first line of Eq. (3.34)),

$$(-i\hbar\partial_t - \epsilon_\alpha - i\hbar\Gamma_\alpha)B_\alpha^\dagger(t) = S_\alpha(t) \tag{B.15}$$

allows to produce the equation for $N_{\alpha\beta}(t,t_2) = \langle B_\alpha(t)B_\beta^\dagger(t_2)\rangle$

$$\partial_t N_{\alpha\beta}(t,t_2) = (\omega_\alpha + i\Gamma_\alpha)N_{\alpha\beta}(t,t_2) + S_\alpha(t)P_\beta^*(t_2)\,, \tag{B.16}$$

(we have defined $\epsilon_\alpha \equiv \hbar\omega_\alpha$). Taking as start time $t_2 < t_1$, Eq. (B.16) is integrated to

$$N_{\alpha\beta}(t_1,t_2) = N_{\alpha\beta}(t_2,t_2)e^{(i\omega_\alpha-\Gamma_\alpha)(t_1-t_2)} + P_\beta^*(t_2)\int_{t_2}^{t_1} dt' iS_\alpha(t')e^{(i\omega_\alpha-\Gamma_\alpha)(t_1-t')} \tag{B.17}$$

The same integral appears integrating Eq. (B.15) between t_2 and t_1 and taking the expectation value,

$$P_\alpha(t_1) = P_\alpha(t_2) e^{(i\omega_\alpha - \Gamma_\alpha)(t_1 - t_2)} + \int_{t_2}^{t_1} dt' i S_\alpha(t') e^{(i\omega_\alpha - \Gamma_\alpha)(t_1 - t')} \,. \tag{B.18}$$

Therefore, replacing in Eq. (B.17) we obtain

$$N_{\alpha\beta}(t_1, t_2) = P_\alpha(t_1) P_\beta(t_2)^* + e^{(i\omega_\alpha - \Gamma_\alpha)(t_1 - t_2)} D_{\alpha\beta}(t_2, t_2) \qquad (t_1 > t_2) \,. \tag{B.19}$$

In the opposite case ($t_1 < t_2$) the other variable (t_2) is derived in Eq. (B.16) and one ends up with

$$N_{\alpha\beta}(t_1, t_2) = P_\alpha(t_1) P_\beta(t_2)^* + e^{(-i\omega_\beta - \Gamma_\beta)(t_2 - t_1)} D_{\alpha\beta}(t_1, t_1) \qquad (t_1 < t_2) \,. \tag{B.20}$$

Both cases and the limit situation ($t_1 = t_2$) are contained in the compact expression

$$N_{\alpha\beta}(t_1, t_2) = \underbrace{P_\alpha(t_1) P_\beta(t_2)^*}_{\text{coherent}} + \underbrace{\delta_{\alpha\beta}\, e^{i\omega_\alpha(t_1 - t_2) - \Gamma_\alpha |t_1 - t_2|} D_{\alpha\alpha}(\min\{t_1, t_2\})}_{\text{incoherent}} \,, \tag{B.21}$$

which exploits the property that (in the Markov approximation) the single-time incoherent density matrix is diagonal. We have also indicated which parts of the density matrix contribute to the coherent (speckled) and incoherent emission (see Sect. (B.5)).

B.5 Frequency resolved intensity

The starting point for the frequency resolved results is Eq. (3.40). Assuming Lorentz spectral resolution, $\mathcal{G}(\omega, t) = \theta(t) \exp((i\omega - \delta)t)$, we get

$$\begin{aligned} I_{\mathbf{k}}(\omega) &= \int dt\, I_{\mathbf{k}}(\omega, t) = \frac{1}{2\delta} \int dt_1 \int dt_2 \,\times \\ & \quad e^{-i\omega(t_1 - t_2) - \delta |t_1 - t_2|} \sum_{\alpha\beta} m^*_{\alpha\mathbf{k}} m_{\beta\mathbf{k}} N_{\alpha\beta}(t_1, t_2) \,. \end{aligned} \tag{B.22}$$

The incoherent intensity is originated by the incoherent part of the two-time density matrix (see Eq. (B.21)). Discarding the prefactor δ^{-1} and changing variables to $s = t_1 - t_2$ and $t = (t_1 + t_2)/2$ we get

$$\begin{aligned} I^{\text{inc}}_{\mathbf{k}}(\omega) &= \frac{1}{2} \sum_\alpha |m_{\alpha\mathbf{k}}|^2 \int ds\, e^{i(\omega_\alpha - \omega)s} e^{-(\Gamma_\alpha + \delta)|s|} \int dt\, D_{\alpha\alpha}(t - \frac{|s|}{2}) \\ &= \sum_\alpha |m_{\alpha\mathbf{k}}|^2 \frac{\Gamma_\alpha + \delta}{(\omega - \omega_\alpha)^2 + (\Gamma_\alpha + \delta)^2} D_\alpha \,, \end{aligned} \tag{B.23}$$

where $D_\alpha = \int dt\, D_{\alpha\alpha}(t)$ is obtained integrating the rate equation Eq. (3.36) with the boundary conditions $D_{\alpha\alpha}(t = \pm\infty) = 0$:

$$0 = \sum_\eta \gamma_{\alpha \leftarrow \eta} \left[R_\eta + D_\eta \right] - 2\Gamma_\alpha D_\alpha \,. \tag{B.24}$$

In the source term, also the coherent population R_α appears. It is given by

$$R_\alpha = \int dt\, |P_\alpha(t)|^2 = \frac{|m_{\alpha 0}|^2}{2\pi\hbar^2} \int d\omega' \, \frac{E_{\mathrm{in}}^2(\omega')}{(\omega' - \omega_\alpha)^2 + \Gamma_\alpha^2} \,. \tag{B.25}$$

The spectrally resolved coherent intensity follows from the product of polarizations in Eq. (B.21). We find

$$\begin{aligned} I_{\mathbf{k}}^{\mathrm{coh}}(\omega) &= \frac{1}{2} \sum_{\alpha\beta} m_{\alpha\mathbf{k}}^* m_{\beta\mathbf{k}} \frac{1}{(2\pi)^2} \int d\omega_1 \int d\omega_2 \, P_\alpha(\omega_1) P_\beta^*(\omega_2) \times \\ & \quad \int ds\, e^{i((\omega_1+\omega_2)/2-\omega)-\delta|s|} \int dt\, e^{i(\omega_1-\omega_2)t} \\ &= \frac{1}{2\hbar^2} \sum_{\alpha\beta} m_{\alpha\mathbf{k}}^* m_{\beta\mathbf{k}} m_{\alpha 0} m_{\beta 0}^* \times \\ & \quad \int d\omega' \frac{E_{\mathrm{in}}^2(\omega')}{(\omega' - \omega_\alpha - i\Gamma_\alpha)(\omega' - \omega_\beta + i\Gamma_\beta)} \frac{\delta/\pi}{(\omega - \omega')^2 + \delta^2} . \end{aligned} \tag{B.26}$$

For ideal resolution ($\delta \to 0$) we get

$$I_{\mathbf{k}}^{\mathrm{coh}}(\omega) = E_{\mathrm{in}}^2(\omega) \frac{1}{2\hbar^2} \sum_{\alpha\beta} m_{\alpha\mathbf{k}}^* m_{\beta\mathbf{k}} m_{\alpha 0} m_{\beta 0}^* \frac{1}{(\omega - \omega_\alpha - i\Gamma_\alpha)(\omega - \omega_\beta + i\Gamma_\beta)} \,. \tag{B.27}$$

Applying also the speckle averaging (which selects only terms with $\alpha = \beta$), we arrive at

$$I_{\mathbf{k}}^{\mathrm{coh}}(\omega) = E_{\mathrm{in}}^2(\omega) \frac{1}{2\hbar^2} \sum_{\alpha} |m_{\alpha\mathbf{k}} m_{\alpha 0}|^2 \frac{1}{(\omega - \omega_\alpha)^2 + \Gamma_\alpha^2} \,. \tag{B.28}$$

Finally, we notice that at high temperatures a simple equilibrium distribution for D_α is obtained. In this case we neglect the radiative rates with respect to the phonon rates in Eq. (B.24). Then we exploit that $\gamma_{\alpha\leftarrow\eta}$ and $\gamma_{\eta\leftarrow\alpha}$ are related by

$$\frac{\gamma_{\alpha\leftarrow\eta}}{\gamma_{\eta\leftarrow\alpha}} = \exp\left(-2(\epsilon_\beta - \epsilon_\alpha)/(k_B T)\right) \,, \tag{B.29}$$

which is obvious after Eq. (5.25). Therefore

$$D_\alpha \underset{T\to\infty}{\longrightarrow} D \exp(-\epsilon_\alpha/(k_B T)) \equiv N_\alpha^{\mathrm{Boltz}} \tag{B.30}$$

follows.

B.6 Photon conservation law

A simple relation between the total number of absorbed and emitted photons holds. Introducing the total integrated density $N_\alpha^{\mathrm{tot}} = R_\alpha + D_\alpha$, we rewrite the kinetic equation Eq. (B.24) as

$$2\Gamma_\alpha R_\alpha = 2\Gamma_\alpha N_\alpha^{\mathrm{tot}} - \sum_\eta \gamma_{\alpha\leftarrow\eta} N_\eta^{\mathrm{tot}} \,. \tag{B.31}$$

Replacing the definition $2\Gamma_\alpha = r_\alpha + \sum_\eta \gamma_{\eta\leftarrow\alpha}$ and summing over all exciton states we have

$$\sum_\alpha 2\Gamma_\alpha R_\alpha = \sum_\alpha r_\alpha N_\alpha^{\mathrm{tot}} \,. \tag{B.32}$$

The l.h.s. of the previous equation can be interpreted as total number of absorbed photons. Defining the total number of emitted photons as $I^{\mathrm{tot}} = (1/\pi)\int d\omega\,(I^{\mathrm{coh}}(\omega) + I^{\mathrm{inc}}(\omega))$, and recalling the approximate expression for R_α, Eq. (B.25), we find the equivalence

$$I^{\mathrm{tot}} = \sum_\alpha 2\Gamma_\alpha R_\alpha \,. \tag{B.33}$$

The total emission is set by the coherent population R_α. This conservation law can be used as a test of the overall numerical accuracy, since the r.h.s. does not depend on the relaxation kinetics of Eq. (B.24).

Appendix C

Appendices to Chapter 4

C.1 Polarization equation of motion

For determining the polarization dynamics we have to set up a proper Hamiltonian. Here we are interested only on the role of disorder and systematic potential, which can be view collectively as a source of elastic scattering between COM plane wave states. If $B^\dagger_{\mathbf{k}}$ creates an exciton (with bosonic character) in the state $\mathbf{k}$ (QW plane coordinate only) and dipole coupling to the light field is considered, then the Hamiltonian reads

$$\mathcal{H} = \sum_{\mathbf{k}} \frac{\hbar^2 k^2}{2M} B^\dagger_{\mathbf{k}} B_{\mathbf{k}} + \sum_{\mathbf{k},\mathbf{k}'} U_{\mathbf{k}-\mathbf{k}'} B^\dagger_{\mathbf{k}} B_{\mathbf{k}'} + \sum_{\mathbf{k}} \Big(\mu_{\mathrm{cv}} C_{\mathbf{k}}(t) B^\dagger_{\mathbf{k}} + \mathrm{h.c.} \Big) \tag{C.1}$$

The energies are referred to the energy $\hbar\omega_X$ of the $1s$ exciton in a QW without disorder, $U_{\mathbf{k}} = W_{\mathbf{k}} + Z_{\mathbf{k}}$ couples exciton states whose wavevectors differ by $\mathbf{k}$ and its value is given by the Fourier transform of disorder plus systematic potential, $C_{\mathbf{k}}(t)$ is the photon operator. The Heisenberg equation $-i\hbar\partial_t B_{\mathbf{k}} = [\mathcal{H}, B_{\mathbf{k}}]_-$, gives

$$-i\hbar\partial_t B_{\mathbf{k}} = \frac{\hbar^2 k^2}{2M} B^\dagger_{\mathbf{k}} + \sum_{\mathbf{q}} U_{\mathbf{q}-\mathbf{k}} B^\dagger_{\mathbf{k}} + \mu_{\mathrm{cv}} C_{\mathbf{k}} \, . \tag{C.2}$$

Taking the expectation value and Fourier transforming into real space coordinates, we get

$$\left(i\hbar\partial_t - \frac{\hbar^2 \Delta_{\mathbf{R}}}{2M} + U(\mathbf{R}) \right) P(\mathbf{R}, t) = \mu_{\mathrm{cv}} E_{\mathrm{in}}(\mathbf{R}, t) e^{-i\omega_{\mathrm{in}} t} \, , \tag{C.3}$$

where $U(\mathbf{R}) = W(\mathbf{R}) + Z(\mathbf{R})$. This is equivalent to Eq. (4.1) together with Eq. (4.2).

C.2 Exact results without disorder: continuum case

Here we present a method for solving the problem Eq. (4.4) in the continuum case.

We switch to the momentum-time plane by means of the Fourier definitions

$$f(k) = \int dy \, e^{iky} f(y); \qquad f(y) = \frac{1}{2\pi} \int dk \, e^{-iky} f(k) \, , \tag{C.4}$$

and obtain

$$\left(i\hbar\partial_t - \frac{\hbar^2 k^2}{2M} - i\hbar g\partial_k\right) P(k,t) = 0\,, \tag{C.5}$$

with initial condition $P(k,0^+) = -(i\mu_{\mathrm{cv}}/\hbar)\,E_{\mathrm{in}}(k)$. This is a first order partial differential equation which can be solved using the method of the characteristics [80]. It maps the partial differential equations (PDE) problem Eq. (C.5) to a set of ordinary differential equations (ODE) whose solution represents a new frame of coordinates (r,s) (the so called "characteristics") and to an ODE that describes the solution change of the PDE along the characteristics.
The following relations between old and new variable sets is assumed:

$$\begin{aligned} t &= t(r,s) \\ k &= k(r,s) \\ P &= P(t(r,s);k(r,s))\,. \end{aligned} \tag{C.6}$$

The original problem is then mapped to the total differential

$$\frac{dP}{dr} = \frac{\partial P}{\partial r} + \frac{\partial t}{\partial r}\frac{\partial P}{\partial t} + \frac{\partial k}{\partial r}\frac{\partial P}{\partial k}\,. \tag{C.7}$$

Identification of the coefficients leads to the system of ODE

$$\begin{aligned} \frac{\partial t}{\partial r} &= 1 \\ \frac{\partial k}{\partial r} &= -g \\ \frac{dP}{dr} &= \frac{i\hbar k^2}{2M}P = \frac{i\hbar(s-gr)^2}{2M}P\,. \end{aligned} \tag{C.8}$$

With the initial condition $t = 0^+, k(t = 0^+) = s, P(k,0^+) = P(s,0^+)$, this is integrated to

$$P(r,s) = P(r,0^+)\exp\left(-\frac{i\hbar}{2Mg}\int_s^{s-gr} du\,u^2\right) \tag{C.9}$$

or, restoring the old variables, to

$$P(k,t) = P(k+gt,0^+)\exp\left(\frac{i\hbar}{6Mg}((k+gt)^3 - k^3)\right)\,. \tag{C.10}$$

The k-quadratic term in Eq. (C.10) is independent of the gradient g, thus $|P(y,t)|^2$ has got amplitude and width in y direction that do not depend on g, see Eq. (4.6). The k-linear term in Eq. (C.10) is responsible for $|P(y,t)|^2$ being centred at a position which changes with time, with acceleration proportional to g. Finally, the intensity in k space only depends on the initial condition, according to

$$I(k,t) = |P(k,t)|^2 = \hbar^{-2}\,E_{\mathrm{in}}^2(k+gt)\,. \tag{C.11}$$

C.3 Exact results without disorder: discrete case

We present here some dynamical results for the 1D tight-binding problem in presence of a constant force. The discussion follows the derivation given in [21] for the case of a static electric field.

First the free problem

$$H = -\frac{\hbar^2}{2M}\partial_y^2 \tag{C.12}$$

is discretized on a mesh of grid step Δ_x. This implies looking for eigenstates and using second derivatives respectively of the form

$$\begin{aligned} \psi_k^{(j)} &= A e^{iky_j} \\ \left(\psi_k^{(j)}\right)'' &= \frac{\psi_k^{(j+1)} + \psi_k^{(j-1)} - 2\psi_k^{(j)}}{\Delta_x^2} \, . \end{aligned} \tag{C.13}$$

With this ansatz the tight-binding dispersion

$$E(k) = 2T_0(1 - \cos(k\Delta_x)) \, , \quad T_0 = \frac{\hbar^2 \Delta_x^{-2}}{2M} \tag{C.14}$$

is obtained. The constant force $\hbar\mathbf{g}$ is responsible for the exciton moving periodically along this dispersion with velocity given by [21]

$$v(t) = \frac{1}{\hbar}\left(\frac{dE}{dk}\right)_{k=gt} = \frac{2T_0\Delta_x}{\hbar}\sin(tg\Delta_x) \, . \tag{C.15}$$

The period of the oscillation is $\tau_g = 2\pi/(g\Delta_x)$. With the initial condition $y_c(t = 0) = 0$, Eq. (C.15) is integrated to

$$y_c(t) = \frac{2T_0}{\hbar g}\left(1 - \cos(tg\Delta_x)\right) = y_{\max}\sin^2(tg\Delta_x/2) \, . \tag{C.16}$$

$y_{\max}$ is the maximum elongation of the periodical motion in real space (“Bloch oscillations”).

For short times $t \ll \tau_g$ after excitation (or for small grid step Δ_x), the exciton moves in the parabolic part of the dispersion Eq. (C.14) and the tight-binding solution approaches the continuum case, (cp. Eq. (4.6)),

$$y_c(t) \approx \frac{1}{2}at^2 \, , \quad a = \frac{\hbar g}{M} \, . \tag{C.17}$$

A numerical example is given in Fig. C.1.

C.4 Disorder and real space dynamics

As introduced in Sect. (4.4) we characterize the real space motion in presence of both disorder and systematic potential in terms of the moments $y_c(t)$ and $w(t)$ defined

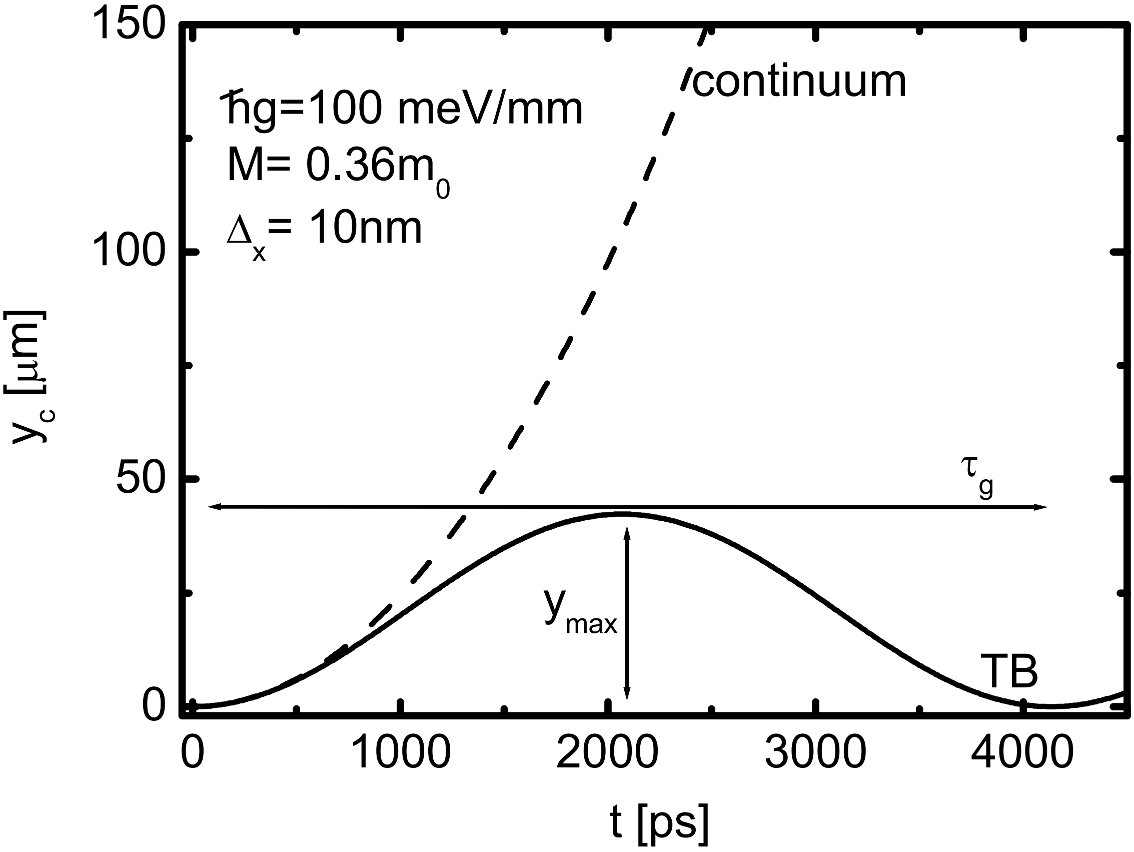

Figure C.1: *Tight-binding (solid line) vs. continuum case (dashed line) center position $y_c(t)$ of a wave packet of mass M in presence of a constant force $\hbar g$ and for a mesh step Δ_x. Maximum elongation $y_{\max}$ and period τ_g of the periodic motion for the tight-binding case are indicated.*

by Eq. (4.10).

For strong disorder, we expand the polarization P in terms of localized states ψ_α,

$$P(0,y,t) = \sum_\alpha c_\alpha(t)\psi_\alpha(0,y)\,, \tag{C.18}$$

with expansion coefficients

$$c_\alpha(t) = c_{\alpha 0}\exp\left(i(\epsilon_\alpha^{(0)} + Z_\alpha)t\right) \tag{C.19}$$

(cp. Eq. (4.15), Eq. (4.16) and Eq. (4.18)). The moment y_c is thus

$$y_c = \sum_{\alpha,\beta} c_{\alpha 0}c_{\beta 0}^* \int dy\, y\, \psi_\alpha(0,y)\psi_\beta(0,y) \Bigg/ \sum_{\alpha,\beta} c_{\alpha 0}c_{\beta 0}^* \int dy\, \psi_\alpha(0,y)\psi_\beta(0,y)\,. \tag{C.20}$$

Due to the oscillating factor in Eq. (C.19), the average over a large exciton ensemble selects only diagonal terms, obtaining a time-independent value

$$y_c \approx \sum_\alpha |c_{\alpha 0}|^2 \int dy\, y\, \psi_\alpha^2(0,y) \Bigg/ \sum_\alpha |c_{\alpha 0}|^2\,, \tag{C.21}$$

where the normalization of the wavefunctions $\psi_\alpha(0,y)$ has been exploited. In a similar way, we obtain for the width parameter w

$$w^2 \approx 2\sum_\alpha |c_{\alpha 0}|^2 \int dy\, y^2\, \psi_\alpha^2(0,y) \Bigg/ \sum_\alpha |c_{\alpha 0}|^2\,. \tag{C.22}$$

The quantity $\left(\int dy\, y^2\, \psi_\alpha^2(0,y)\right)^{1/2}$ can be considered as the localization length of the state $\psi_\alpha(\mathbf{R})$ along the direction y.

C.5 Correlation function

Here we prove the expression Eq. (4.32) for the speckle correlation function. Since the denominator of the correlation function defined as in Eq. (4.30) is time and direction independent and given by $\langle I\rangle_{\mathbf{k},t}^2$, we only need to evaluate the numerator $N(\Delta\mathbf{k},\tau)$ of the correlation. Due to the subtractions of the intensity average value, it reads

$$\begin{aligned} N(\Delta\mathbf{k},\tau) &= \Big\langle \sum_{\alpha\neq\beta,\gamma\neq\delta} e^{i(\epsilon_\alpha^{(0)}+Z_\alpha-\epsilon_\beta^{(0)}-Z_\beta)(t-\tau/2)/\hbar} e^{i(\mathbf{k}-\Delta\mathbf{k}/2)\cdot(\mathbf{R}_\alpha-\mathbf{R}_\beta)} \times \\ &\qquad e^{i(\epsilon_\gamma^{(0)}+Z_\gamma-\epsilon_\delta^{(0)}-Z_\delta)(t+\tau/2)/\hbar} e^{i(\mathbf{k}+\Delta\mathbf{k}/2)\cdot(\mathbf{R}_\gamma-\mathbf{R}_\delta)} \times \\ &\qquad m_\alpha^2 m_\beta^2 m_\gamma^2 m_\delta^2\, E_{\rm in}(\mathbf{R}_\alpha)E_{\rm in}(\mathbf{R}_\beta)E_{\rm in}(\mathbf{R}_\gamma)E_{\rm in}(\mathbf{R}_\delta)\Big\rangle_{\mathbf{k},t}\,. \end{aligned} \tag{C.23}$$

The average implies either ($\alpha=\beta$, $\gamma=\delta$), which does not appear in the sum, or ($\alpha=\delta$, $\beta=\gamma$) which results in

$$\begin{aligned} N(\Delta\mathbf{k},\tau) &= \left|\sum_\alpha e^{i(\epsilon_\alpha^{(0)}+Z_\alpha)\tau/\hbar} e^{i\Delta\mathbf{k}\cdot\mathbf{R}_\alpha} m_\alpha^4 E_{\rm in}^2(\mathbf{R}_\alpha)\right|^2 \\ &= \left|\int d\mathbf{R} e^{i(\Delta\mathbf{k}\cdot\mathbf{R}+Z(\mathbf{R})\tau/\hbar)} E_{in}^2(\mathbf{R}) \sum_\alpha e^{i\epsilon_\alpha^{(0)}\tau/\hbar} m_\alpha^4 \delta(\mathbf{R}-\mathbf{R}_\alpha)\right|^2 . \end{aligned} \tag{C.24}$$

If energies $\epsilon_\alpha^{(0)}$ and positions $\mathbf{R}_\alpha$ are uncorrelated (i.e. if level repulsion can be neglected [79, 77]), the following sum does not depend on $\mathbf{R}$ in the normalization area A:

$$\sum_\alpha e^{i\epsilon_\alpha^{(0)}\tau/\hbar} m_\alpha^4 \delta(\mathbf{R}-\mathbf{R}_\alpha) = \frac{1}{A}\sum_\alpha e^{i\epsilon_\alpha^{(0)}\tau/\hbar} m_\alpha^4 = \hbar \int d\omega\, e^{i\omega\tau} I^{\rm coh}(\omega)\,. \tag{C.25}$$

According to the last equation, the RRS of the system without systematic potential is

$$I^{\rm coh}(\omega) = \frac{1}{A}\sum_\alpha m_\alpha^4 \delta(\hbar\omega - \epsilon_\alpha^{(0)})\,. \tag{C.26}$$

Notice that the spectrum $I^{\mathrm{coh}}(\omega)$ of the unstrained sample appears here, since all strain dependence has been absorbed into the spatial integration of Eq. (C.24). We have thus found

$$N(\Delta\mathbf{k},\tau) = \langle I\rangle_{\mathbf{k},t}^{2}\ \varphi_0(\tau)\left|\int d\mathbf{R} e^{i(\Delta\mathbf{k}\cdot\mathbf{R}+Z(\mathbf{R})\tau/\hbar)} E_{in}^{2}(\mathbf{R})\right|, \tag{C.27}$$

which is equivalent to Eq. (4.32).

Appendix D

Appendices to Chapter 5

D.1 Coupling function: approximation

The coupling function $f(E)$ is at the heart of the non Markovian dynamics. It is therefore worth of deeper understanding. According to the definition Eq. (5.12) and to the expression for the deformation potential matrix elements Eq. (B.2), the coupling function $f(E)$ is given by the angular average of

$$\left[D_c K_e(q_z)\chi(\mathbf{q}_\parallel/\eta_e) - D_v K_h(q_z)\chi(\mathbf{q}_\parallel/\eta_h)\right]^2 (\psi_1\psi_1)^2_{\mathbf{q}_\parallel} \tag{D.1}$$

on the sphere of radius E/s in momentum space.

We would like to have a feeling of the shape of the coupling function. Therefore we take an isotropic Gaussian COM wavefunction, $\psi_\alpha(\mathbf{R}) = \exp(-R^2/2L^2_{COM})$, and assume $L_e = L_h = L_1$ as typical confinement size. Since the relative motion function χ has range $1/a_B$, it is approximated by $\chi(0) = 1$ in the range $1/L_{COM} \ll 1/a_B$ of $(\psi_1\psi_1)^2_{\mathbf{q}_\parallel}$. Thus, we obtain

$$f(E) \sim e^{-\frac{1}{2}E^2(L_{COM}/s)^2} \int_0^1 d\xi \exp\left(\frac{E^2\xi^2}{2s^2}(L^2_{COM} - L^2_1)\right) . \tag{D.2}$$

Using the Dawson integral $F(x) = e^{-x^2}\int_0^x dv\, e^{+v^2}$ [1], we finish with the compact expression

$$f(E) = f(E=0)\,\frac{F(x)}{x}\exp(-\frac{1}{2}(EL_1/s)^2) \tag{D.3}$$

with $x = E\sqrt{(L^2_{COM} - L^2_1)/2s^2}$. The COM localization length dominates the low energy part of $f(E)$, while its tails are determined by the well width L_z, Fig. D.1. For $L_{COM} \gg L_1$ the width of $f(E)$ is of the order of $\hbar s/L_{COM}$. At high temperature T, it is simply $Y(t) = k_B T f(t)$, with the Fourier transform $f(t)$ of $f(E)$. Therefore in this limit the BM gives

$$|P_1(t)| = m_1\theta(t)\exp(k_B T(f(t) - f(t=0))) . \tag{D.4}$$

The polarization amplitude decays to its asymptotic value in a characteristic time which is about L_{COM}/s for the case $L_{COM} \gg L_1$. We can interpret this time as the memory depth of the system. It corresponds to the time an acoustic wave of velocity s takes for going through an exciton state of COM extension L_{COM}.

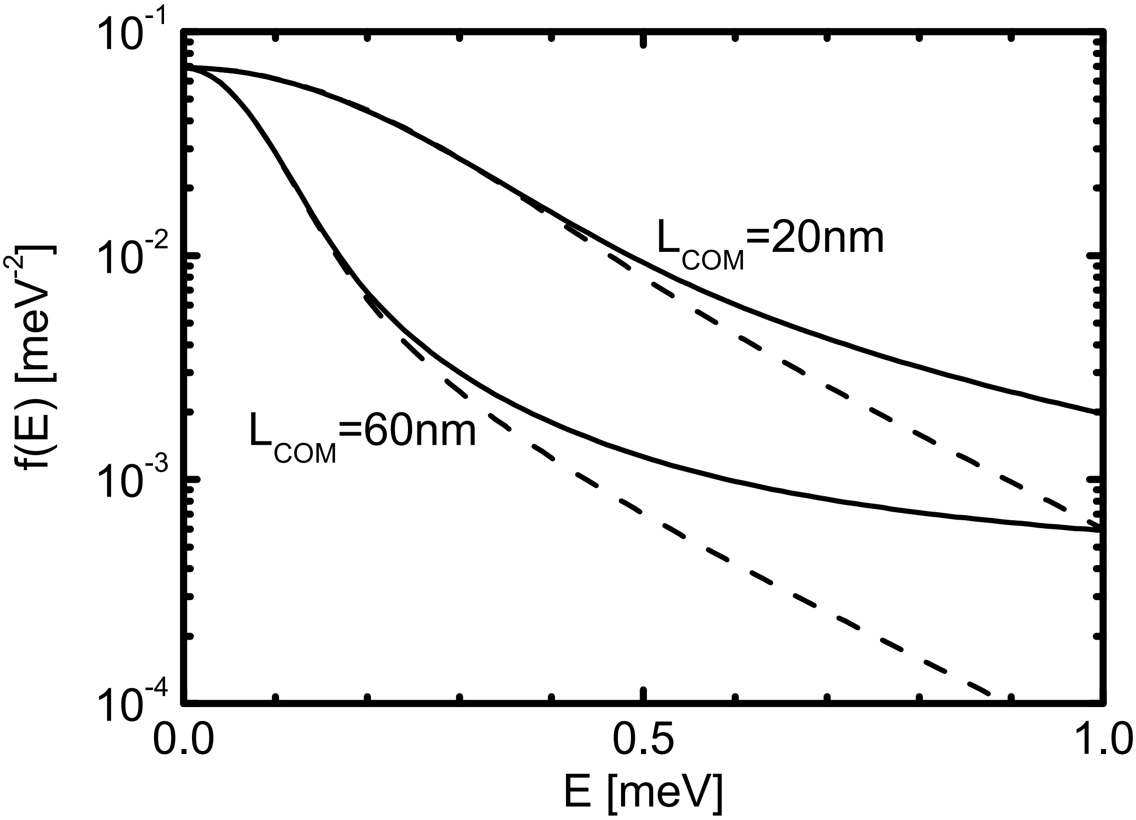

Figure D.1: *Coupling function $f(E)$ (solid lines) and its approximation according to Eq. (D.3) (dashed) for two different COM sizes.*

D.2 Coupling function: numerics

The choice of the coordinate system for a numerical evaluation of the coupling function $f^{\beta\theta}_{\alpha\eta}(E)$ depends on the matrix elements $t^{\mathbf{q}}_{\alpha\beta}$. Since these are computed in cartesian coordinates, we write Eq. (5.12) as

$$|E|^3 f^{\beta\theta}_{\alpha\eta}(E) = \frac{V}{(2\pi)^3}\int dq_x dq_y dq_z\, t^{\mathbf{q}}_{\alpha\beta} t^{-\mathbf{q}}_{\eta\theta}\, \delta(|E| - \hbar s\sqrt{q_x^2+q_y^2+q_z^2}) \tag{D.5}$$

Exploiting the delta function for eliminating the q_z integration, we obtain

$$f^{\beta\theta}_{\alpha\eta}(E) = C\cdot\int_{-1}^{1} du \int_{-\sqrt{1-u^2}}^{\sqrt{1-u^2}} dv\, \Lambda(|E|,u,v)\, (\psi_\alpha\psi_\beta)_{\frac{|E|}{\hbar s}\mathbf{u}}\, (\psi_\eta\psi_\theta)^*_{\frac{|E|}{\hbar s}\mathbf{u}} \tag{D.6}$$

where

$$\begin{aligned} C &= \frac{1}{s^2\rho(2\pi)^3(\hbar s)^3} \\ \mathbf{u} &= (u,v) = \frac{\hbar s}{|E|}(q_x,q_y) \\ t(u,v) &= \sqrt{1-(u^2+v^2)} \\ \Lambda(E,u,v) &= \frac{1}{t(u,v)}\left(\sum_{a=e,h} D_a\, K_a\left(\frac{E}{\hbar s}t(u,v)\right)\, \chi_a\!\left(\frac{E}{\hbar s}\frac{\sqrt{u^2+v^2}}{\eta_a}\right)\right)^2 \end{aligned}$$

D_a, χ_a, K_a, and $(\psi_\alpha \psi_\beta)_{\frac{|E|}{\hbar s}\mathbf{u}}$ have the same meaning and the same values as in Sect. (B.1). The factor $[t(u,v)]^{-1}$ presents an integrable singularity at the borders of the integration area. For the numerical integration, it is smoothed as ($\rho^2 = u^2 + v^2$):

$$\frac{1}{\sqrt{1-\rho^2}} \approx \sqrt{\frac{1}{2} \frac{(1-\rho^2) + \sqrt{(1-\rho^2)^2 + \epsilon^2}}{(1-\rho^2)^2 + \epsilon^2}} \tag{D.7}$$

with $\epsilon \approx 10^{-4}$.

D.3 Selfenergy

Evaluation of the real part of the polarization selfenergy presents the problem that the integrand of Eq. (5.15) has poles. We have the structure

$$\mathrm{Re}\Sigma = P \int dx \frac{N(x)}{c + dx} \,. \tag{D.8}$$

An integration by the trapezoidal rule cannot care for singularities. Therefore, a linear interpolation of the numerator function is necessary. It leads to

$$\begin{aligned} \mathrm{Re}\Sigma \;&\approx\; \sum_j \int_{E_j}^{E_j+\Delta} dx \frac{a_j + b_j x}{c + dx} \\ &=\; \sum_j \frac{b_j}{d}\Delta + \frac{a_j d - b_j c}{d^2} \Big(\log|c + dx|\Big)\Big|_{E_j}^{E_j+\Delta} \,, \end{aligned} \tag{D.9}$$

with the (real) interpolation coefficients:

$$\begin{aligned} a_j &= N(E_j)\,(1 + E_j/\Delta) - N(E_j + \Delta)\,E_j/\Delta \,, \\ b_j &= \left(N(E_j + \Delta) - N(E_j)\right)/\Delta \,. \end{aligned}$$

An eventual singularity at the grid point E_{j+1} (implying $c + dE_{j+1} = 0$) is now compensated. Therefore in the integration routine the quantity $\log|c + dE_{j+1}|$ is set to zero if $c + dE_{j+1} = 0$.

D.4 Polarization

Single state
Since the polarization spectrum consists of a narrow ZPL on top of a smooth BB, special numerical care has to be taken in the Fourier transformation into the time domain. Using the expression Eq. (5.37) for the ZPL, the total polarization is written as

$$P_1(\Omega) = \frac{S_1(\epsilon_1)}{(\hbar\Omega - \epsilon_1)(1 + R')} + P_1^{BB}(\Omega) \,. \tag{D.10}$$

The first term on the r.h.s. can be analytically transformed, leading to

$$P_1(t) = i\theta(t) \frac{2\pi e^{i\epsilon_1 t/\hbar} S(\epsilon_1)}{1 + R'} + \hbar \int d\Omega \, e^{i\Omega t} P_1^{BB}(\Omega) \tag{D.11}$$

The function $P_1^{BB}(\Omega)$ is smooth enough for applying standard Fourier routines.

Multi state

In the multi state case, ZPL have finite widths due to real transitions. Nevertheless, it is desirable to avoid transforming such spiky features with the same numerical tool used for the BB. We assume that the total polarization $P(\Omega) = \sum_\alpha m_\alpha P_\alpha(\Omega) \Big/ \sum_\alpha m_\alpha^2$ in the vicinity of the poles is approximately given by

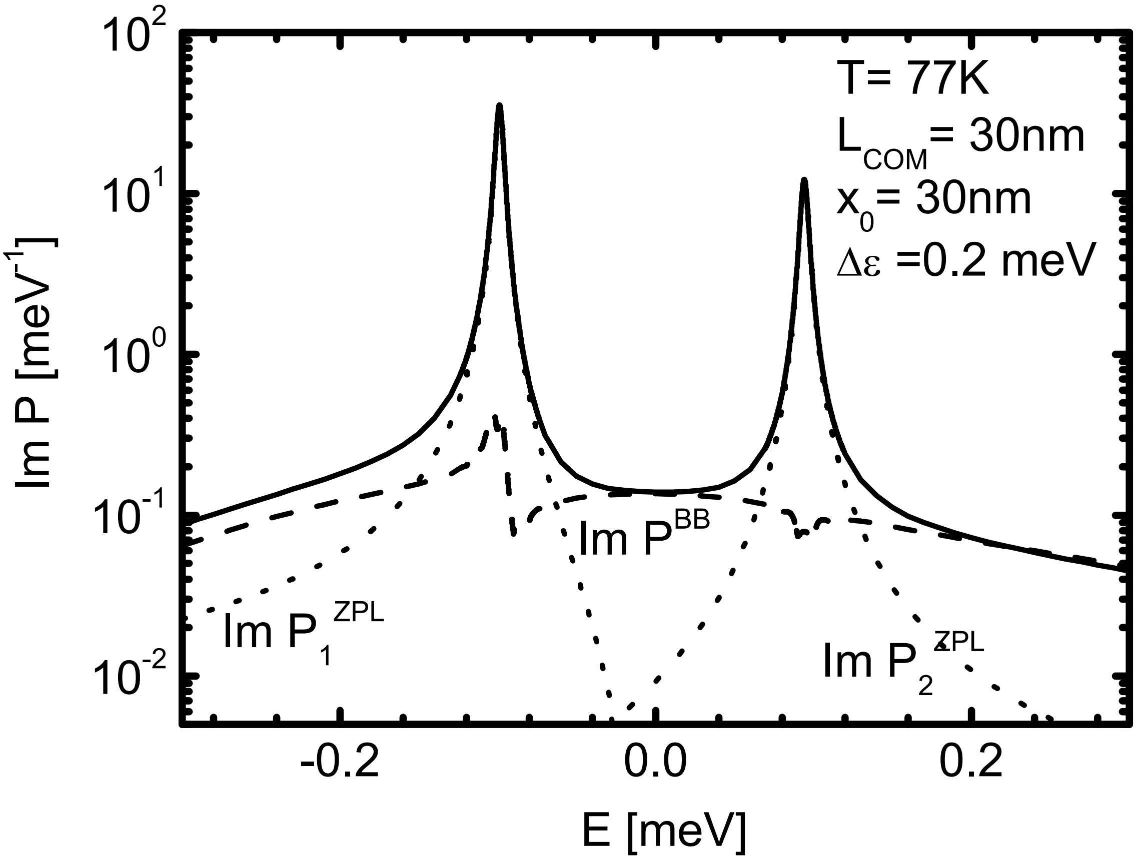

Figure D.2: *Absorption spectrum (solid line), fitted ZPL contributions (dotted) according to Eq. (D.12) and imaginary part of the difference* $P^{BB} = P - \sum_\alpha P_\alpha^{ZPL}$ *(dashed). Notice the logarithmic scale.*

$$P(\Omega \approx \epsilon_\alpha/\hbar) = \frac{W_\alpha}{(\hbar\Omega - \epsilon_\alpha) - \frac{i}{2}\hbar\Gamma_\alpha} + C_\alpha \equiv P_\alpha^{ZPL}(\Omega)\,, \tag{D.12}$$

with complex coefficients $W_\alpha, \Gamma_\alpha, C_\alpha$, see Fig. D.2. Fitting this expression allows to extract the Lorentz-shaped ZPL and to be left with a smooth function for the Fourier transformation. Like in the single state case, we distinguish a part that has analytical transformation and obtain

$$P(t) = i\theta(t) \sum_\alpha 2\pi W_\alpha e^{i\epsilon_\alpha t/\hbar - \frac{1}{2}\Gamma_\alpha t} + \hbar \int d\Omega\, e^{i\Omega t} P^{BB}(\Omega)\,. \tag{D.13}$$

The complex coefficients are given by

$$\begin{aligned}
\Gamma_\alpha &= \frac{2x}{\hbar}\sqrt{\frac{2-4\rho_\alpha}{\rho_\alpha-2}} \\
W_\alpha &= \left(P((\epsilon_\alpha+x)/\hbar) - P((\epsilon_\alpha-x)/\hbar)\right)\cdot\frac{x^2+(\hbar\Gamma_\alpha/2)^2}{2x} \\
C_\alpha &= P(\epsilon_\alpha/\hbar) - \frac{2i\,W_\alpha}{\hbar\Gamma_\alpha}
\end{aligned} \tag{D.14}$$

with

$$\rho_\alpha = \frac{P((\epsilon_\alpha+2x)/\hbar) - P((\epsilon_\alpha-2x)/\hbar)}{P((\epsilon_\alpha+x)/\hbar) - P((\epsilon_\alpha-x)/\hbar)}\,, \tag{D.15}$$

where x has to be of the order of magnitude of $\hbar\Gamma_\alpha$.

D.5 Normalization of the absorption

A useful normalization condition of the absorption spectrum holds for both Markovian and non-Markovian dynamics. First, we prove it for the single state case. Extending $P_1(\Omega)$ to an analytic function of complex variable, it holds

$$P_1(\Omega) = \frac{1}{2\pi i}\oint d\nu\,\frac{P_1(\nu)}{\Omega-\nu}\,. \tag{D.16}$$

When integrating along a path around the cut on the real axis, only twice the imaginary part of the integrand survives. Exploiting for the l.h.s. $P_1(|\Omega|\to\infty) = m_1 A_p/(2\pi\hbar\Omega)$, (due to Eq. (5.29) used for $S_1(t) = m_1 A_p\,\delta(t)$) one ends up with

$$\frac{A_p}{2}\,m_1^2 = \hbar m_1\int_{-\infty}^{+\infty} d\nu\,\mathrm{Im}P_1(\nu)\,. \tag{D.17}$$

The same argument applies for the multi state case, i.e. for P_α in Eq. (5.2). Indeed it is only required that $P_\alpha(\Omega)\to 0$ for $|\Omega|\to\infty$. Therefore, for the total polarization $P(\Omega) = \sum_\alpha m_\alpha P_\alpha$ we have [1]

$$\frac{A_p}{2}\sum_\alpha m_\alpha^2 = \hbar\int_{-\infty}^{+\infty} d\nu\,\mathrm{Im}P(\nu)\,. \tag{D.18}$$

It is easily verified that this holds for the Markov case, too, by replacing $P_\alpha(\Omega)$ from Eq. (5.26).

---

[1] $\sum_\alpha m_\alpha^2 = A$ (A=normalization area) if a complete set of states is considered.

Appendix E

List of abbreviations

BB	broad band
BM	(independent) boson model
COM	center-of-mass
cw	continuous wave
E	electron (confinement level in quantum well)
FWHM	full width half maximum
FWM	four wave mixing
HH	heavy hole (confinement level in quantum well)
LA	longitudinal acoustic (phonon)
LH	light hole (confinement level in quantum well)
LO	longitudinal optical (phonon)
MBE	molecular beam epitaxy
PL	photoluminescence
QD	quantum dot(s)
QW	quantum well(s)
RRS	resonant Rayleigh scattering
2B	2nd Born approximation
SE	secondary emission
SQW	single quantum well(s)
ZPL	zero phonon line

Bibliography

[1] M. Abramowitz and I. A. Stegun. *Handbook of Mathematical Functions with Formulas, Graphs, and Mathematical Tables.* Dover, New York, 1964.

[2] S. Adachi. *Physical Properties of III-V Semiconductor Compounds InP, InAs, GaAs, GaP, InGaAs, InGaAsP.* World Scientific, Singapore, 1994.

[3] Z. I. Alferov. *Rev. Mod. Phys.*, 73:767, 2001.

[4] L. C. Andreani. *Solid State Comm.*, 77:641, 1991.

[5] L. C. Andreani. *NATO ASI Series*, B 340:57, 1995.

[6] V. M. Axt, M. Herbst, and T. Kuhn. *Superlattices Microstruct.*, 26:117, 1999.

[7] L. Bányai, D. B. Tran Thoai, E. Reitsamer, H. Haug, D. Steinbach, M. U. Wehner, M. Wegener, T. Marschner, and W. Stolz. *Phys. Rev. Lett.*, 75:2188, 1995.

[8] L. Besombes, K. Kheng, L. Marsal, and H. Mariette. *Phys. Rev. B*, 63:155307, 2001.

[9] D. Birkedal and J. Shah. *Phys. Rev. Lett.*, 81:2372, 1998.

[10] P. Borri, W. Langbein, S. Schneider, U. Woggon, R. L. Sellin, D. Ouyang, and D. Bimberg. *Phys. Rev. Lett.*, 87:157401, 2001.

[11] R. Cerbino, A. Vailati, and M. Giglio. *Phys. Rev. E*, 66:05530(R), 2002.

[12] K. Chesnel, M. Belakhovsky, G. van der Laan, F. Livet, A. Marty, G. Beutier, S. P. Collins, and A. Haznar. *Phys. Rev. B*, 70:180402(R), 2003.

[13] J. C. Dainty, editor. *Laser Speckle and Related Phenomena.* Springer-Verlag, 1984.

[14] X. Fan, T. Takagahara, J. E. Cunningham, and Hailin Wang. *Solid State Comm.*, 108:857, 1998.

[15] Max-Planck Institut für Radioastronomie. Infrared interferometry group. www.mpifr-bonn.mpg.de/div/ir-interferometry.

[16] A. Fürst, A. Leitenstorfer, A. Laubereau, and R. Zimmermann. *Phys. Rev. Lett.*, 78:3733, 1997.

[17] J. Grenzler, U. Zeimer, S. A. Grigorian, S. Feranchuk, U. Pietsch, J. Fricke, H. Kissel, A. Knauer, and M. Weyers. *Phys. Rev. B*, 69:125316, 2004.

[18] M. Grochol, F. Grosse, and R. Zimmermann. In *Proceedings of the 6th EXCON, Cracow*, 2004.

[19] M. Grochol, F. Grosse, and R. Zimmermann. *Phys. Rev. B*, 71:125339, 2005.

[20] F. Grosse and R. Zimmermann. *Superlattices and Microstructures*, 17:439, 1995.

[21] G. Grosso and G. Pastori Parravicini. *Solid State Physics.* Academic Press, 2000.

[22] M. Gurioli, F. Bogani, S. Ceccherini, and M. Colocci. *Phys. Rev. Lett.*, 78:3205, 1997.

[23] S. Haacke, R. A. Taylor, R. Zimmermann, I. Bar-Joseph, and B. Deveaud. *Phys. Rev. Lett.*, 78:2228, 1997.

[24] J. Hegarty, M. D. Sturge, C. Weisbuch, A. C. Gossard, and W. Wiegmann. *Phys. Rev. Lett.*, 49:930, 1982.

[25] W. Hoyer, M. Kira, S. W. Koch, H. Stolz, S. Mosor, J. Sweet, C. Ell, G. Khitrova, and H. M. Gibbs. *Phys. Rev. Lett.*, 93:067401, 2004.

[26] W. A. Hügel, M. Wegener, Q. T. Vu, L. Bányai, H. Haug, F. Tinjod, and H. Mariette. *Phys. Rev. Lett.*, 66:153203, 2002.

[27] S. P. Kennedy, N. Garro, and R. T. Phillips. *Phys. Rev. Lett.*, 86:4148, 2001.

[28] M. Kira, F. Jahnke, and S. W. Koch. *Phys. Rev. Lett.*, 82:3544, 1999.

[29] G. Kocherscheidt. *Speckle analysis and spectral interferometry on gallium arsenide single quantum wells.* PhD thesis, Universität Dortmund, Experimentelle Physik IIB, 2003.

[30] G. Kocherscheidt, W. Langbein, G. Mannarini, and R. Zimmermann. *Phys. Rev. B*, 66:161314(R), 2002.

[31] G. Kocherscheidt, W. Langbein, G. Mannarini, and R. Zimmermann. In *Proceedings of the 26th ICPS, Edinburgh.* Institute of Physics Conference Series, No. 171, paper M 3.2, 2002.

[32] G. Kocherscheidt, W. Langbein, U. Woggon, V. Savona, R. Zimmermann, D. Reuter, and A. D. Wieck. *Phys. Rev. B*, 68:085207, 2003.

[33] B. Krummheuer, V. M. Axt, and T. Kuhn. *Phys. Rev. B*, 65:195313, 2002.

[34] A. Labeyrie. *Astronom. Astrophys.*, 6:85, 1970.

[35] W. Langbein. *Habilitationsschrift.* Universität Dortmund, 2002.

[36] W. Langbein and J. M. Hvam. *phys. stat. sol. (a)*, 178:13, 2000.

[37] W. Langbein, J. M. Hvam, and R. Zimmermann. *Phys. Rev. Lett.*, 82:1040, 1999.

[38] W. Langbein, R. Zimmermann, R. Runge, and J. M. Hvam. *phys. stat. sol. (b)*, 221:349, 2000.

[39] L. Lepetit, G. Chériaux, and M. Joffre. *J. Opt. Soc. Am. B*, 12:2467, 1995.

[40] J. Liu, D. D. Cannon, K. Wada, Y. Ishikawa, D. T. Danielson, S. Jongthammanurak, J. Michel, and L. C. Kimerling. *Phys. Rev. B*, 70:155309, 2004.

[41] R. Loudon. *The Quantum Theory of Light.* Clarendon Press, Oxford, 1983.

[42] G. D. Mahan. *Many-Particle Physics.* Plenum Press, 1990.

[43] G. Mannarini, F. Grosse, R. Zimmermann, S. Kassbohm, and W. Langbein. *Phys. Rev. B*, 69:085326, 2004.

[44] G. Mannarini, W. Langbein, and R. Zimmermann. *phys. stat. sol. (c)*, 1:489, 2004.

[45] G. Mannarini, R. Zimmermann, G. Kocherscheidt, and W. Langbein. *phys. stat. sol. (b)*, 238:494, 2003.

[46] K. Matsuda, T. Saiki, S. Nomura, M. Mihara, and Y. Aoyagi. *Appl. Phys. Lett.*, 81:2291, 2003.

[47] E. Muljarov and R. Zimmermann. *Phys. Rev. Lett.*, 93:237401, 2004.

[48] M. S. Pierce, R. G. Moore, L. B. Sorensen, S. D. Kevan, and O. Hellwig. *Phys. Rev. Lett.*, 90:175502, 2004.

[49] F. Rossi and T. Kuhn. *Rev. Mod. Phys.*, 74:895, 2002.

[50] E. Runge and R. Zimmermann. *Phys. Rev. B*, 61:4786, 2000.

[51] E. Runge and R. Zimmermann. *phys. stat. sol. (b)*, 221:269, 2000.

[52] S. K. Saha. *Rev. Mod. Phys.*, 74:551, 2002.

[53] J. Schilp, T. Kuhn, and G. Mahler. *Phys. Rev. B*, 50:5435, 1994.

[54] J. Schilp, T. Kuhn, and G. Mahler. *phys. stat. sol. (b)*, 188:417, 1995.

[55] J. Shah. *Ultrafast Spectroscopy of Semiconductors and Semiconductor Nanostructures.* Springer, AT&T, 1996.

[56] K. Siantidis, V. M. Axt, and T. Kuhn. *Phys. Rev. B*, 65:035303, 2001.

[57] A. Siarkos, E. Runge, and R. Zimmermann. *Phys. Rev. B*, 61:10854, 2000.

[58] D. Steinbach, G. Kocherscheidt, M. U. Wehner, H. Kalt, M. Wegener, K. Ohkawa, D. Hommel, and V. M. Axt. *Phys. Rev. B*, 60:12079, 1999.

[59] V. C. Stergiou, T. T. Pelekanos, and Y. S. Raptis. *Phys. Rev. B*, 67:165304, 2003.

[60] H. Stolz. *Time-Resolved Light Scattering from Excitons*, volume 130 of *Springer Tracts in Modern Physics*. Springer, Berlin, 1994.

[61] H. Stolz, D. Schwarze, W. von der Osten, and G. Weimann. *Phys. Rev. B*, 47: 9669, 1993.

[62] T. Takagahara. *Phys. Rev. B*, 31:6552, 1985.

[63] A. Thränhardt, C. Ell, S. Mosor, G. Rupper, G. Khitrova, H. M. Gibbs, and S. W. Koch. *Phys. Rev. B*, 68:035316, 2003.

[64] A. Thränhardt, S. Kuckenburg, A. Knorr, P. Thomas, and S. W. Koch. *Phys. Rev. B*, 62:16802, 2000.

[65] A. Vailati and M. Giglio. *Nature*, 390:262, 1997.

[66] H. Wang, J Shah, T. C. Damen, and L. N. Pfeiffer. *Phys. Rev. Lett.*, 74:3065, 1995.

[67] M. U. Wehner, M. H. Ulm, D. S. Chemla, and M. Wegener. *Phys. Rev. Lett.*, 80:1992, 1998.

[68] G. P. Weigelt. *Opt. Comm.*, 21:55, 1977.

[69] G. P. Weigelt. *Astronom. Astrophys.*, 333:L51, 1998.

[70] U. Woggon, F. Gindele, W. Langbein, and J. M. Hvam. *Phys. Rev. B*, 61:1935, 2000.

[71] R. Zimmermann. *J. Lumin.*, 53:187, 1992.

[72] R. Zimmermann. *Nuovo Cimento*, 17D:1801, 1995.

[73] R. Zimmermann. *Solid State Comm.*, 134:43, 2005.

[74] R. Zimmermann, F. Grosse, and E. Runge. *Pure and Applied Chemistry*, 69: 1179, 1997.

[75] R. Zimmermann, W. Langbein, E. Runge, and J. M. Hvam. *Physica E*, 10:40, 2001.

[76] R. Zimmermann and E. Runge. In *Proceedings of the 26th ICPS, Edinburgh.* Institute of Physics Conference Series, No. 171, paper M 3.1, 2002.

[77] R. Zimmermann and E. Runge. *Phys. Rev. B*, 69:155307, 2004.

[78] R. Zimmermann, E. Runge, and V. Savona. *Theory of resonant secondary emission: Rayleigh scattering versus luminescence* in: Quantum Coherence, Correlation and Decoherence in Semiconductor Nanostructures, edited by T. Takagahara. Elsevier Science, 2003.

[79] R. Zimmermann, E. Runge, and V. Savona. *phys. stat. sol. (b)*, 238:478, 2003.

[80] D. Zwillinger. *Handbook of Differential Equations (Second Edition)*. Academic Press, Inc., 1992.

Acknowledgments

It is for me reason of joy at the end of this work to acknowledge help and collaboration from many colleagues and friends.

First of all, I have to thank my supervisor Roland Zimmermann, who made me rich of his deep physical insight, his critical spirit and his love for precision and clarity: I feel I have received a lot from him. I am sure I would have never begun this PhD-Thesis without Vincenzo Savona, who let me know of an open position in Berlin and who closely assisted me during the first one and half year here, both from the scientific and the personal point of view. I am indebted to Erich Runge, who taught me how to improve my programming skills and allowed to use one of his software packages for the numerical projects of this Thesis. I also benefited from the collaboration with Wolfgang Langbein (presently at Cardiff University, UK), from whom I have learned the experimental side of solid state physics and who gave me the exciting experience to collaborate for two weeks in his former laboratory in Dortmund.

I could profit a lot from the stimulating atmosphere in our research group in Berlin: at this place, I would like to thank Frank Grosse and Volkhard May firstly. My previous PhD-student colleagues Axel Esser, Tomáš Mančal and Ben Brüggemann played a very important role for maintaining the LINUX network of the group and were always very friendly to me. During his PhD, Gerrit Kocherscheidt measured many of the experimental data I displayed in this Thesis and our remote collaboration was very effective. In this four years I could enjoy collaboration and friendship also with: Helge Ludwig, Nienke Boeijenga, Egor Muljarov, Andreas Kaiser, Luxia Wang, Dmitry(Dima) Tsivlin, Milana Michaljowa, and Michal Grochol. I would like to express a special thank to Sergio Caracciolo for his enduring support and advice along these years. Michael Happ and Volkmar Ullrich of the “Institutsrechenzentrum”of the Physics Department helped me whenever network or hardware problems were making me nervous. Joanna Ryćko of the “AG Elektronisches Publizieren” of the Humboldt University assisted me for the online publication of this manuscript on the EDOC-server. Marion Heider, our secretary, was always improving the atmosphere in the group with her friendly smile.

Finally, it is clear to me that I would have never completed this work successfully without the love and optimism of my friends in Italy and in Germany and the enduring trust of my family.

Lebenslauf

Name:	Gianandrea Mannarini
19.1.1977	geboren in Lecce (Italien)
9.1990–7.1995	Gymnasium in Lecce (Italien)
10.1995–10.2000	Studium an der Università di Pisa (Italien) in der Fachrichtung Physik
10.2000	Diplomarbeit: *Sub-Doppler time-resolved spectroscopy of* CH_3I *molecule* unter Betreuung von Prof. P. Minguzzi Endnote: “110/110 e lode”
2.2001–1.2005	Wissenschaftliche Mitarbeiter an der Humboldt-Universität zu Berlin, Lehrstuhl Prof. Dr. R. Zimmermann, Institut für Physik
1.2005	Doktorarbeit: *Speckle analysis of the excitonic emission from quantum wells* unter Betreuung von Prof. Dr. R. Zimmermann

Selbständigkeitserklärung

Hiermit erkläre ich, die vorliegende Arbeit selbständig ohne fremde Hilfe verfaßt und nur die angegebene Literatur und Hilfsmittel verwendet zu haben.

Gianandrea Mannarini
28. Januar 2005